# Realization of TMR Devices in an Industrial Environment

**Dissertation zur Erlangung des Doktorgrades**
**der Fakultät für Physik der**
**Universität Bielefeld**

von
**Anna Gerken**
geboren in Hamburg

Universität Bielefeld

Mainz, 2010

# Eidesstattliche Erklärung

Hiermit verichere ich, die vorliegende Arbeit selbständig verfaßt und keine anderen als die angegebenen Hilfsmittel und Quellen verwendet zu haben.

Mainz, August 2010

Anna Gerken

Gutacher:
Prof. Dr. Andreas Hütten
Prof. Dr. Dario Anselmetti

Datum des Einreichens der Arbeit: 01.09.2010

# Contents

# List of Figures

# List of Tables

# Chapter 1

# Introduction

Spintronics, the combination of electronics and the use of the electron's spin, has gained much interest over the last 20 years. The starting point for this interesting field of research and application was the discovery of the Giant MagnetoResistive Effect (GMR) by Peter Grünberg [1] and Albert Fert [2] in 1988. After fifty years of pure electronics, which uses the electron's charge only, they were the first to make use of the electron's spin as well. The discovery of the GMR-effect also fueled the research on another closely related topic: the so-called Tunneling MagnetoResistive Effect (TMR). This MR-Effect had been already discovered almost 15 years previously by Jullière but due to insufficient fabrication techniques it was difficult to prepare high-quality samples. Therefore TMR was almost forgotten until the end of the 1980s.

The first TMR-stacks contained amorphous $Al_2O_3$-barriers. In 2001 it was predicted that junctions containing single-crystalline MgO (100) tunneling barriers and suitable electrodes would result in very high TMR rations because of coherent tunneling [3]. Therefore from then on research was focused on understanding and optimizing MgO-barriers.

It turned out that, apart from Fe and Co, CoFeB was a well-suited electrode-material [4]. In contrast to the first two CoFeB can easily be integrated into standard spin-valve structures, which are known from GMR processes. This is one of the reasons why CoFeB is favourable for industrial processes.

In this thesis a layer stack consisting of sputtered CoFeB electrodes, one of them being exchange-coupled with IrMn, and an ion beam deposited MgO barrier is presented. This system was studied by many research groups and is now transferred to an industrial environment. In contrast to most publications, the MgO barrier is being prepared by ion beam deposition, a novel preparation method for TMR stacks. This technique is well suited for both, metallic and insulating materials, and allows large parameter variations to optimize film growth.

A second possibility to maximize the TMR effect is the use of optimized electrodes, e.g. half-metallic ferromagnets like certain Heusler alloys. At the fermi-energy these materials are fully spin-polarized, this results in a theoretically infinite TMR effect. Examples for Heusler alloys are $Co_2Cr_{0.6}Fe_{0.4}Al$ or $Co_2MnSi$, the latter one was used in the experiments presented in this thesis.

Conventionally Heusler-materials are sputter-deposited or deposited via MBE. Here however, the $Co_2MnSi$ films were prepared by ion beam deposition, the same method that was used for the MgO barrier formation. This was the first time ever that a Heusler alloy was deposited by ion beam; the results are very promising and prove that this technique is capable of producing high quality films.

The work presented in this thesis is a purely industrial work, i.e. all experiments were performed directly on production tools at Sensitec GmbH in Mainz [5]. The goal was to develop a TMR process that is suitable for mass production. In contrast to university research the focus was shifted to reproducibility and wafer uniformity instead of creating single perfect samples.

This work consists of two main subjects: Firstly, the development of a production process for an MgO tunneling barrier and secondly the fabrication of Heusler thin films as potential electrodes by ion beam deposition. Therefore the thesis is structured in the following way: Following a short motivation the basics of the theoretical background are presented, where the concept of tunneling magnetoresistance and the fundamental properties of Heusler alloys in general are explained. The experimental part starts with a description of the experimental procedure in general in chapter 4, the fabrication and optimization of the MgO tunneling barrier is presented in chapter 5. In contrast to university research process stability and reproducibility are of fundamental interest in an industrial environment. Therefore the stability of the MgO process was carefully monitored, the surprising results are presented in chapter 6. Finally chapter 7 is dedicated to the fabrication and characterization of $Co_2MnSi$ thin films and their implementation into TMR stacks. At the end of this thesis the work is summarized and an outlook, especially concerning the continuation of work on TMR at Sensitec, is given.

# Chapter 2

# Motivation

Sensitec GmbH is a medium sized company producing magnetoresistive sensors and magnetic micro systems [5]. The main production site in Mainz was integrated into Sensitec in 2004; previously this facility had been part of IBM's read head production line. Today Sensitec mainly produces sensors based on the AMR-effect, a smaller part of the sensor portfolio are the GMR-multilayer sensors. TMR is a logical continuation and is meant to complete the product portfolio in the near future.

In figure 2.1 the historical development of the application of the XMR-effects in HDD-heads is shown.

Sensitec does not produce HDD heads any more, however, its development is quite the same: AMR and GMR are currently used in various MR sensors; a TMR-sensor based on an alumina barrier has been developed in a separate research project in which the product development phase is about to start [7].

The development of a novel TMR sensor based on a crystalline MgO barrier is the goal of this thesis, which is incorporated into an industrial research project funded by Rhineland-Palatinate [8]. The main focus lies on finding a production process for an MgO barrier that is suitable for mass production, i.e. the process must form a uniform film over a whole wafer, be reliable and reproducible. Additionally the resistance-area-product has to be in an appropriate range for sensor applications, which is in the order of $k\Omega\mu m^2$. Another requirement is that the processes known from the GMR spin valve production should be used in the production of future TMR sensors as well. This concerns e.g. the materials used in the TMR stack and the deposition processes. In order to justify the development of a new product it must have at least one big advantage over existing ones. In

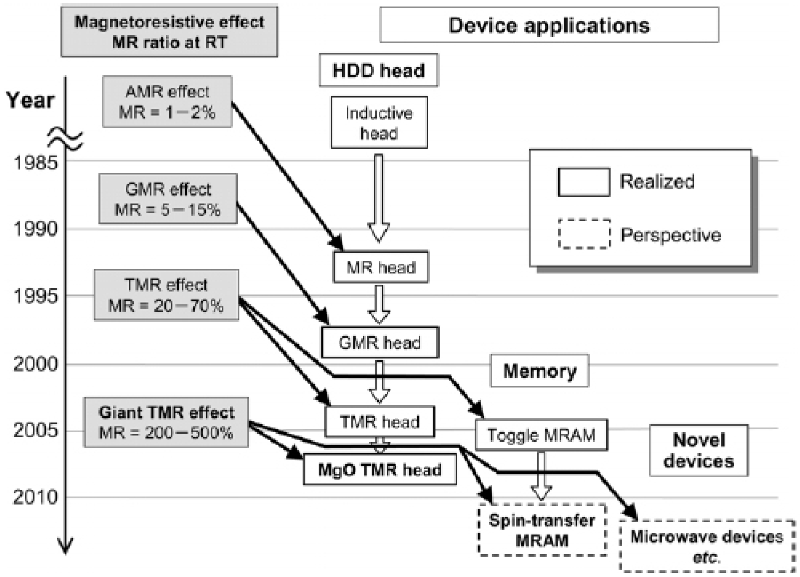

Figure 2.1: History and envisaged future of the technical usage of XMR-effects (figure taken from [6]).

the case of TMR sensors these advantages are the greater MR ratio of potentially several hundred percent at room temperature, hopefully along with an increased sensitivity, and the small dimensions of TMR junctions due to the CPP geometry.

In this thesis the first point was targeted: The work presented here focusses on the development of a TMR stack that contains an MgO barrier and/or a half-metallic electrode (Heusler electrode). Both are aimed at increasing the MR ratio. The second point, achieving smaller dimensions, is incorporated into a BMBF follow-up project called *MultiMag* [9].

# Chapter 3

# Theory

In this chapter the TMR-effect will be discussed from a theoretical point of view. There are different models to describe TMR, starting from the rather simple model developed by Jullière up to first principles calculations.

It turns out that materials with high spin polarization are preferable electrode materials, which renewed the interest in ferromagnetic half-metals, like Heusler-alloys. The interesting characteristics of this class of materials will be discussed as well.

## 3.1 Tunneling Magnetoresistance

In general the magnetoresistive (MR) effect describes the change of the electrical resistance of a material or system of materials by changing an external magnetic field. TMR, short for Tunneling Magnetoresistance, occurs in layer stacks of two ferromagnetic thin films that are separated by an insulating film, the so-called "tunneling barrier". This effect was first described by Jullière in 1975 [10], who discovered a conductance change in Fe-Ge-Co junctions depending on the relative magnetic orientation of the ferromagnetic films. Jullière also introduced a simple model to explain the TMR-effect with the following two assumptions: At low voltages tunneling is assumed to be spin-conserving and conductance is proportional to the density of states (DOS) of the ferromagnetic electrodes alone. This leads to the simple Jullière formula for the TMR, which is defined as the resistance change normalized by the resistance for parallel magnetization alignment:

$$TMR = \frac{\Delta R}{R} = \frac{R_{AP} - R_P}{R_P} = \frac{2P_1P_2}{1 - P_1P_2} \tag{3.1}$$

Here $R_{AP}$ and $R_P$ are the junction's resistance in antiparallel and parallel magnetization alignment, $P_1$ and $P_2$ are the electrodes' spinpolarizations.

Jullière's formula does not take into account the electronic density of states of the ferromagnetic electrodes. However, discrepancies between his theory and experiments suggested that the tunneling probability, which is different for different electronic states, has to be considered as well. This is integrated in Stearns' model which connects the tunneling probability to the electron's effective mass. The effective mass in turn depends on the electronic band: Nearly free electrons, like the $s$-electrons, have a lower effective mass than the localized $d$-electrons and therefore have a longer decay length. As a result only the dispersive $s$-like bands contribute considerably to the tunneling current, whereas the $d$-bands can be neglected. For these nearly free electron bands the DOS at the Fermi level is proportional to their Fermi wave vector; combining this with the assumption, that the conductance depends on the ferromagnets alone (see above) yields to the following equation for the ferromagnet's spin polarization $P_{FM}$:

$$P_{FM} = \frac{k^{\uparrow} - k^{\downarrow}}{k^{\uparrow} + k^{\downarrow}} \tag{3.2}$$

Here $k^{\uparrow}$ and $k^{\downarrow}$ are the Fermi wave vectors for majority and minority spins respectively. Using this formula Stearns found e.g. 43 % spin polarization for Ni, which is in good agreement with experiments [11].

The first exact model for the description of TMR was advanced by Slonczewski [12, 13]. Here the identical ferromagnets' band structure was modeled by parabolic bands, shifted to one another to simulate exchange splitting, the barrier potential was considered to be a rectangular potential of height $U$. After having solved the Schrödinger equation the conductance dependence on the relative magnetization orientation of the ferromagnetic electrodes was determined. The conductance depends linearly on the cosine of the angle between the electrodes' magnetization:

$$G(\theta) = G_0(1 + P^2 \cos\theta) \tag{3.3}$$

Here $P$ denotes the tunneling electrons' effective spin polarization, which is given by the following expression:

$$P = \frac{k^{\uparrow} - k^{\downarrow}}{k^{\uparrow} + k^{\downarrow}} \cdot \frac{\kappa^2 - k^{\uparrow}k^{\downarrow}}{\kappa^2 + k^{\uparrow}k^{\downarrow}} \tag{3.4}$$

In this equation the decay constant $\kappa$ is given by $\kappa = \sqrt{\frac{2m}{\hbar^2}(U - E_F)}$, where $m$ is the electron's mass and $\hbar$ the reduced Planck constant. As a result the spin polarization of a tunneling current is not an intrinsic property of the electrode, but depends on the barrier height $U$ as well. In the limit of a high barrier the second factor in equation 3.4 tends to unity and the old expression for the spinpolarization is regained.

## 3.2 Half-metallic Ferromagnets - Heusler Alloys

In applications, like magnetic sensors, AMR as well as GMR have been successfully used; the resistance changes there are in the order of 3 % for AMR and 20 % for GMR. TMR has the potential to reach MR ratios that are at least one order of magnitude higher: Following Jullière's equation 3.1 one can clearly see that the TMR increases with increasing electrode spin polarization. Heusler alloys are one particular class of materials that are predicted to be half-metallic, meaning they show ferromagnetic behaviour for one spin direction and semiconducting or insulating behaviour for the other spin direction. This means that Heusler alloys can show 100 % spin polarization at the Fermi level, compared to a maximum of 50 % for conventional ferromagnets like Ni, Fe, Co and their alloys [14]. Among the multitude of Heusler alloys the Co-based alloys are of special interest as many of them exhibit a high Curie temperature, which allows room temperature applications [15]. In this work $Co_2MnSi$ was used, therefore this alloy will be discussed as an example.

### 3.2.1 Crystallographic Structure of Heusler Alloys

In 1903 Friedrich Heusler discovered a new class of intermetallic compounds with the astonishing property of being ferromagnetic even if all elements of the compound were non-magnetic [16]. The alloy he examined was $Cu_2MnAl$; the whole group of alloys like this one was later named after him. In general full-Heusler alloys are intermetallic compounds of the general formula $X_2YZ$, where X is a transition metal, Y a transition metal or a rare earth metal and Z is either a nonmagnetic metal or a non-metal. They crystallize in the $L2_1$-structure, which

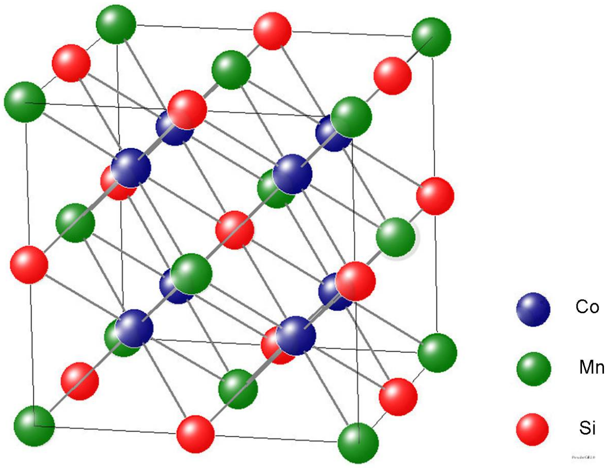

Figure 3.1: Crystal structure of $Co_2MnSi$. The blue spheres represent Co-atoms, the green ones Mn and the red ones Si.

means they form cubic lattices (space group $Fm\overline{3}m$) that can be regarded as four interpenetrating fcc-lattices. Half-Heusler alloys (XYZ), which form a $C1_b$ structure, can be constructed from full-Heusler alloys by replacing one of the X-positions by a vacancy. A schematic representation of $Co_2MnSi$, as an example for a full-Heusler crystal, is shown in figure 3.1.

This picture shows a perfect crystal, however disorder can occur in the Heusler alloys reducing the $L2_1$ order to B2 (Y-Z interchange) or even A2 (complete disorder). The latter leads to a reduced spin polarization, which in turn reduces the TMR effect in magnetic tunneling junctions. B2 ordering, which in the case of $Co_2MnSi$ means an interchange between Mn and Si, does not lead to a loss of the half-metallic properties of CMS, because Si is a relatively light atom. The main effect that destroys the half metallicity is the changing Coulomb interaction; therefore the effect is the higher, the heavier the element. The influence of disorder has been examined theoretically by Galanakis *et al.* [17]. Improving the crystalline growth of Heusler thin films to achieve at least B2 ordering is therefore crucial for applications.

Nakatani *et al.* have shown that the annealing temperature has a great influence on the degree of ordering in $Co_2MnSi$ thin films [18]. They prepared MTJs with CMS bottom and top electrode and an MgO barrier, where the bottom CMS layer was always annealed *in situ* at 600°C and the top part either at 400°C or 550°C. Annealing at 400°C led to B2 ordering, whereas 550°C resulted in $L2_1$-

ordered films. The TMR ratio increased from 80 % at room temperature for the 400°C annealed sample to 180 % at room temperature for the 550°C annealed sample [19]. Further increasing the second annealing temperature to 600°C did not improve the TMR ratio any more [20]. A detailed investigation of the degree of ordering upon annealing was also presented by Gaier *et al.* [21]. They prepared $Co_2MnSi$ films on MgO substrates with Cr seed layer and annealed them at temperatures ranging from 350°C to 500°C. They found an increase of the $L2_1$ ordered portion from 60 % after a 350°C annealing up to 90 % ordering after a 500°C annealing.

In order to determine the degree of ordering, the crystalline orientation and the lattice constant, Heusler bulk samples and thin films are often analyzed using X-ray diffraction [22]. The existing reflexes can be grouped in the following way: In an fcc crystal, like in a Heusler alloy, only those reflexes, where the Miller indices are either all even or all odd, exist. Taking this into account there are three groups of reflections:

1. h, k, l are all odd (e.g. (111))
2. $(h + k + l)/2 = 2n + 1$ (e.g. (200))
3. $(h + k + l)/2 = 2n$ (e.g. (220))

The third group is the group of principal reflections that are always present; the other two contain superlattice reflections, that reflect the crystalline ordering. Only in the $L2_1$ ordered state the (111) reflex is present; in the B2 ordered state the (200) reflex can be found[1]. For that reason the X-ray analysis in this work was focused on these two reflections (see chapter 7.1).

### 3.2.2 Half-Metallicity of Heusler Alloys

The first researchers to identify some of the Heusler alloys as half-metallic materials were de Groot *et al.* in 1983 [23]. They performed band-structure calculations on some Mn-based Heusler alloys like NiMnSb and discovered what they called "unusual electronic properties": The majority spin electrons were metallic, whereas the minority ones were semiconducting. This so called "half-metallic" behaviour requires non-zero density of states for one spin direction (majority) and a band gap for the other direction (minority). It turned out later that the

---

[1] A list of the peak positions of the X-ray reflections can be found in in Appendix D.

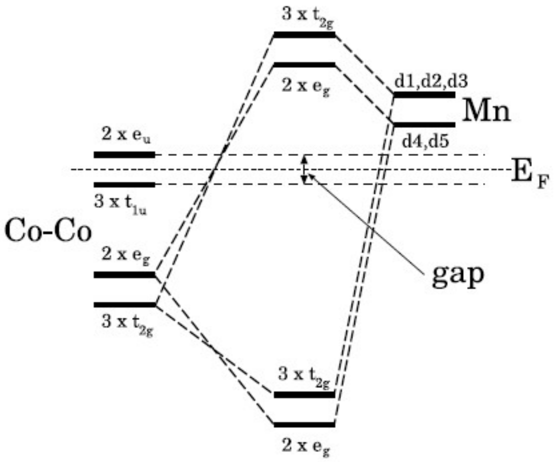

Figure 3.2: Schematic illustration of the Co-Co-Mn hybridization which leads to the gap in the minority band of $Co_2MnSi$. The abbreviations d1, d2, d3 stand for $d_{xy}$, $d_{yx}$, $d_{zx}$; d4 and d5 for $d_{r^2}$ and $d_{x^2-y^2}$ respectively (picture taken from [24]).

hybridization of the $d$ bands of the transition metals in a Heusler compound is crucial for the formation of the band gap. In a compound which contains different materials the exchange splitting between spin up and spin down will be different for the different atoms. After the hybridization the resulting band structure will therefore be different for spin up and spin down, which leads to the observed gap in only one spin direction. In the case of $Co_2MnSi$ the gap is a result of the Co-Mn hybridization ($d$ states) which leads to eight filled and seven empty minority bands; the Fermi level is situated in between the five Co bands [24]. This is illustrated in figure 3.2.

Band structure calculations have been performed by many groups for a variety of half- and full-Heusler alloys, using different computational models. Examples for $Co_2MnSi$ can be found in references [25–28]. These calculations lead to the spin-resolved density of states (DOS) which is depicted in figure 3.3.

In contrast to theoretical predictions of half-metallicity 100% spin polarization has not been observed in experiments yet. There are several reasons for that which have been examined theoretically: The half-metallic character of Heusler alloys can be reduced or even destroyed when disorder occurs in the films. Picozzi *et al.* have calculated that atomic swaps in CMS as well as Mn antisite defects preserve half-metallcity. Co antisite defects however destroy the gap in the minority band, which results in considerable reduction of the spin polarization [29].

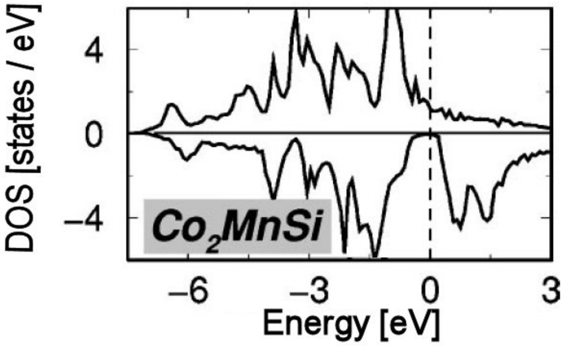

Figure 3.3: Spin-resolved DOS for $Co_2MnSi$ revealing a gap for the spin-down states (picture adapted from [27]).

It has also been shown by various groups that surfaces and interfaces differ greatly from bulk properties for many half-metallic materials. Surface states can turn into interface states that destroy the half-metallic character of the film [30–32]. Hashemifar *et al.* calculated the surface band structure of $Co_2MnSi$ (100) surfaces with different terminations; according to their analyses the pure Mn-termination should preserve the half-metallic character of the surface [33]. Sakuma *et al.* examined the half-metallicity of $Co_2MnSi$ at the surface and interfaces of thin films [34]. By first principles calculations they found out that in the surface density of states of Co the half-metallic character is lost. In a bilayer system with MgO, like in an MTJ, the Co's exchange constant and magnetic moment are reduced; this is considered to be the reason for the rapid decrease of TMR with increasing temperature. In general all half-metallic systems suffer from magnon and phonon excitations at finite temperatures that lead to a reduction of the spin polarization at application-relevant temperatures [35]. Itoh *et al.* have calculated that spin fluctuations at finite temperatures add to the drop of spin polarization and magnetoresistance ratio of half-metallic junctions with increasing temperatures [36].

In addition to that interface oxidation has to be avoided as it results in a significant reduction of the TMR ratio as well: The conductance in the state of parallel magnetization is decreased while at the same time the conductance of the anti-parallel state is increased. These results were calculated by Miura *et al.*, who also pointed out that the likeliness of oxidation depends on the $Co_2MnSi$ termination. The MnSi-termination is more likely to oxidize compared to the Co-

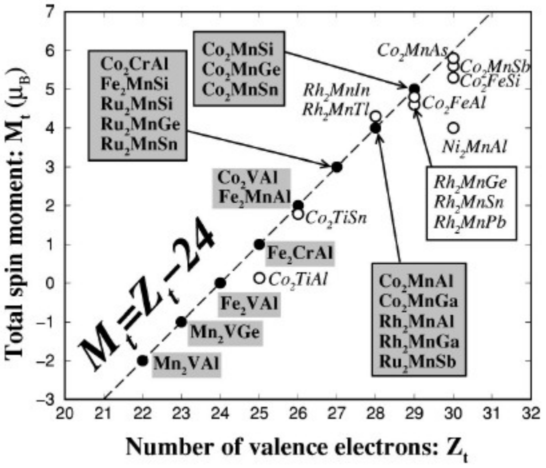

Figure 3.4: Total spin moment as a function of the number of valence electrons for a number of known full Heusler alloys. The dashed line represents the Slater-Pauling rule $M_t = Z_t - 24$; alloys that do not follow this rule are marked with open circles (picture taken from [27]).

termination, so an exact control of the interface termination would be desirable [37]. In practice however, this control is difficult to achieve.

### 3.2.3 Slater-Pauling Behaviour of Heusler Alloys

As shown by a number of groups many full-Heusler alloys, as well as so-called half-Heusler alloys, follow the Slater-Pauling rule [38, 39] which relates the magnetic moment to the number of valence electrons [27, 40, 41]. In the case of half-Heusler alloys this relation is given by $M_t = Z_t - 18$, for the full-Heusler alloys by $M_t = Z_t - 24$. The total spin moment is abbreviated by $M_t$, the total number of valence electrons per unit cell by $Z_t$ in these equations. Figure 3.4 shows the total spin moment as a function of the corresponding number of valence electrons for a large number of full Heusler alloys that have been studied so far. The dashed line represents the Slater-Pauling rule. This rule follows simply because $Z_t = N_\uparrow + N_\downarrow$, where $N_\uparrow$ ($N_\downarrow$) is the number of spin-up (spin-down) bands and $M_t = N_\uparrow - N_\downarrow$. Combining these two and taking into account that 12 minority bands are fully occupied results in the Slater-Pauling rule.

In the case of $Co_2MnSi$ eight of the twelve occupied spin down states are a result of the Co-Co and subsequent Co-Mn hybridization; the remaining four

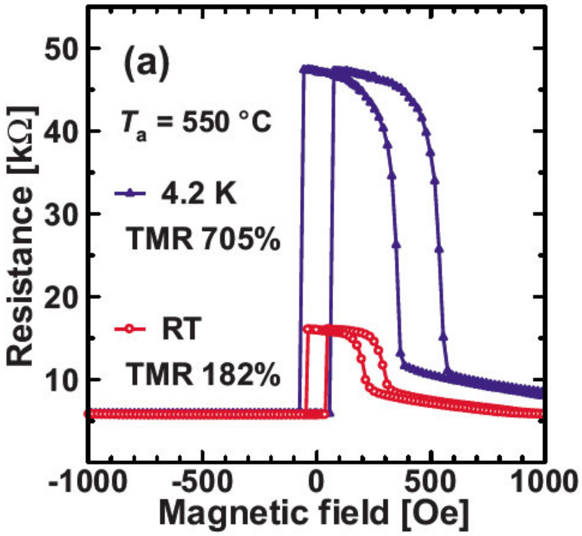

Figure 3.5: Transfer curves at room temperature and 4.2 K for an MTJ with $Co_2MnSi$ electrodes and an MgO barrier (picture taken from [19]).

states are contributed by Si. As $Co_2MnSi$ has 29 valence electrons in total (Co: 9, Mn: 7, Si: 4), the resulting magnetic moment is 5 $\mu_B$/unit cell.

### 3.2.4 Magnetic Tunneling Junctions with Heusler Electrodes

Many groups worldwide have successfully incorporated Heusler alloy thin films into MTJs with either Alumina or MgO tunneling barriers. Considering $Co_2MnSi$ remarkable results were achieved by Sakuraba *et al.* in 2006 with top-pinned Alumina-MTJs stacks: TMR ratios of 570 % were reported at low temperatures of 2K with a system of Cr-$Co_2MnSi$-$Al_2O_3$-$Co_2MnSi$-IrMn-Ta on an MgO substrate [42]. However the pronounced temperature dependence of the TMR ratio led to a modest TMR of only 67 % at room temperature, which is comparable to the results of a stack of CMS-$Al_2O_3$-CoFe presented by the same group [43]. In 2009 Ishikawa *et al.* presented considerably higher TMR ratios of 705 % at 4.2 K and still 179 % at room temperature achieved with a system containing two $Co_2MnSi$ electrodes and an MgO barrier [19]; their result is shown in figure 3.5.

Here again the top-pinned stack was deposited on a single-crystalline MgO substrate. In both cases the Heusler bottom and top electrodes were annealed in-situ directly after their deposition, before the IrMn antiferromagnetic film had been deposited. This procedure reduces the risk of interdiffusion, especially of Mn into the electrode and barrier.

In all results published so far the experimentally determined spin polarizations lag behind the theoretical predictions of 100 % spin polarization. In 2005 Schmalhorst *et al.* achieved a spin polarization of 65.5 % at 20K, determined by measuring the TMR ratio of $Co_2MnSi$-AlOx-$Co_{70}Fe_{30}$ junctions and applying Jullière's formula 3.1 [44]. The above mentioned junctions by Sakuraba *et al.* yielded a spin polarization of 89 % for the bottom CMS electrode at 2K; using this value the top CMS electrode's spin polarization was calculated to be 83 % at the same temperature [42]. Given the theoretical considerations concerning surfaces and interfaces mentioned above these reduced values confirm these calculations.

## 3.3 TMR with MgO Barriers

Apart from using a highly spin-polarized electrode material, a second possibility to improve the TMR effect is to use an optimized system of ferromagnet(100)-barrier(100)-ferromagnet(100). It has been theoretically predicted by Butler *et al.* in 2001 that an MTJ consisting of Fe(100)-MgO(100)-Fe(100) should yield a very high TMR in the order of several hundred percent at room temperature due to coherent tunneling [3].

The concept of coherent tunneling can be explained qualitatively as follows (an exact calculation can be found in [45]): Due to a relatively small lattice mismatch between Fe(100) and MgO(100) of only 3% an epitaxial system of Fe(100)-MgO(100)-Fe(100) can be grown. In such an epitaxial system the tunneling probability is highest for the $k_{\|} = 0$ direction, which is the [100] direction in this case. In the MgO(100) band gap there are three different kinds of evanescent states with different symmetries: $\Delta_1$, $\Delta_5$ and $\Delta_{2'}$ (see figure 3.6). As the symmetries of the wave functions should be conserved, $\Delta_1$ Bloch states from the Fe electrode couple with $\Delta_1$ evanescent states in the MgO only; the same is true for the other symmetries. It has been shown by first principle calculations that the $\Delta_1$ evanescent states have the longest decay lengths and are therefore dominating the tunneling process [3]. This is shown in figure 3.7. As the $\Delta_1$ band in Fe (as well as in e.g. Co) is fully spin polarized at the Fermi energy, a very large TMR is expected.

The first experiments on epitaxial Fe(100)-MgO(100)-Fe(100) systems by

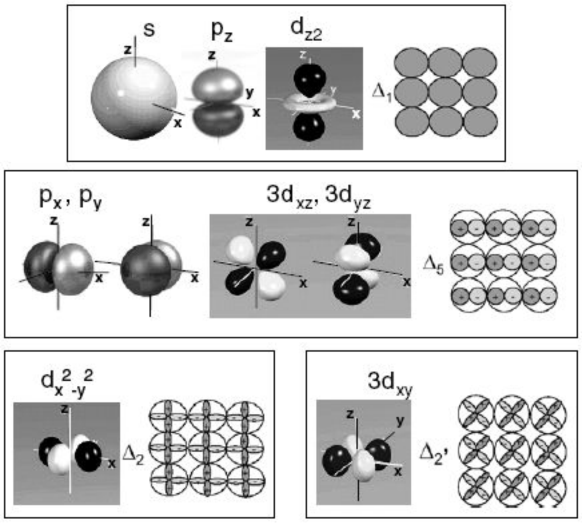

Figure 3.6: Atomic orbitals grouped according to their symmetry, i.e. number of nodes in the plane of the interface. The $\Delta_1$ states are the most important ones concerning tunneling in Fe(100)-MgO(100)-Fe(100) MTJs (figure taken from [46]).

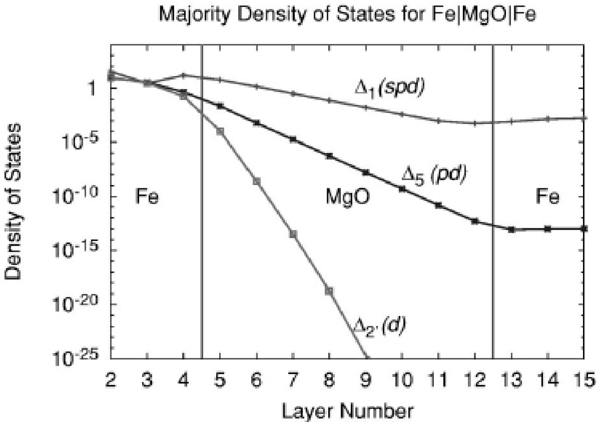

Figure 3.7: Density of states of majority spin states for $k_\parallel = 0$ for Fe(001)-MgO(001)-Fe(001). The $\Delta_1$ state has the slowest decay and will therefore dominate the tunneling process (figure taken from [3]).

Keavney *et al.* in 1997 had not been successful; they measured only ohmic current-voltage characteristics due to pinholes in the MgO barrier [47]. In 2004 Parkin *et al.* found a TMR ratio as high as 220 % at room temperature using CoFe(100) electrodes and an MgO(100) barrier [48], at the same time Ando *et al.* fabricated Fe-MgO-Fe MTJs that reached a maximum TMR of 180 % at room temperature [49]. The problem with these epitaxial (100) systems for applications however is, that they cannot be integrated into standard spinvalve systems easily. The typical layer stack consisting of seed layer / synthetic ferrimagnet (SyF) usually forms an fcc (111) structure, which is not compatible to the (100) structure formed by the electrode and barrier. However, these SyF structures are known to be advantageous for applications because they are magnetically robust and have a negligibly small stray field acting on the top free layer [6]. Therefore they should be part of a TMR sensor stack as well; developing an alternative SyF-system in (100) orientation would be too large an alteration and would also require a long time of research. As a result, a different approach to make use of the favourable coherent tunneling in ferromagnet-bcc(100)- barrier(100) junctions had to be found.

## 3.4 The System CoFeB-MgO-CoFeB

To overcome the problems of matching the (100) textured electrodes to an (111) textured SyF structure, Djayaprawira *et al.* introduced amorphous CoFeB electrodes in combination with a crystalline MgO(100) barrier [4]. They used a standard spin-valve structure on a Si substrate and sputter deposited a CoFeB-MgO-CoFeB trilayer. The resulting TMR was surprisingly high, 230 % at room temperature, although the electrodes' structure remained essentially amorphous, even after annealing. The MgO barrier however, showed a (100) fiber structure even though it was grown on an amorphous layer.

In the following years a number of groups worldwide continued to work on CoFeB systems. The TMR ratios that were achieved were continuously increasing, in 2008 Ikeda *et al.* published a maximum TMR of 604 % at room temperature after a 525°C annealing [50]. In contrast to Djayaprawira *et al.* they used a pseudo-spin-valve structure, which did not contain any antiferromagnetic material. Therefore those systems are of pure academic interest but cannot be employed in a real device.

As mentioned above the main advantage of amorphous CoFeB over crystalline

Co or Fe electrodes is the possibility to integrate them into standard spin-valve systems. These stacks usually contain a bottom pinned electrode where IrMn or PtMn are used for exchange biasing the system. Both, IrMn and PtMn, grow in (111) direction and are therefore not compatible with Co(100) or Fe(100) [51]. Because CoFeB in the composition of $Co_{40}Fe_{40}B_{20}$ is amorphous after deposition and only crystallizes upon annealing, this ferromagnet can be grown on any underlying film and is therefore perfectly suited. Different compositions, like $Co_{80}Fe_{10}B_{10}$ however are not completely amorphous after the deposition; therefore their structure depends greatly on sputtering parameters and seed layer material which makes them difficult to handle [52]. Another advantage of CoFeB is that MgO crystallizes well on CoFeB and some publications suggest that MgO acts as a template for the crystallization of both, top and bottom CoFeB due to very good lattice matching between MgO(100) and CoFeB(100) [6].

Tsunekawa *et al.* found out that the cap layer on top of the CoFeB electrode has a strong influence on the resulting TMR effect as well [6, 53]. Standard cap materials like Ru or Ta lead to high TMR effects whereas materials like NiFe, which are typically used in GMR spinvalve systems, result in a comparatively low TMR. The reason for this is the different crystallization upon annealing: NiFe starts crystallizing at lower temperatures than MgO, therefore NiFe will be the template for CoFeB. As NiFe crystallizes in an fcc(111) structure, CoFeB will also form an fcc (111) structure, which significantly reduces the TMR because coherent tunneling of $\Delta_1$ electrons is impossible. Similar results were found by Park *et al.* when they analyzed the influence of top and bottom adjacent materials: For e.g. NiFe they found the "wrong" (110) orientation of CoFeB, whereas MgO and CoFe made CoFeB crystallize in (100) orientation [54]. Ibusuki *et al.* favoure Ti over Ta or Ru as capping material, as they found even higher TMR for Ti-capped MTJs [55]. They suggest that Ti absorbs B from the CoFeB electrode, which enables crystallization and thus high TMR even after moderate annealing. However, Ti was not available at Sensitec; for that reason, unless stated otherwise, Ru was chosen as cap material for all TMR stacks presented in this thesis.

Several publications suggest that the CoFeB crystallization does not only depend on the neighbouring material but also on its thickness: Kim *et al.* found out that CoFeB crystallizes at lower temperatures if the adjacent MgO layer is thicker [56]. They compared CoFeB thin films on 3nm and 10nm of MgO and observed complete crystallization in the second case after 320°C annealing while the first sample was only partly crystallized. This result and several experiments by other groups indicate that B segregates from the electrode to neighbouring layers. For example, You *et al.* verified by TEM analyses that B segregates from the interface [57] and Bae *et al.* performed XPS analyses of CoFeB-MgO-CoFeB junctions and found B-oxide at the electrode-barrier interface [58].

# Chapter 4

# Sample Preparation

All samples described in this thesis were fabricated using a *Veeco* PVD cluster tool. The annealing can only be done *ex situ* in three different ovens. The samples are structured using standard processes like UV projection lithography, Ar ion etching and sputter deposition of $Al_2O_3$ insulation and Au contacts.

All machines in the Sensitec production line are suited for handling 5-inch wafers. Therefore 5 inch Si substrates covered with an oxide layer were used for sputtering whenever samples needed to be structured.

In this chapter the production steps for the preparation of magnetic tunneling junctions will be described briefly; a generic process flow can be found in Appendix B.

## 4.1 The Sputtering Tool

The *Veeco* sputtering tool (called "PVD 2") consists of three sputtering chambers: a six-target dc magnetron chamber ("PM 4"), a six-target Ion Beam Deposition chamber ("IBD") and a single-target dc magnetron chamber ("PM 5") which is mainly used for reactive processes. A typical target configuration for the three chambers is listed in table 4.1. The three chambers are connected by a transport module with a robot handler that automatically transfers the wafers from one chamber to the next or to one of the two load locks. The whole system is software controlled.

In order to guarantee good film quality, i.e. homogenous film thickness over a five inch surface, the targets are considerably larger than the wafers. The targets in PM 4 and PM 5 are 300 mm in diameter, the targets in the ion beam chamber

| **chamber** | **Pos. 1** | **Pos. 2** | **Pos. 3** | **Pos. 4** | **Pos. 5** | **Pos. 6** |
|---|---|---|---|---|---|---|
| IBD | Cr | NiFe | NiFeCr | $Co_{90}Fe_{10}$ | MgO | CMS |
| PM 4 | Ta | $Co_{90}Fe_{10}$<br>CCFA | $Co_{40}Fe_{40}B_{20}$<br>Cu | Ru | CFAS<br>NiFe | IrMn<br>PtMn |
| PM 5 | Al<br>Mg | | | | | |

Table 4.1: Typical target configuration for PVD 2. The upper line displays the usual configuration, the second line lists alternatives. The targets cannot be interchanged between the chambers due to geometry factors. The abbreviations for the Heusler alloys stand for: CMS = $Co_2MnSi$; CCFA = $Co_2Cr_{0.6}Fe_{0.4}Al$; CFAS = $Co_2Fe_{0.5}Al_{0.5}Si$

are 200 mm in diameter. During the sputtering process the wafers rotate to optimize film homogeneity. Additionally the shutter always moves into the same direction during opening and closing in order to prevent one side of the wafer to be sputtered slightly longer. As this machine was designed for the deposition of high performance GMR multilayers and spin valves the deliberate deposition of uneven films, like wedges, is impossible. To test different thicknesses of e.g. a tunneling barrier, new samples had to be deposited each time.

The deposition rates are determined by a simple contact profilometer measurement; the uniformity of metallic layers over a five inch wafer is monitored with the help of resistance measurements. On a regular basis deposition rates were verified with X-ray reflectometry.

## 4.2 TMR Layer Stack

A complete TMR stack consists of at least three films: the bottom electrode, the tunneling barrier and the top electrode. Seed and cap layers as well as an antiferromagnetic layer (IrMn or PtMn) to magnetically ”pin” one of the electrodes are also needed. Although PtMn has a greater high-temperature stability IrMn was chosen as antiferromagnet because of its significantly lower hysteresis [59]. The ferromagnetic electrodes are mostly deposited by dc magnetron sputtering in PM4. However, some of the electrode materials and some seed layer materials are deposited using ion beam deposition.

In a TMR stack with conventional electrodes all metallic layers are deposited by dc magnetron sputtering in PM4; only the tunneling barrier is deposited in a different chamber. In case of an alumina barrier PM5 is used, in case of MgO the barrier is deposited in the IBD chamber (see section below 4.3). TMR stacks containing $Co_2MnSi$ Heusler electrodes on the other hand were mostly prepared in the Ion Beam Chamber; only the cap and optional pinning layer were deposited in the PM4.

## 4.3 MgO Barrier Deposition

Different sputtering techniques were used for the preparation of the MgO tunneling barrier: pulsed dc sputtering and ion beam deposition, both assisted and not assisted. In the following chapter the different preparation methods will be discussed in detail.

### 4.3.1 Pulsed dc Sputtering

When starting with the development of an MgO process similar conditions as for the preparation of $Al_2O_3$ layers were used: A metallic Mg target was installed and the sputtering was done reactively in an argon-oxygen atmosphere. For this process the single-target reactive chamber was used.

However, only moderate TMR results (approx. 15 %) were achieved with this process after more than a year of optimization work. For that reason this process was discarded. A possible explanation for the low TMR values is that instead of being crystalline and (100) oriented as required for coherent tunneling, the barrier remained essentially amorphous. This has been reported by groups that have experimented with reactive sputtering from metallic targets before [60]. For future experiments, especially with delicate electrode materials, the Mg target might be of use in an Mg-MgO double-barrier-process.

### 4.3.2 Ion Beam Deposition

Ion Beam Deposition (IBD) of MgO for the use as tunneling barrier is unusual, but not completely new. Cardoso *et al.* published first results on IBD TMR stacks with an MgO barrier in 2008 [61], shortly after the work in Mainz had begun.

In dc sputtering processes a voltage between the target and the substrate is applied, an inert gas (typically Ar) is let into the chamber and forms a plasma in the electromagnetic field. The Ar ions are then accelerated onto the target where they can eject atoms from the surface. These atoms are in turn deposited onto the substrate. This method however does only work for metallic targets, sputtering from oxidic targets would result in charging.

In an IBD system on the other hand the ions are generated in a separate gun, not directly at the target. A system of grids accelerates the ions onto the target and the sputtering process starts. Because no voltage is applied directly at the target, this method is also suitable for sputtering insulating materials like, in this case, MgO. Another advantage of the ion beam process is that one can operate at a lower pressure than in standard sputtering processes, which reduces the risk of contamination.

The base pressure of the IBD chamber used here is $2 \cdot 10^{-8}$ torr, typical deposition pressures are in the order of $10^{-4}$ torr. The chamber is equipped with two ion guns: the deposition gun, which is directed at the target and the etch gun, which is aimed directly at the wafer surface. The orientations of the guns within the chamber can be altered within the range of a few degrees. Both guns are equipped with two gas inlets that can be switched independently. The deposition gun typically uses xenon, however argon is also available. The etch gun is connected to Ar and $\mathrm{Ar/O_2}$ (20 % $\mathrm{O_2}$). In addition to that a background gas inlet was added in the course of this project in order to increase the variety of parameters for MgO optimization. Currently the etch gun's $\mathrm{Ar/O_2}$ mixture is attached to the background gas inlet.

The distance between target and wafer is fixed to about 25 cm; this distance cannot be changed. In order to improve wafer uniformity the targets are considerably larger than the wafers, their diameter is 200 mm. The targets are situated in a cylinder which is rotated until the required target faces the chamber. There are two shutters, one for the target and a second one for the substrate. This allows e.g. pre-sputtering for target conditioning without coating the wafer. During the deposition process the wafer rotates, the rotation speed can be defined in the process recipe. As the sputtering tool is a production tool the whole setup is optimized for wafer uniformity. It is impossible to deliberately deposit an inhomogeneous film, like e.g. a wedged barrier. As a result variations of barrier thicknesses have to be deposited on single wafers each, which means that a large number of wafers has to be processes for thickness optimizations.

## 4.4 Annealing the Samples

Unfortunately there is no possibility to deposit at elevated temperatures or anneal samples *in situ* in the PVD, therefore all samples have to be annealed *ex situ* after the complete stack has been deposited. This is especially disadvantageous for TMR stacks with Heusler alloys, as the Heusler thin films require relatively high annealing temperatures of 350°C or even higher (see chapter 3.2.4). At Sensitec there are three different ovens suitable for annealing TMR samples: A so-called *High Field Reset Oven* (HFRO) by *Despatch* and two smaller ones by *Blue M Electric* and *YES*. The HFRO can generate magnetic fields up to 1.3 T, but its temperature is limited to 265 ℃. This oven works under nitrogen atmosphere, the wafers are placed on special holders where the position of the wafer notch (i.e. the orientation of the wafer within the magnetic field) is fixed. Up to fifteen 5 inch wafers can be annealed simultaneously. In the *Blue M* oven samples can be annealed up to 500 ℃. However, this oven does not have a magnet, so it cannot be used for defining exchange coupling. In the past it had been equipped with a permanent magnet but this magnet was removed in the course of this work for production reasons. The *Blue M* oven works in an $N_2$ atmosphere as well, the pressure during the process is always kept slightly above atmosphere in order to prevent air from entering the chamber.

The third oven, a *YES* oven, is similar to the *Blue M* oven, the samples are annealed in an moderate positive nitrogen working pressure, no magnetic field can be applied. The maximum working temperature is lower than in the *Blue M* oven, however this oven was used temporarily because the *Blue M* oven had an oxygen leakage.

TMR samples were typically annealed twice: firstly in the *HFRO* to define pinning and secondly in the *Blue M* or *YES* oven to fully crystallize the barrier. Single films for X-Ray analyses were only annealed once, either in the *Blue M* or the *YES* oven.

## 4.5 Structuring the Samples

All Sensitec machinery is designed for handling circular 5 inch wafers. For that reason these wafers were always used whenever samples needed to be structured in Mainz. All together three mask layers are necessary to define the bottom electrode, the junction itself and the top electrode which is contacted later. A

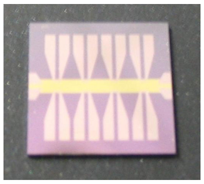

Figure 4.1: TMR chip with an edge length of 10mm. The horizontal line is the bottom electrode which is contacted at the left and right. The vertical lines are the contacts of the upper electrode (see Appendix A for the mask drawing).

picture of the final chip is shown in figure 4.1. Each chip consists of eight junctions that are arranged in two identical rows with four circular junctions each. Their diameters ascend from 16 $\mu$m to 50 $\mu$m. The chip design is kept as simple as possible, the chips' only usage is to be able to measure the TMR ratio. The chip's edge length is 10 mm which allows easy handling after dicing. The contact pads are large enough to ensure easy manual probing if needed.

After sputtering and a first annealing step the bottom electrode is defined lithographically. Therefore the wafers are spin coated with positive photosensitive resist (AZ® ECI 3012) of 1 $\mu$m thickness [63]. After a softbake step they are exposed with UV light (365 nm) by a *Canon FPA-3000MR* i-line wafer stepper. After developing the resist in metal ion free developer (AZ® 300 MIF)[1] only the bottom electrode and the base for the later top contacts are left. Afterwards the structure is ion milled in a *Veeco* Ion Milling tool at an angle of -10° with respect to the normal. In order to improve wafer homogeneity the wafer rotates continuously with 10 rpm. As the ion milling process uses highly energetic ions (300 V, 500 mA) the resist is hardened and irremovable by chemical means alone. Therefore the resist is exposed to an oxygen plasma first and then removed with warm N-Methylpyrollidone (NMP).

To structure the actual MTJs the wafers were spin-coated with a double-layer resist in order to define a so-called "undercut". This is necessary if lift-off processes are used and describes a "T"-like resist structure in which the bottom resist is washed out. After sputtering a narrow slit is left between the metal and the resist allowing the remover to affect the resist. The bottom resist, LOR 1A by *MicroChem Corp.*, is a non-photosensitive resist based on PMGI (polydimethyl-

---

[1] AZ® 300 MIF is an aqueous solution of 2.38% tetramethyl-ammonium-hydroxide (TMAH) without any surfactants [64].

glutarimide) [65], as a top resist AZ® ECI 3012 is used. After the softbake of both resists the wafers are exposed with the *Canon* stepper and developed with AZ® 300 MIF. The resulting MTJs are circular pillars with different diameters ranging from 16 to 50 $\mu$m. The following ion milling process is designed to stop shortly below the tunneling barrier. This process is critical and is therefore monitored carefully. For the monitoring half-stacks were sputtered on glass coupons, etched and the transmission of light was then measured with the help of a densitometer.

After the ion milling process the resist is not removed, but used as a mask during the sputtering of the passivation layer (gap refill). 60 nm of Aluminum oxide are used to isolate the top electrode from the bottom one. The resist is stripped afterwards with warm NMP in a spray stripper tool.

The last photolithography layer is needed to structure the leads and contact pads. Again a double-layer resist (LOR 5A + AZ® ECI 3012) is applied, soft-baked and the wafers are exposed and developed. 40 nm of Ta as adhesion promoter and 200 nm of Gold are sputtered to ensure a good electrical conduction and contact for testing the samples. After removing the resist with NMP the wafers are ready for testing.

The structuring process is visualized schematically in figure 4.2.

## 4.6 Quadrants-Wafer

As mentioned above all Sensitec machinery is only capable of handling 5 inch wafers. However, for research projects like this one normally only a few samples are needed. Sputtering and structuring a whole wafer is therefore a waste of time and substrates. So a method to use the wafer surface more effectively was developed: A 4 inch wafer with one quarter being sawn out was used as a cover during the deposition of the TMR layer stack. After the first sputter run the cover was removed, rotated by 90 degrees and another TMR stack was sputtered on the same wafer. With this technique four different stacks could be deposited on only one wafer. The advantage of this was that a larger variety of stacks could be tested within a lot of nine wafers or the other way round a smaller amount of wafers was needed which means lower cost and faster processing. The effectively used area of the wafer was reduced from 5 inch to 4 inch in diameter, but there were still enough samples in one quadrant.

It is striking to note that placing a wafer on top of a TMR layer does not destroy the stack. In various tests not more short-circuited elements were found

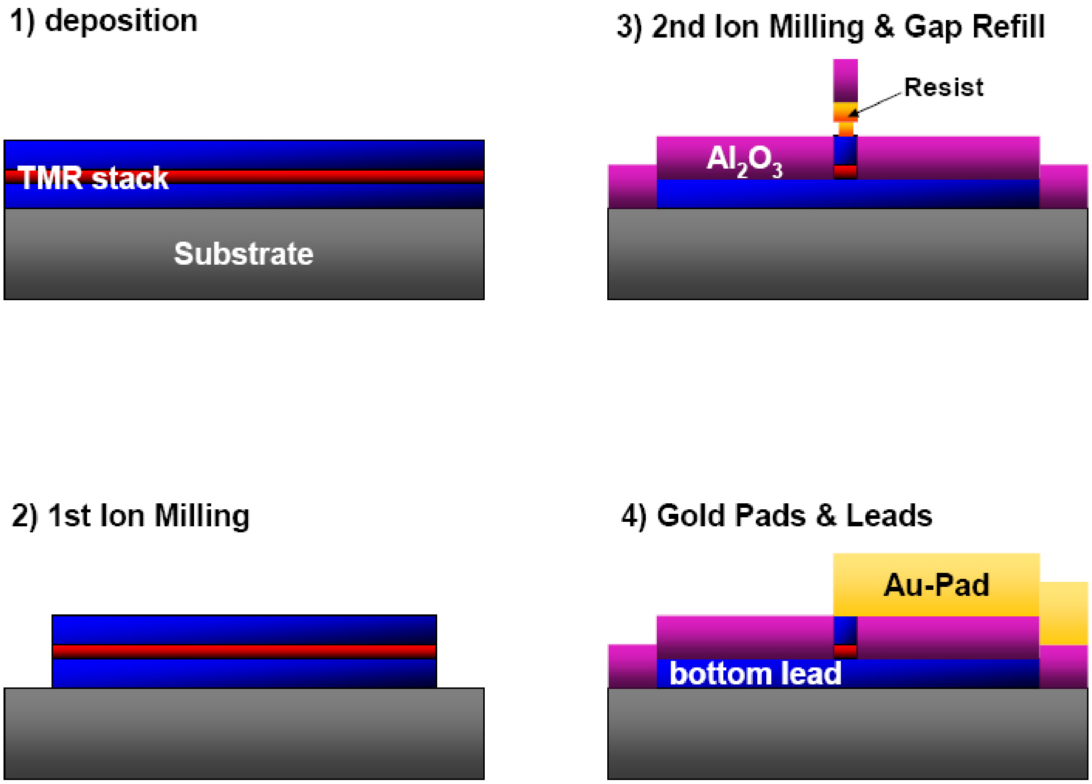

Figure 4.2: Schematic structuring sequence (not to scale). The blue-red-blue trilayer symbolizes the MTJ with the tunneling barrier drawn in red.

on a quadrants wafer in comparison to a ”normal” full-film wafer.

## 4.7 TMR Tester

A fully automatic TMR tester for five inch wafers was developed at Sensitec during the time of this thesis. The tester is based on an *Electroglass* prober that was upgraded with a permanent magnet which can be moved along a vertical axis. The maximum magnetic field is about 1700 Oe, the minimum field with the magnet moved to the uppermost position of the axis is 6.8 Oe. This constraint implies that un-pinned MTJs are difficult to test because there is no data point at zero field.

A probecard contacts all top electrode pads along one row of junctions and the bottom electrode. This configuration allows testing four junctions almost simultaneously. Measurements with constant current as well as constant voltage are possible. The standard procedure at Sensitec is testing with constant current; this procedure was adopted for the TMR measurements, too. Normally the wafers were tested using a constant current of 10 $\mu$A. The TMR tester allows testing at room temperature only. Therefore all TMR results presented in this thesis are always room temperature results.

# Chapter 5

# MgO Barrier Optimization

The tunneling barrier is the heart of a TMR stack, therefore optimizing this layer is crucial for the performance of a TMR device. In this chapter the optimization of the ion beam deposited MgO barrier will be described comprehensively.

## 5.1 Seed-Layer Optimization

Before the optimization of the ion beam process itself an ideal seed layer had to be found. Seed layers influence the growth of the electrode materials, which in turn influences their texture and roughness [66]. Only materials that were present in the sputtering system were considered as possible seed layers: Ta, Ru, NiFeCr, NiFe, MgO. To compare the results, identical stacks containing $Co_{40}Fe_{40}B_{20}$ 4nm - MgO 2nm - $Co_{40}Fe_{40}B_{20}$ 3nm were deposited on 5 inch Si wafers with variable seed layers and then annealed twice [1]. The first annealing was done at 300°C in a low magnetic field of 2000 Oe [2], the second annealing was done at 265°C in a higher field of 5000 Oe. The wafers were measured using the TMR tester setup in Mainz.

Figure 5.1 and figure 5.2 show the averaged measured TMR and RA values for the different seed layers that were tested. In the first graph data for the MgO standard process is shown, the second graph contains data for the IBAD barrier process. Both results show clearly that the combination of Ta-Ru-Ta is favourable, an additional MgO seed underneath is counterproductive. Magic

---

[1] Whenever CoFeB was used it had the composition $Co_{40}Fe_{40}B_{20}$; the exact composition will therefore be omitted in the remaining thesis.

[2] The first annealing was done in the *Blue M* oven, which still contained a permanent magnet at this tine.

Seed (NiFeCr / NiFe bilayer), with or without MgO underneath, does not seem to work in TMR junctions.

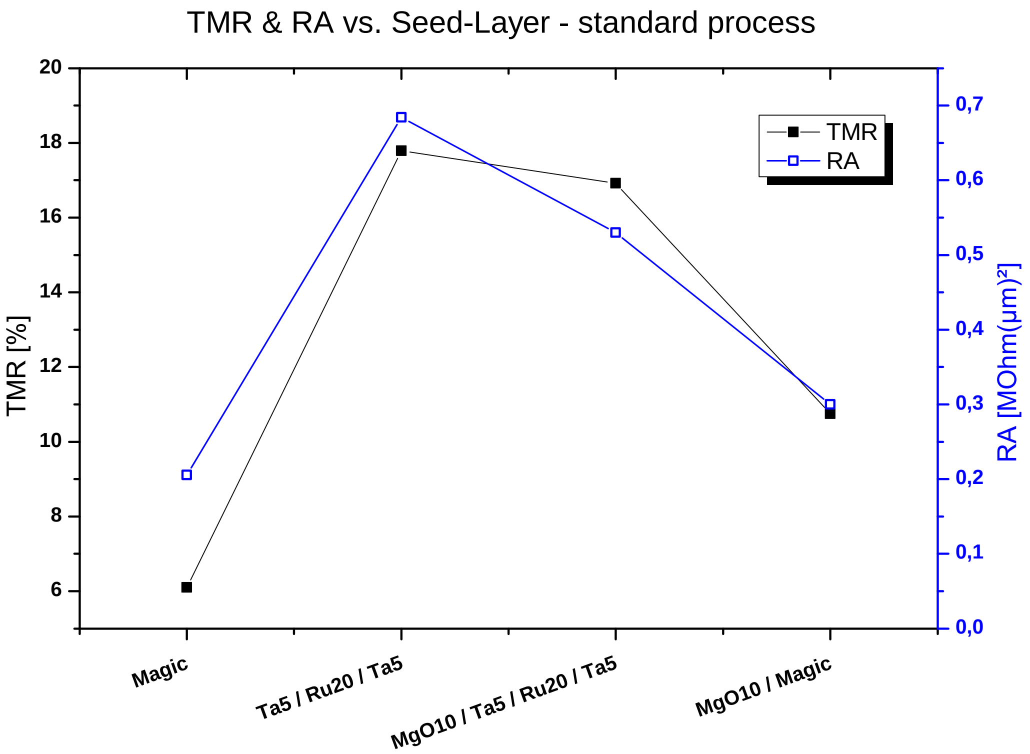

Figure 5.1: TMR and resistance-area-product for CoFeB-MgO-CoFeB stacks with different seed layers, where the MgO barrier has been deposited using the standard ion beam deposition process (the numbers represent the thickness in nm). All values are average values of several junctions.

In the IBAD-graph also MgO/Ta looks promising; the average TMR was 46 %. However, in contrast to Ta/Ru/Ta the number of working junctions, i.e. junctions that were not short-circuited, was clearly reduced. Therefore Ta/Ru/Ta was chosen as the optimum seed layer, all further junction optimization work was done with this buffer layer. The big difference between 10 and 20 nm Ru, which is clearly visible in the second graph, never occurred again in later experiments. For that reason only 10 nm of Ru were sputtered.

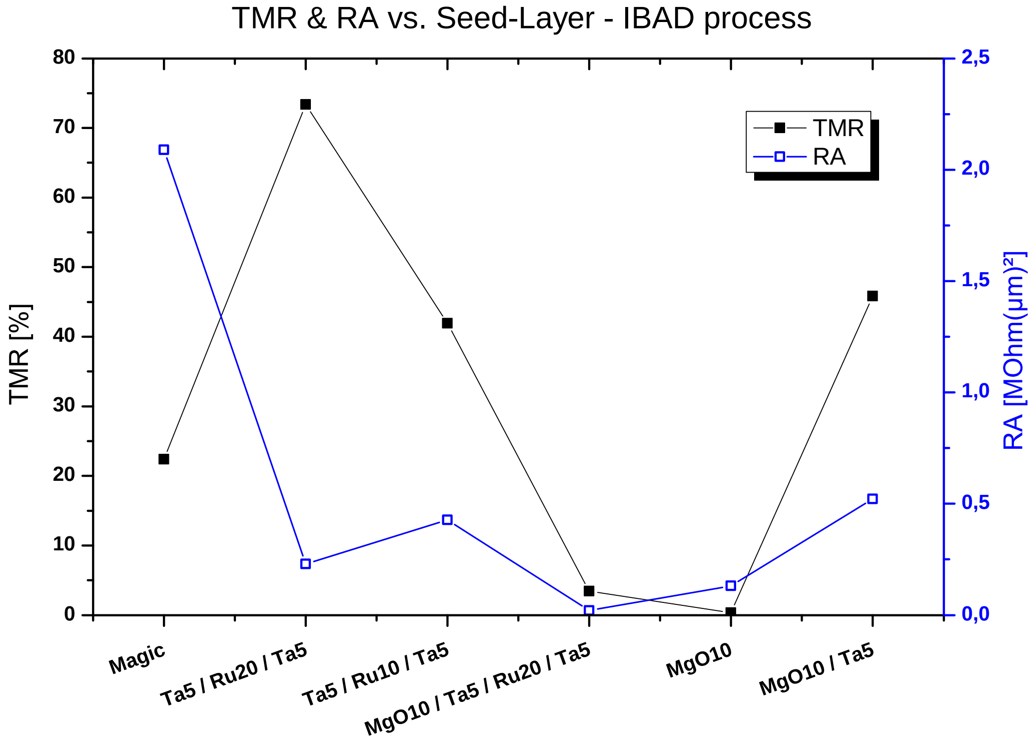

Figure 5.2: TMR and resistance-area-product for CoFeB-MgO-CoFeB stacks with different seed layers, where the MgO barrier has been deposited by IBAD (the numbers represent the thickness in nm). All values are average values of several junctions.

## 5.2 Ion Beam Standard Process

The term ”standard process” refers to the process conditions used for the deposition of metallic layers such as NiFe or CoFe. In that case only the deposition gun is used, the etch gun remains in idle mode (”off”).

However, in order to be able to ablate material from the oxidic MgO target the etch gun has to be switched on to ”source” mode. The reason why it is impossible to deposit MgO without the etch gun is that as soon as the target shutter is opened the oxidic target gets charged, which makes a sputtering process impossible. Apparently the neutralizer filament alone does not produce a sufficient amount of electrons to compensate for the cations being ablated from the target, so the etch gun needs to act as an additional neutralizer. In order to start the etch gun a gas flow is needed; an Ar-flow of 6 sccm was chosen arbitrarily.

All other beam parameters were kept to the parameters used for metallic deposition because these parameters have proven to give the most stable beam condition. The beam voltage was set to 750 V, the beam current to 70 mA; xenon was used as sputtering gas with a gas flow of 2.5 sccm. During deposition the wafer rotates with a constant speed of 5 rpm. This set of parameters results in a deposition rate of 0.2 Å/s. This ”MgO standard process” is very stable; long deposition times up to 30 minutes were tested repeatedly without a change in the beam parameters.

The first wafers that were deposited were meant to find the ideal process time, i.e. MgO thickness. This variation was done only for wafers with magic seed, the MgO thickness was varied from 1.6 nm to 2.2 nm. The samples were annealed twice, first at 300°C followed by an annealing at 265°C and a higher magnetic field.

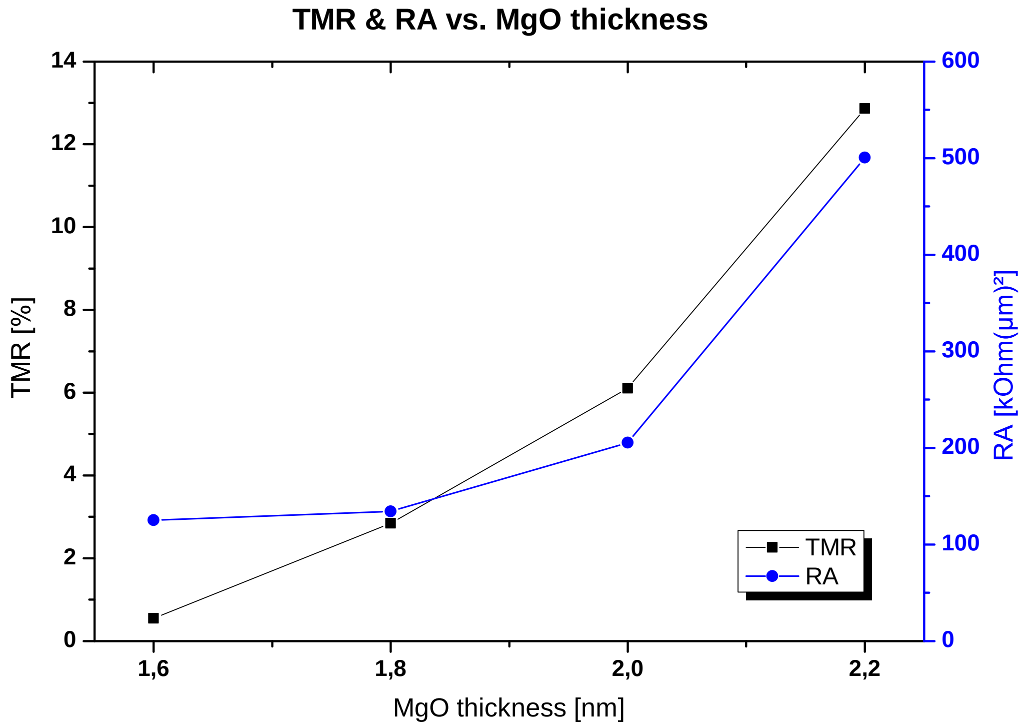

Figure 5.3: TMR and resistance-area-product for CoFeB-MgO-CoFeB stacks with different MgO thicknesses. The barrier was deposited using the standard process. All values are average values of several junctions.

As shown in figure 5.3 both, TMR and RA, increase with increasing barrier thickness. The maximum value in this matrix here is a TMR of almost 13 % at a resistance-area-product of approximately 500 k$\Omega(\mu\mathrm{m})^2$.

## 5.3 Ion Beam Assisted Process (IBAD)

Shortly after the work on the MgO barrier process by ion beam deposition had begun, we became aware of the publication by Cardoso *et al.* [61]. The group from Lisbon produced MgO tunnel barriers by IBD as well; in contrast to our work they made use of their second gun which was directed at the substrate in a shallow angle. They claimed that using an "etch gun" during the deposition process is advantageous for the barrier growth, which they confirmed by X-ray diffraction. TMR results were improved, too: 110 % were achieved with an etch gun, only 30% without it [3].

As mentioned above, in our case the etch gun was operated in "source" mode only until then. Because of the positive results by Cardoso *et al.* an assisted process was tested in our tool, too. In our case the etch gun points directly at the wafer, thereby covering an off-centered spot of approximately 25 % of the wafer's surface. By rotating the wafer homogenous coverage is guaranteed. The standard parameters for etching are 500 V and 60 mA. However, with a deposition rate of only 0.2 Å/s this would result in no deposition at all as the etch rate of 0.8 Å/s is four times higher than that. Therefore the etch beam power was reduced to a stable minimum. Experiments showed that the beam voltage could not be reduced below 300 V and the beam current had its lower limit at 30 mA. Reducing it further results in unstable plasma ignition, reducing the cathode minimum to circumvent this limitation results in instable beam parameters because the beam current can no longer be kept stable during the process. However the gas flow in the deposition gun had to be increased by a factor of four to guarantee a stable plasma; the lower gas flow of 2.5 sccm had repeatedly resulted in charging again. The resulting gun parameters are listed in table 5.1.

The first results were very promising: For an identical stack with the same resistance a TMR of about 20 % was achieved without an etch beam; with etch

---

[3] An IBAD process for MgO had been reported in 1997 already by Wang *etal.* [62]. In their case MgO films down to 10nm were deposited by e-beam evaporation onto amorphous $Si_3N_4$ substrates for the use as structural templates for other materials. An additional assist gun that was directed onto the substrates was used to improve film growth.

| | **Deposition Gun** | **Etch Gun** |
|---|---|---|
| Status | Beam | Beam |
| Beam Voltage | 750 V | 300 V |
| Beam Current | 70 mA | 30 mA |
| Gas | Xe | Ar |
| Gas-Flow | 10 sccm | 12.5 sccm |
| Neutralizer | 3.0 | 3.0 |

Table 5.1: Gun parameters for the MgO Ion Beam Assisted Deposition process (IBAD process).

gun more than 70 % TMR were reached in the first try (see figure 5.4). The stack consisted of the following layers: Si-substrate // $Al_2O_3$ 400 / Ta 5 / Ru 20 / Ta 5 / IrMn 15 / CoFe 3 / Ru 0.8 / CoFeB 4 / MgO 2.0/ CoFeB 3 / Ru 3 / Ta 5 (all thicknesses in nm). This wafer was a quadrant wafer; only two of the quadrants are regarded here (the other contained an Mg underlayer in the barrier and are therefore not comparable to the others). The wafer was annealed at 265°C in a magnetic field of 5 kOe only. The average TMR of about 70 % was the highest TMR value achieved until then. Figure 5.5 shows the TMR distribution over the quadrants wafer containing both, standard and IBAD stacks. The first quadrant (upper left) shows the results for the standard stack with 2.0 nm MgO barrier deposited with the standard process, the second quadrant the same stack with the sole exception that the IBAD process was used for the barrier deposition. Quadrants three and four are stacks with Mg / MgO double barriers that can be disregarded for the moment. One can see that the TMR values are quite homogenously distributed, the first quadrant shows between 19 % and 21 % TMR, the second considerably higher values between 70 % and 77 % TMR.

As a consequence work on the so-called ”standard process” was not continued because it turned out that the ”ion-beam-assisted process (IBAD)” produced by far better results.

In figure 5.6 typical transfer curves are shown for the MgO standard process and the assisted process. For each process one chip with four junctions of different diameter is depicted. One can see, that the difference in TMR arises from a different resistance in the anti-parallel state only.

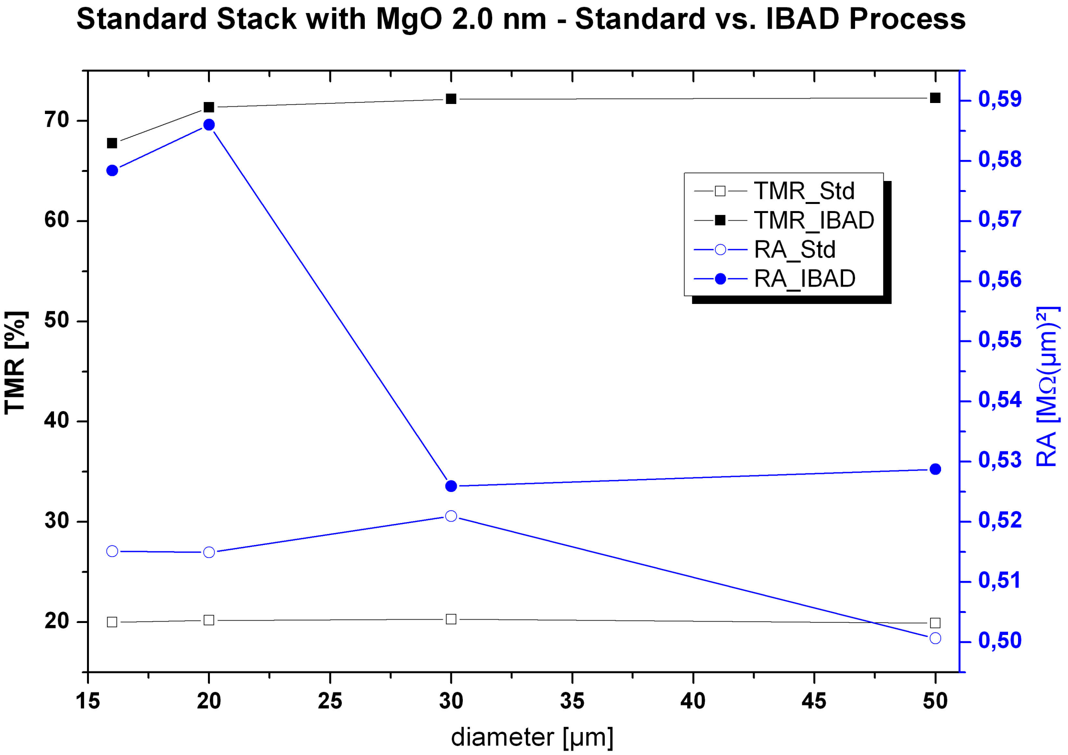

Figure 5.4: TMR and RA for CoFeB-MgO-CoFeB stacks with 2.0 nm MgO barrier. "Std" refers to the MgO standard deposition process with the etch gun in "source" mode; "IBAD" refers to the process with an additional etch beam. All data points are average values of about 10 to 15 junctions; damaged junctions were disregarded.

## 5.4 Low Rate Process

A different approach than using the etch gun to improve the MgO barrier process was to reduce the beam power of the deposition beam in the "standard process". By reducing the beam current to 40 mA (instead of 70 mA in the standard process) the deposition rate was halved. All other deposition parameters, like beam voltage and gas flow, were kept unchanged.

With these parameters TMR ratios of about 20 % after a 265°C annealing were achieved; after a second annealing step at higher temperatures the values increased to about 57 %. The resistance-area product was in the order of 700 $k\Omega/\mu m^2$. These results were not competitive compared to the IBAD process. Therefore this path was not continued.

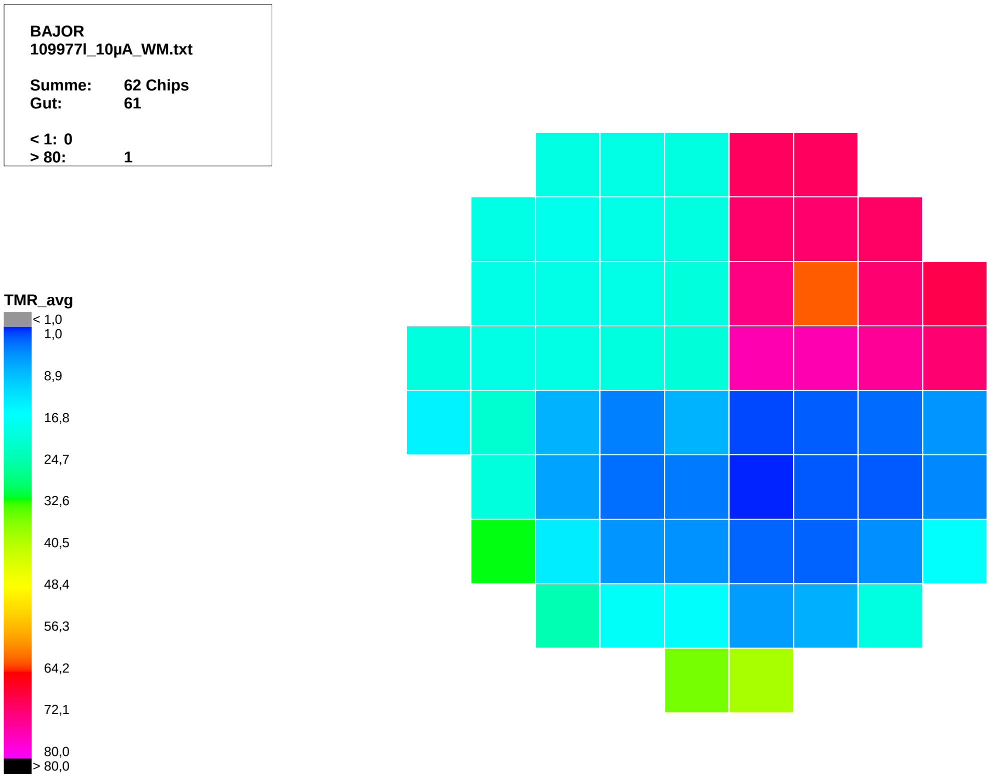

Figure 5.5: TMR distribution for CoFeB-MgO-CoFeB stacks with 2.0 nm MgO barrier. The first quadrant (upper left) shows the standard process, the second (upper right) the IBAD process. All data points are average values of 4 junctions per chip; damaged junctions were disregarded.

## 5.5 Deposition with additional Oxygen

After a few months of experimenting the measured resistance of the junctions decreased steadily. The most likely explanation for that was that magnesium and oxygen were ablated from the target at different rates so that after a while the target had a larger proportion of Mg than it used to at the beginning. To compensate for the oxygen loss reactive sputtering was tested. For all development work the TMR layer sequence was kept unchanged to avoid additional variations that could distort the results. The "standard stack" that was used from then on was built up as follows:

Si-substrate // $Al_2O_3$ 400 / Ta 5 / Ru 10 / Ta 5 / IrMn 15 / CoFe 3 / Ru 0.8 / CoFeB 4 / MgO / CoFeB 3 / Ru 5 (all thicknesses in nm).

The wafers were annealed only once at 265°C in a magnetic field of 5 kOe for

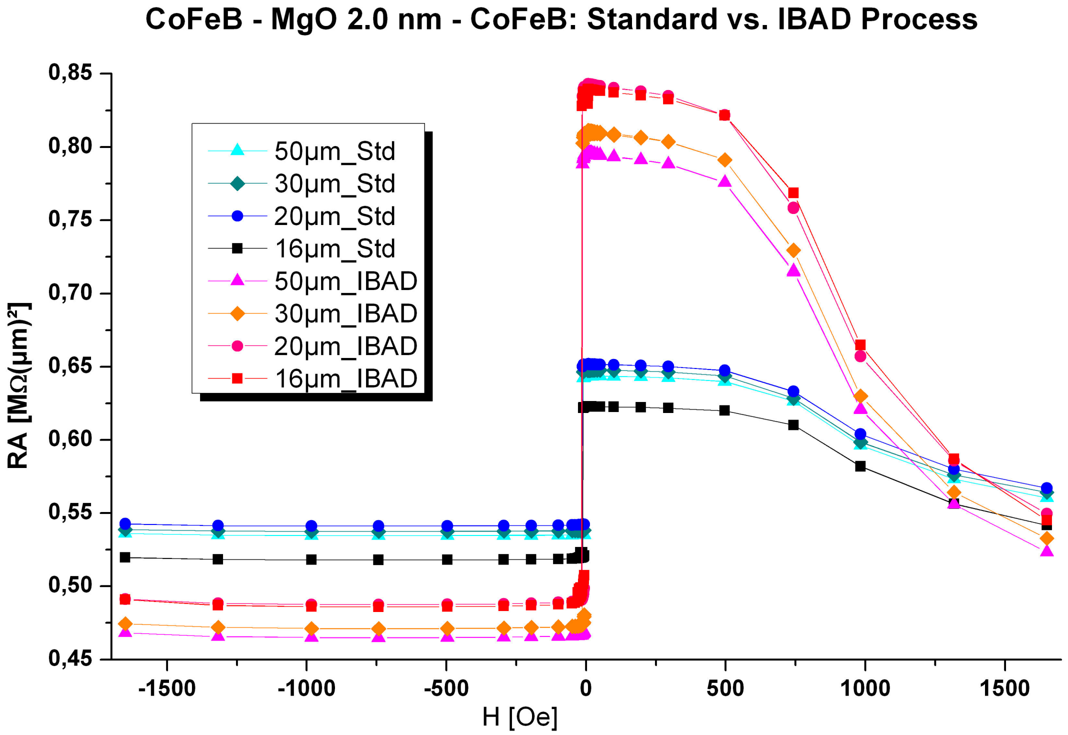

Figure 5.6: TMR transfer curves for CoFeB-MgO-CoFeB stacks with 2.0 nm MgO barrier. The wafer was annealed at 265°C only. For this plot four junctions of the same chip on the same wafer were chosen for each process.

only 10 minutes to induce exchange coupling.

### 5.5.1 Additional Ar/$O_2$ via Etch Gun

The only way to add oxygen during during the deposition process was adding it via one of the etch gun's gas inlets. The gas mixture chosen was an Ar/$O_2$ mixture with 80 % Ar and 20 % $O_2$, the gas flow was set to 1.0 sccm. The aim was to find a sputtering process that produces working TMR barriers with approximately the same resistance as before.

The first wafer was sputtered using the old MgO standard process, i.e. not the IBAD process. This was mainly a safety precaution because etching with oxygen had never been tested before in this machine. Apart from that, the idea of the additional oxygen was to provide oxygen in the chamber, not bombarding the wafer with highly energetic oxygen ions. The deposition rates for the standard and

| **MgO w/o $O_2$ [s]** | **MgO with $O_2$ [s]** | **TMR [%]** | **RA[$M\Omega(\mu m)^2$]** |
|---|---|---|---|
| 0 | 180 | 14.55 | 14.55 |
| 40 | 140 | 22.71 | 1.28 |
| 0 | 200 | 6.42 | 20.50 |
| 50 | 150 | 20.46 | 5.56 |

Table 5.2: TMR and RA for single and double barriers with the same total sputtering time. In all cases an $Ar/O_2$ flow of 1.0 sccm was used.

later also the IBAD process with additional oxygen were checked; the deposition rate remained unchanged in relation to the non-reactive process.

Adding oxygen during the whole MgO deposition process resulted in a tremendous increase in resistance: The resistance-area product reached 10 to 20 $M\Omega(\mu m)^2$, TMR remained low (5 to 27 %). As a result "double barrier" processes were tested and the deposition method was switched to IBAD. Double barrier in this case means depositing a thin MgO layer without additional oxygen and adding a second MgO layer that has been sputtered reactively. The first thin MgO layer was meant to protect the bottom electrode from oxidizing, which is the case if oxygen is flooding the chamber right from the start.

To find the right combination of sputtering without and with oxygen a number of variations with the same total MgO thickness were built; examples are given in table 5.2.

As expected the resulting resistance was lower for the double barrier than for a stack of the same thickness that was completely sputtered reactively. In addition to a protection of the bottom electrode the double barrier process enables the engineer to tune the junction's resistance according to the needs of a specific application by adjusting the ratio of sputtering without and with additional oxygen.

### 5.5.2 $Ar/O_2$ as Background Gas

Using one of the etch gun's gas inlets to add oxygen worked fine, however, this configuration has its limitations. For example it was difficult to find a cathode minimum which guaranteed reliable plasma ignition and stable operating parameters for both, deposition with and without additional oxygen, especially for the IBAD process. Therefore it was decided to modify the chamber hardware and construct another gas inlet that directly leads into the chamber. It was assumed that simply letting gas into the chamber would have less impact on the performance of the ion guns resulting in a more stable process. The background gas was connected to the same gas mixture that had been used before, Ar/$O_2$ with 20 % oxygen. The background gas flow can be controlled by the software like all other gases, it had been part of the general software configuration even though it had not been part of the actual hardware configuration of PVD 2.

The experiments with oxygen via the etch gun inlet had all been done with a gas flow of 1.0 sccm Ar/$O_2$. With a standard deposition time of 200 s the RA-product reached values of more than 20 M$\Omega(\mu m)^2$, which was too high for practical use. It was assumed, that the "softer" process of background gas flooding would be less effective, particularly because of the chamber architecture: The gas inlet and the wafer are localized at opposite positions in the chamber, the cryopump is situated right in the middle between them. As a result most of the background gas will be pumped away before it reaches the wafer (or the target).

Monitoring of sputtering rates was done for only one process (not assisted), there was no difference between sputtering with and without additional Ar/$O_2$. To check the influence of the background gas a matrix with oxygen flows between 0 and 5 sccm was deposited. The MgO deposition time was kept constant at 200s, the stack remained unchanged and all wafers were annealed at 265°C in a magnetic field of 5 kOe.

It turned out that 1.0 sccm of additional Ar/$O_2$ had a tremendous influence on TMR and especially RA; 2.0 sccm was already too much. Therefore a second matrix was deposited with smaller amounts of Ar/$O_2$, reaching from 0.25 sccm to 1.5 sccm. The results of these two matrices are summarized in table 5.3 and visualized in figure 5.7.

A minimum gas flow of 0.25 sccm was tested, but this amount was too small for the valves to regulate: There was no oxygen in the chamber in that run (verified by RGA). The highest TMR values of approximately 45 % were reached with an oxygen flow of 0.5 and 0.75 sccm; the resistance-area-product jumped from 0.8 to 3.4 M$\Omega(\mu m)^2$ in these two samples. These results show again how sensitive the MgO barrier reacts to oxygen. Controlling the gas flow exactly is crucial for generating a precise resistance. The chamber conditioning could also influence the barrier's resistance: If a lot of oxygen-processes have taken place in the chamber before, the chamber walls as well as the target might have a higher oxygen content then before, which in turn could modify the barrier's resistance.

| **Wafer** | **Ar/O$_2$-flow [sccm]** | **TMR [%]** | **RA [M$\Omega$($\mu$m)$^2$]** | **Comment** |
|---|---|---|---|---|
| 701942 | 1.0 | 25.28 | 19.91 | TMR inhomogeneous |
| 701962 | 2.0 | 0.03 | 71.65 | almost no TMR measureable |
| 701963 | 3.0 | 0 | 70.05 | no TMR |
| 701964 | 4.0 | 0 | 74.59 | no TMR |
| 701965 | 5.0 | 0 | 78.59 | no TMR |
| 701966 | 0.0 | 32.17 | 0.22 | |
| 313004 | 0.0 | 33.87 | 0.27 | |
| 313005 | (0.25) | 40.55 | 0.44 | no oxygen in chamber |
| 313006 | 0.5 | 45.74 | 0.80 | |
| 313007 | 0.75 | 46.09 | 3.38 | |
| 313008 | 1.0 | 24.64 | 22.33 | |
| 313009 | 1.5 | 0.64 | 78.76 | |
| 313011 | 0 | 36.37 | 0.20 | |

Table 5.3: TMR and RA values depending on Ar/O$_2$ background gas flow. All results are average values for a whole wafer; the wafers with more than 2.0 sccm were measured only on a sample basis.

To protect the bottom electrode from oxidizing "double barrier" processes were checked as well, similar to the experiments that had been done before with the oxygen from the etch gun. The results were qualitatively the same as before, which had been summarized in table 5.2, but for the IBAD process with background gas TMR ratios as high as 50 % could be achieved.

In summary one can say that reactive sputtering was tested successfully and allows easy adjustment of the junction's resistance. The use of a newly created background gas inlet stabilized the guns' performance in the IBAD process and made double barriers consisting of a non-reactively deposited MgO bottom and a reactively sputtered top part possible.

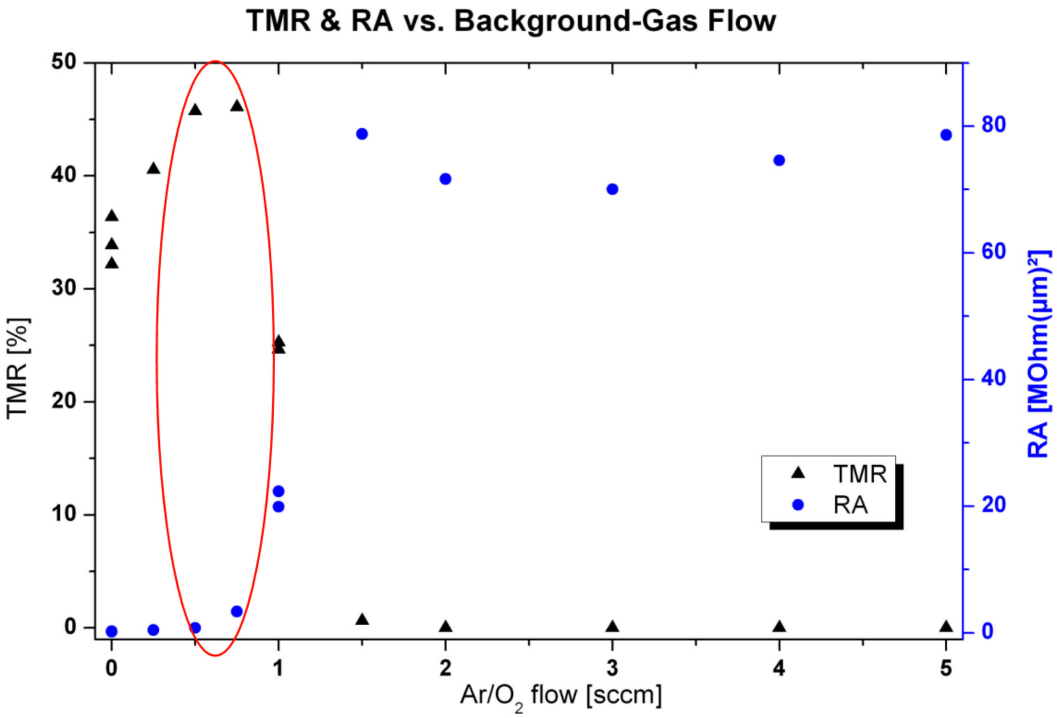

Figure 5.7: TMR and RA for CoFeB-MgO-CoFeB stacks with different Argon-Oxygen flows during barrier deposition. The encircled data marks the optimum gas flow; for more than 1.5 sccm no TMR was measurable. All values are average values of several junctions.

## 5.6 TMR as a Function of the Annealing Temperature

The standard TMR process contained only a moderate annealing at 265°C in a magnetic field of 5kOe for only 10 minutes. This process step fulfilled a double function: On the one hand the MgO barrier was crystallized to improve TMR and on the other hand the exchange bias was induced in the bottom synthetic antiferrimagnetic structure. Depending on the layer stack this typically yielded in TMR values between 30% and 75%. For barrier optimization due to sputter process changes and for comparison between processes this modest annealing was fully sufficient. However, higher TMR values will very likely be needed for applications. It is well known that higher annealing temperatures lead to a higher crystallinity of the barrier as well as the electrode material. Especially the CoFeB layers are known to crystallize only at elevated temperatures [57, 67]. Therefore annealing experiments were performed with a number of different stacks.

Firstly, fullfilm wafers were processed following the standard process flow containing the 265°C annealing step. After the structuring process the wafers were tested and diced into quadrants afterwards. These quadrants were then annealed separately at higher temperatures in the *Blue M* oven and tested again. The second annealing was always 20 min long (hold time at high temperature), the temperatures chosen were 300°C, 350°C, 450°C and 500°C. By this procedure all TMR junctions were only annealed twice: Firstly at 265°C and secondly at one higher temperature. Annealing one and the same sample again and again at ever increasing temperatures was not done.

As can be seen in figure 5.8 the measured TMR values increase strongly with increasing annealing temperature, reaching a maximum value of approximately 140 % after a 500°C annealing. Surprisingly there is no turning point in this graph after which the TMR drops again. It was expected that diffusion processes, especially Mn diffusion from the IrMn antiferromagnetic layer [68] or B diffusion from the electrode into the barrier [69], would lead to intermixing of layers which in turn would reduce the TMR . However, this was not observed for the tested temperatures. Annealing at even higher temperatures was not possible as the *Blue M* oven's maximum operating temperatures is 500°C only.

Despite the high TMR values after e.g. 500°C annealing this step was not used for standard wafers afterwards. The reason is that although TMR was increasing, the magnetic stability of the stack was greatly reduced, even after 350°C annealing only. An example of typical transfer curves after different annealing temperatures is shown in figure 5.9. The stable antiparallel plateau, which reaches from zero to approximately -600 Oe after 265°C annealing, is slowly being tilted. After 450°C there is no stable antiparallel state anymore. Additionally the hysteresis increased with increasing annealing temperature. This lack of magnetic stability may be caused by Mn diffusion into the CoFe layer which forms the lower part of the synthetic antiferrimagnet. However, for applications magnetic stability is crucial. Therefore further optimization is necessary to make the junctions either more robust at elevated temperatures or alternatively to achieve better crystallinity after annealing at moderate temperatures already. The crystallization process seems to depend on the thickness of the CoFeB electrode and the barrier according to Lee *et al.* [70]. Optimizing this ratio could help the crystallization to start at

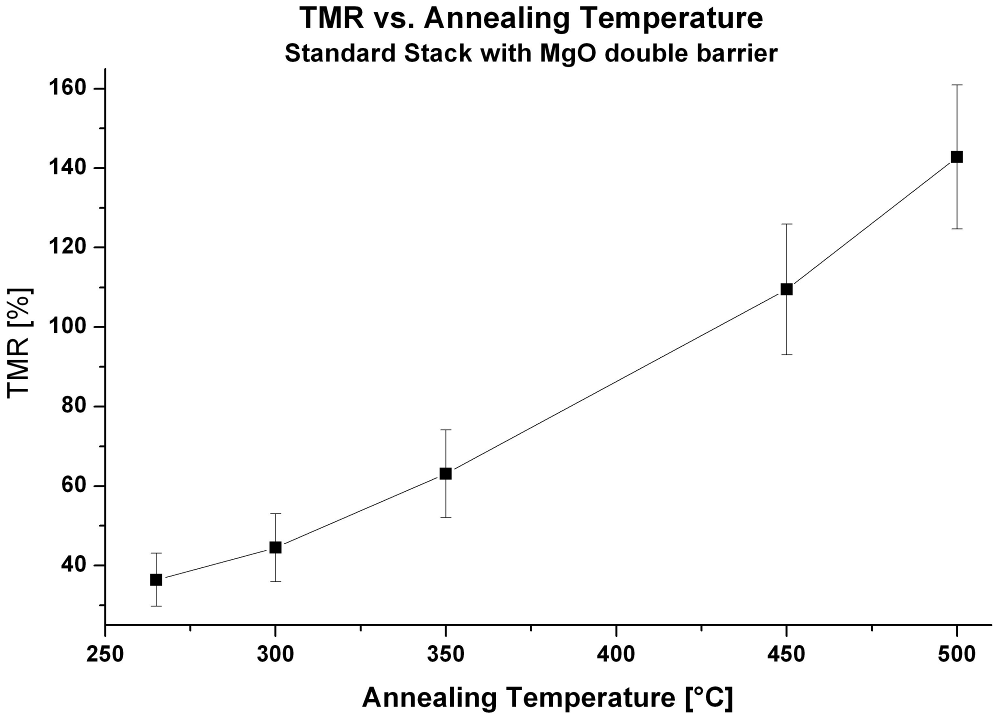

Figure 5.8: Average TMR values for CoFeB-MgO-CoFeB stacks after annealing at different temperatures. The TMR increases steadily with increasing temperature without reaching a turning point. All data points are average values of about 80 junctions; junctions that were short-circuited were excluded. All measurements were done at room temperature.

lower temperatures.

This topic however was not further evaluated in this thesis; it will be part of a follow-up project at Sensitec, where the optimization of magnetic properties to meet application needs is a major focus [9].

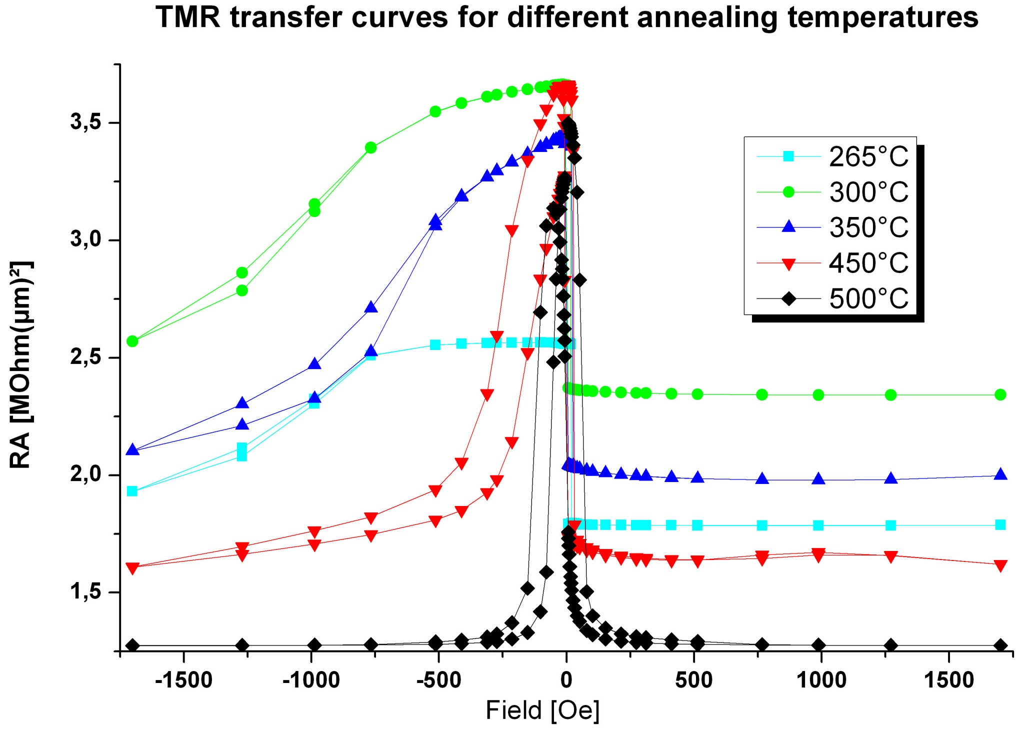

Figure 5.9: TMR measurement for a CoFeB-MgO-CoFeB stack after annealing at different temperatures. The TMR increases steadily with increasing temperature; however the exchange bias drops dramatically. Please note that the data shown was measured at different junctions of the same wafer.

# Chapter 6

# MgO Process Stability

The ultimate goal of the Sensitec TMR project, into which this thesis is incorporated, is to be able to produce TMR stacks of constantly high quality in a production environment. This requirement differs from the purely scientific goal of producing one or only a few highly optimized samples. In addition to high quality a high yield and reproducibility are needed. This requires a very stable process; the difficulties one encounters with this requirement will be discussed in this chapter.

## 6.1 Homogeneity over one Wafer

In university research substrates are normally not bigger than $10\text{mm}^2$ or 2 inch in diameter. For a volume production significantly larger substrates are used; in the case of Sensitec they have a diameter of five inch (125 mm). Typically a chip yield, i.e. the share of good chips per wafer, of 90 % or even more is needed in order to be profitable. At this experimental stage of TMR development a high yield is not crucial, however getting a first impression of the uniformity on a wafer is helpful to evaluate the deposition and structuring process.

Therefore whole wafers were sputtered and structured at the beginning of this project. Typically only very few junctions, less than 5 %, are short-circuited. Histograms of TMR and RA distributions for a standard stack wafer reveal a relatively narrow distribution of the TMR values (see figure 6.1). Only three junctions with a TMR of less than 15 % stick out. These MTJs are the only ones with an RA of less than 0.1 $\text{M}\Omega(\mu\text{m})^2$; this can be seen in figure 6.2. The distribution of the chip-average values of TMR and RA on the wafer is shown in

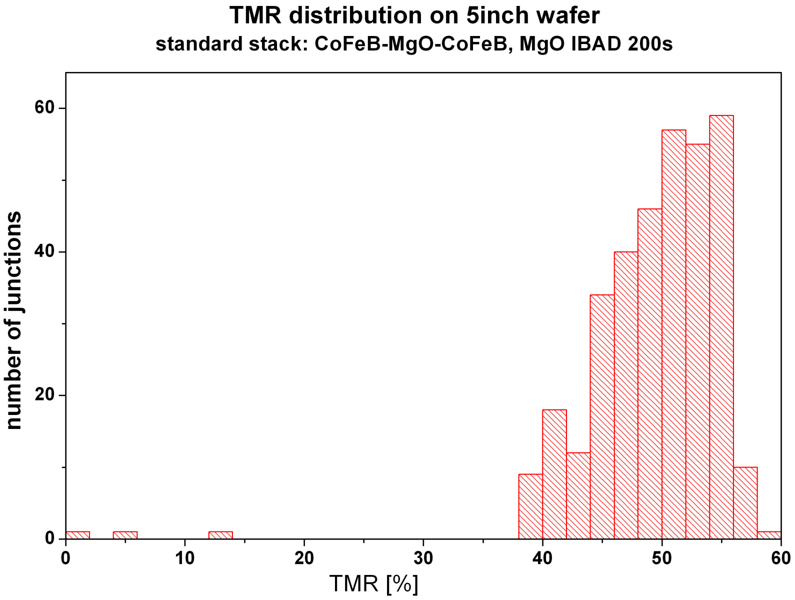

Figure 6.1: Measured TMR for a standard stack wafer, annealed at 265°C. All junctions were measured and included in the graph.

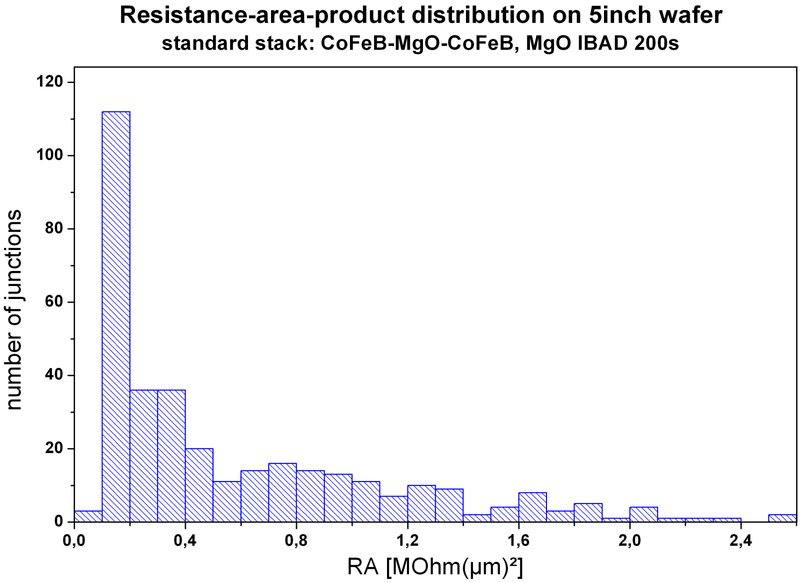

Figure 6.2: Measured resistance area product for a standard stack wafer, annealed at 265°C. All junctions were measured and included in the graph.

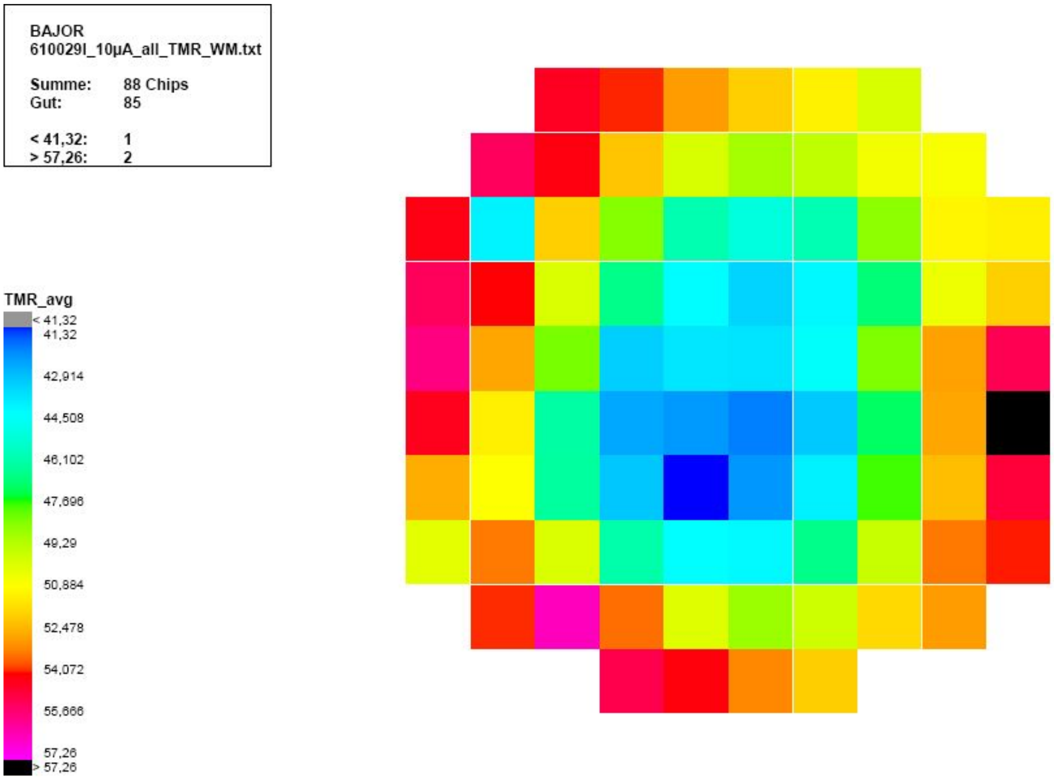

Figure 6.3: TMR distribution for a standard stack wafer annealed at 265°C. TMR is averaged over all working junctions for each chip.

figures 6.3 and 6.4 respectively.

As expected for an ion beam process the distribution is mainly radial. Especially the resistance shows a strong radial dependence with an outward increasing resistance.

Here average values per chips are plotted; the junctions that are short-circuited are disregarded. Only one row of junctions (four junctions) is measured per chip to save time. The two rows which contain identical junctions are only a few hundred microns apart and will therefore give very similar results. This was proven once for a standard stack wafer containing CoFeB electrodes and a 2nm MgO barrier, see figure 6.5; after that only one row per chip was tested.

Because of the good homogeneity of the TMR stacks so-called ”quadrant wafers” were often sputtered (see chapter 4.6), as it could be expected that each quadrant would give the same results.

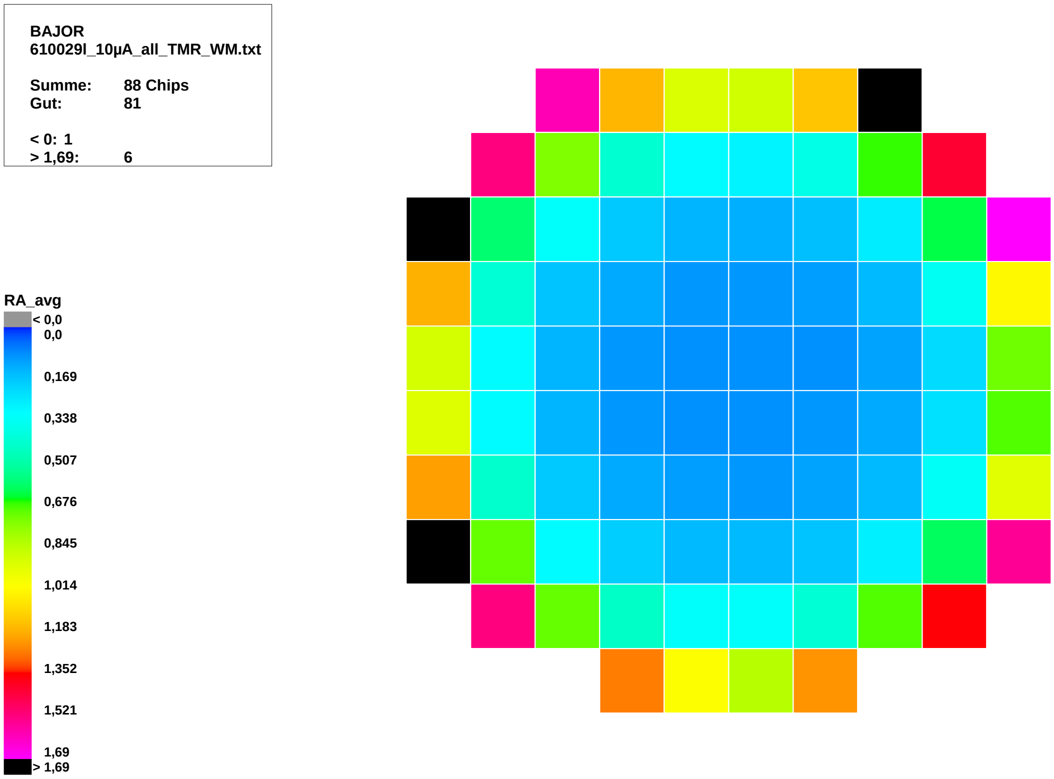

Figure 6.4: Resistance area product in M$\Omega\mu$m$^2$ for a standard stack wafer annealed at 265°C. The values are averaged over all working MTJs per chip.

## 6.2 Reproducibility of TMR Standard Stacks

Normally a monitoring of sputtering rates and electric or magnetic properties of the metallic films is performed on a regular basis. This procedure however is insufficient for MgO; the only significant parameter that can be used to monitor the MgO process is the measurement of TMR. In order to test the MgO process stability so-called TMR standard stacks were sputtered whenever any TMR wafers were produced. These wafers were always annealed, structured and measured in the same way.

The standard stack is built up as follows: Si // 400nm $Al_2O_3$ / Ta 5nm / Ru 10nm / Ta 5nm / IrMn 15nm / CoFe 3nm / Ru 0.8nm / CoFeB 4nm / MgO IBAD 200s / CoFeB 3nm / Ru 5nm. The barrier process that is used is the simplest ion beam assisted process without oxygen; the sputtering time of 200s is meant to result in a 2nm thick MgO barrier. The resulting TMR and resistance-area product values are plotted in figure 6.6. As one can clearly see

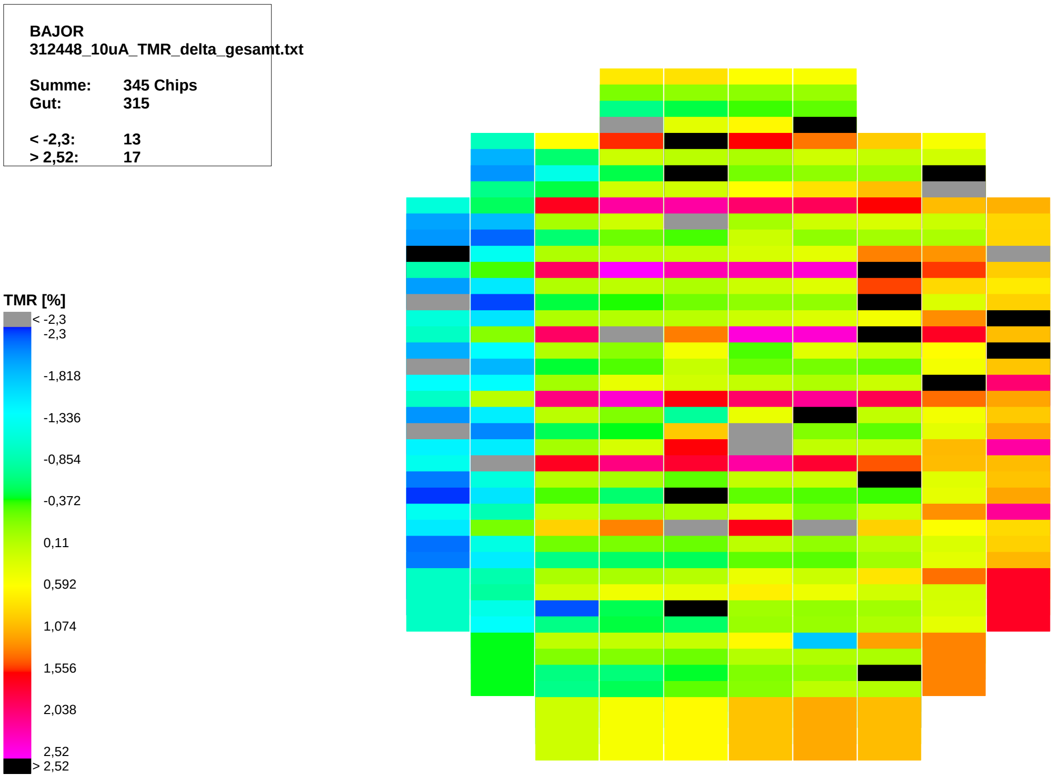

Figure 6.5: Difference in TMR between left and right column of junctions of the same chip. The wafer contained CoFeB electrodes and a 2nm MgO barrier; annealing was done at 265°C. The absolute TMR ratios ranged from 10 % at the edge up to 55 % at the center. For most junctions the difference between left and right column is less than 0.5 %.

the wafers do not always give the same results, although they were produced in the same way. The two data points that are marked with a red ellipse are most striking. The TMR ratio is considerably lower than for all other wafers and the resistance is greatly increased at the same time. A close look at the sputtering sequences reveals the main difference between the marked wafers and the others: $Co_2MnSi$ had been sputtered directly before these TMR standard stack wafers. The influence of previously sputtered samples is also apparent in the sample that is marked with a green ellipse. This wafer is a quadrant wafer with identical quadrants, but different processes, i.e. dummy wafers, in between the TMR quadrants. The left data point represents the average TMR and RA value for the whole wafer, the right point represents data from the same wafer, but with the

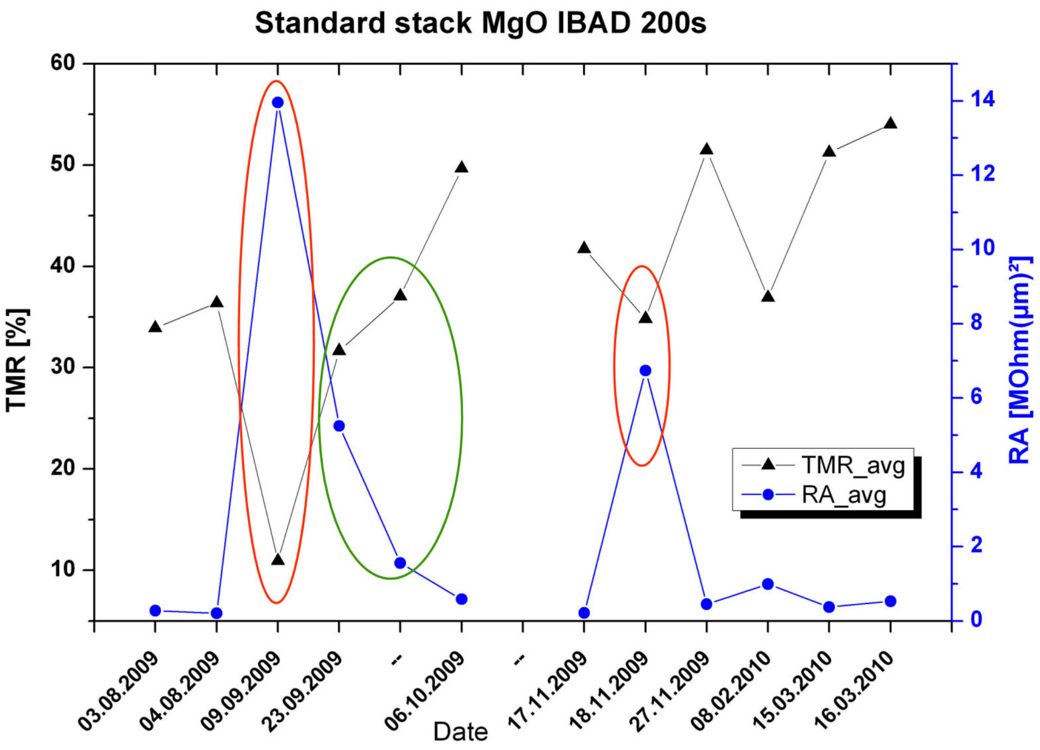

Figure 6.6: TMR and resistance-area-product for CoFeB-MgO-CoFeB stacks with 200s MgO IBAD. All values are average values for whole wafers with approximately 100 chips.

second quadrant being disregarded: Before the sputtering of the second quadrant a $Co_2MnSi$ dummy wafer had been deposited, leading to an increase in resistance and a drop of TMR. If all marked data points are ignored, average TMR ranges from approximately 35 % to 55 %, the resistance area product varies between 200 k$\Omega(\mu m)^2$ and 1 M$\Omega(\mu m)^2$. These results show a that the TMR process as a whole is a stable process, considering that no measures have been taken to regulate the MgO process and structuring can have an influence on the TMR results as well.

The discovery of the dramatic influence of the "sputtering history" of the IBD chamber on the result of the actual wafer shows how sensitive and fragile the barrier deposition process is. In a standard stack the MgO barrier is the only layer that is deposited in the IBD chamber, seed and electrodes are all deposited in PM 4. In this case it is possible to define a chamber conditioning process that always has to be run before the deposition of TMR wafers (e.g. a well-defined number of dummy wafers which are being sputtered with MgO). In the case of TMR wafers with a $Co_2MnSi$ Heusler electrode the problem is harder to circumvent. The whole stack, seed, bottom electrode, barrier and top electrode, are deposited in the ion beam chamber. This means that the MgO process will always take place immediately after the deposition of a rather thick CMS layer. Chamber conditioning with the help of dummy wafers is obviously impossible, so a chamber conditioning has to be integrated into the MgO process itself. Ideas to stabilize the MgO process will be discussed in the following subchapter.

## 6.3 MgO Process Stability after $Co_2MnSi$ Deposition

In order to investigate the process stability CoFeB standard stack wafers were sputtered and analyzed. Right before each wafer a dummy wafer with a thick CMS layer was deposited in the IBD chamber to simulate the deposition of a bottom electrode and to "poison" the chamber. The MgO barrier itself was sputtered with a slightly modified recipe each time. The goal was to find an adjusted barrier deposition process that yielded the same TMR and RA values for a standard stack independent of the previous processes in the IBD chamber.

To verify the negative influence of $Co_2MnSi$ sputtering on TMR and RA and to check whether other metals in the IBD lead to the same results, dummy wafers with Cr, CoFe and CMS of different thicknesses were sputtered right before an MgO barrier. The results are plotted in figure 6.7.

According to this analysis CoFe deposition does not have any influence on the MgO barrier process; Cr deposition leads to an increase of RA, independent of the thickness that is deposited. For $Co_2MnSi$ however the influence is dramatic: After the deposition of 50nm CMS TMR drops to just above 20 %, the resistance area product jumps to more than 20 $M\Omega(\mu m)^2$ for a nominal MgO thickness of 2.0 nm. Therefore dummy wafers with 50nm CMS, which corresponds to a deposition time of about 600s, were sputtered right before the TMR test wafers.

As the mechanism behind this effect remained completely unclear, a number of different approaches to reverse the negative effect of CMS deposition were considered and subsequently evaluated experimentally:

1. Changing the MgO deposition time.

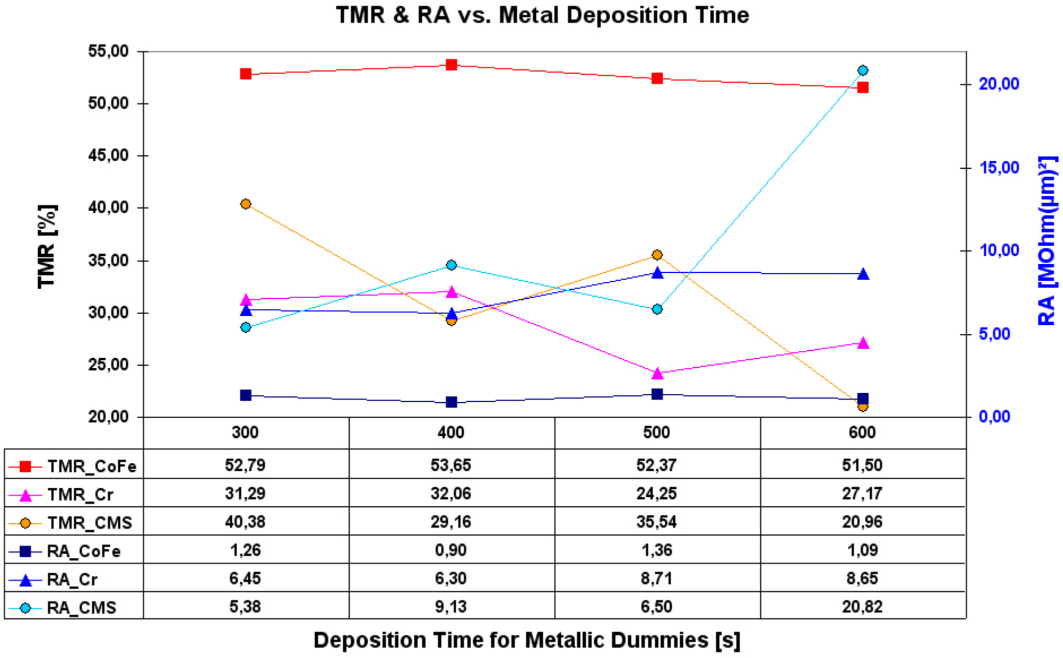

| | 300 | 400 | 500 | 600 |
|---|---|---|---|---|
| TMR_CoFe | 52,79 | 53,65 | 52,37 | 51,50 |
| TMR_Cr | 31,29 | 32,06 | 24,25 | 27,17 |
| TMR_CMS | 40,38 | 29,16 | 35,54 | 20,96 |
| RA_CoFe | 1,26 | 0,90 | 1,36 | 1,09 |
| RA_Cr | 6,45 | 6,30 | 8,71 | 8,65 |
| RA_CMS | 5,38 | 9,13 | 6,50 | 20,82 |

Figure 6.7: TMR and resistance-area-product for CoFeB-MgO-CoFeB stacks with 200s MgO IBAD. Dummy wafers with different metallic layers had been deposited before.

2. Cleaning the etch gun from possible metallic contamination that was taken up during the CMS process.
3. Implementing a longer target preclean before the MgO deposition.
4. Oxidizing the chamber walls.

The first point is maybe the most obvious: If the resistance is too high, the barrier might be too thick, so the deposition rate might be increased with respect to the normal rate. So reducing the sputtering time until the old resistance value is reached again could be a simple work around. The second idea of cleaning the etch gun is based on a similar assumption: If the etch gun, which is directed onto the substrate, is covered with metal, the etch rate might drop which in turn leads to a higher net deposition rate. This could explain a higher resistance. The third point is based on the assumption that during the deposition of $Co_2MnSi$, which is situated right next to the MgO target, either the MgO target or the chamber or both are covered with a metallic film. If the target is contaminated the barrier will contain alien atoms that will surely influence its performance. If the chamber is contaminated or ”too metallic” the fragile electric potentials might change which in turn could influence the process parameters. Oxidizing the chamber walls (point 4) leads into the same direction.

### 6.3.1 Adjusting the MgO Deposition Time

In order to find out whether the MgO deposition rate is being changed by the previous metal deposition two quadrants wafers with different MgO deposition times were deposited. The first wafer was deposited with CoFe dummy wafers in between the quadrants, the second with $Co_2$MnSi dummy wafers. The deposition time was reduced from the standard value of 200s down to 140s, which would correspond to a drastic change of 30 % in deposition rate. The resulting TMR and RA values are summarized in figure 6.8.

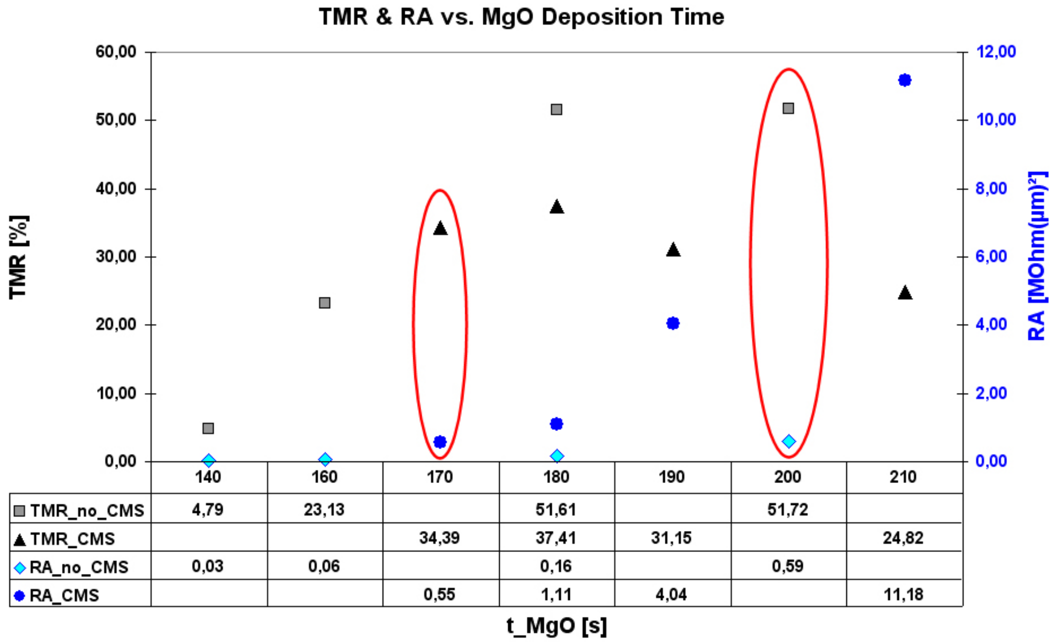

| | 140 | 160 | 170 | 180 | 190 | 200 | 210 |
|---|---|---|---|---|---|---|---|
| ■ TMR_no_CMS | 4,79 | 23,13 | | 51,61 | | 51,72 | |
| ▲ TMR_CMS | | | 34,39 | 37,41 | 31,15 | | 24,82 |
| ◇ RA_no_CMS | 0,03 | 0,06 | | 0,16 | | 0,59 | |
| ● RA_CMS | | | 0,55 | 1,11 | 4,04 | | 11,18 |

Figure 6.8: TMR and resistance-area-product for CoFeB-MgO-CoFeB stacks with different sputtering times for the MgO barrier. Stacks with and without prior CMS deposition were sputtered and compared.

One can see that the resistance value for the standard process of 200s, which is approximately 500 k$\Omega$($\mu$m)$^2$, is reached at a deposition time of only 170s.

This looks like reduction of the deposition rate by 15 %, whose origin remains completely unclear. However, the TMR value is almost halved as compared to the 200s wafer. Therefore work on finding the reason for this apparent change of the deposition rate, or finding a process that reverses this effect, had to continue.

The change of deposition rate, or the change of the MgO barrier thickness to be precise, was also verified by X-Ray Reflectometry measurements. Stacks with identical thicknesses were deposited: The first one had CoFeB electrodes, the second one $Co_2MnSi$ electrodes. The barrier deposition process was the same in both cases. The XRR data and corresponding fit can be seen in figure 6.9. If the layers had identical thicknesses, the plots would be almost congruent with each other. This is obviously not the case; the exact fit results are summarized in table 6.1.

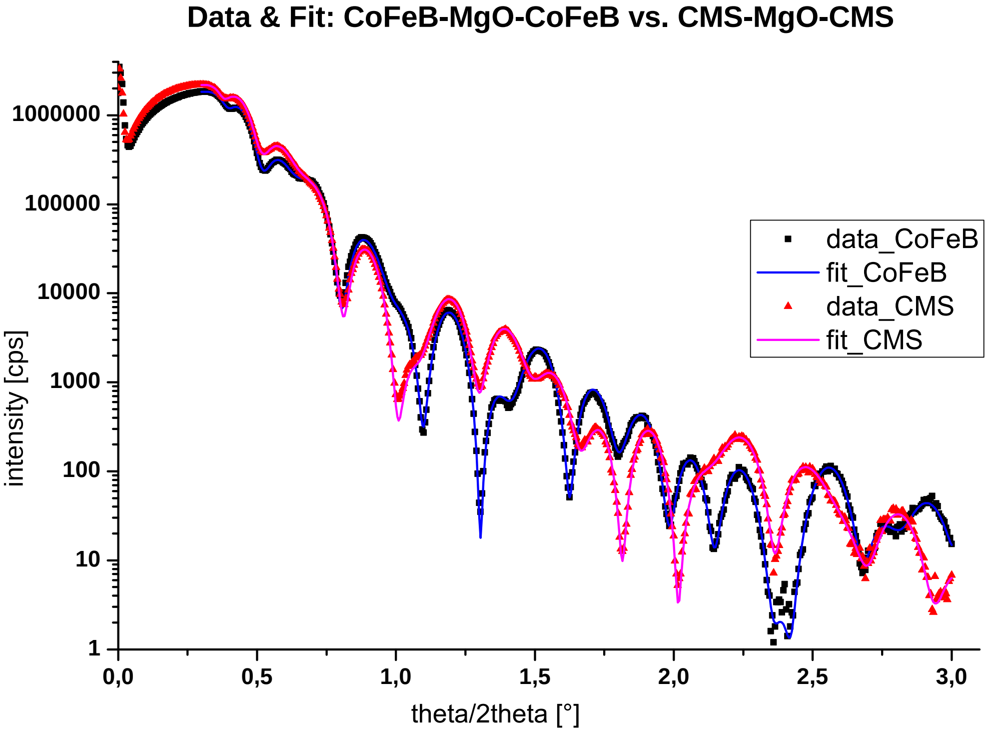

Figure 6.9: XRR Data and corresponding fit for a CoFeB-MgO-CoFeB stack (black/blue) and for a stack with identical nominal layer thicknesses containing CMS-MgO-CMS (red/pink).

From this data the same barrier process applied after a $Co_2MnSi$ deposition process yields in an MgO barrier that is 4 Å thicker than in the case of CoFeB.

| **Layer** | **nominal thckn. [Å]** | **Mat. 1** | **real thckn. [Å]** | **Roughn. [Å]** | **Mat. 2** | **real thckn. [Å]** | **Roughn. [Å]** |
|---|---|---|---|---|---|---|---|
| Sub | inf | Si | inf. | 3.17 | Si | inf. | 4.00 |
| 1 | 100 | CoFeB | 95.33 | 2.73 | CMS | 85.24 | 1.00 |
| 2 | 18 | MgO | 23.13 | 2.54 | MgO | 27.56 | 2.60 |
| 3 | 100 | CoFeB | 94.18 | 4.29 | CMS | 85.62 | 4.68 |
| 4 | 50 | Ru | 39.02 | 4.58 | Ru | 47.88 | 3.97 |
| 5 | 0 | CHx | 10.49 | 5.77 | CHx | 9.46 | 2.84 |

Table 6.1: Fit of XRR data for a CoFeB-MgO-CoFeB stack on Si/SiOx as well as the stack $Co_2$MnSi-MgO-$Co_2$MnSi. For the Si/SiOx substrate only the roughness was included into the fitting parameters. The goodness of the fits was 0.033 and 0.03 respectively.

This result supports the theory that the chamber is negatively preconditioned by the deposition of the $Co_2$MnSi; the reason why and how to circumvent this problem remains unclear at this point.

### 6.3.2 Etch Gun Cleaning

The idea behind the etch gun cleaning process was to remove metallic residue at the etch gun by igniting the etch gun alone at the beginning of the MgO process. This step takes place with all shutters closed, thereby avoiding redeposition onto the wafer surface. Afterwards the standard recipe was used to deposit the MgO barrier.

As shown in figure 6.10 no improvement was found for the etch clean process. A contamination of the etch gun during the CMS deposition process can therefore be excluded.

### 6.3.3 Target Preclean Variation

Normally a sputtering recipe contains four steps: A pre-start, where the gas is set, the target is chosen etc., a start-step, where the guns are ignited, a target preclean of about 30 s and the actual deposition step. For the deposition of MgO the target preclean had already been increased to 90 s in order to further stabilize both, the deposition and especially the etch gun. An additional stabilization was achieved by igniting the guns independently, the preclean was performed twice

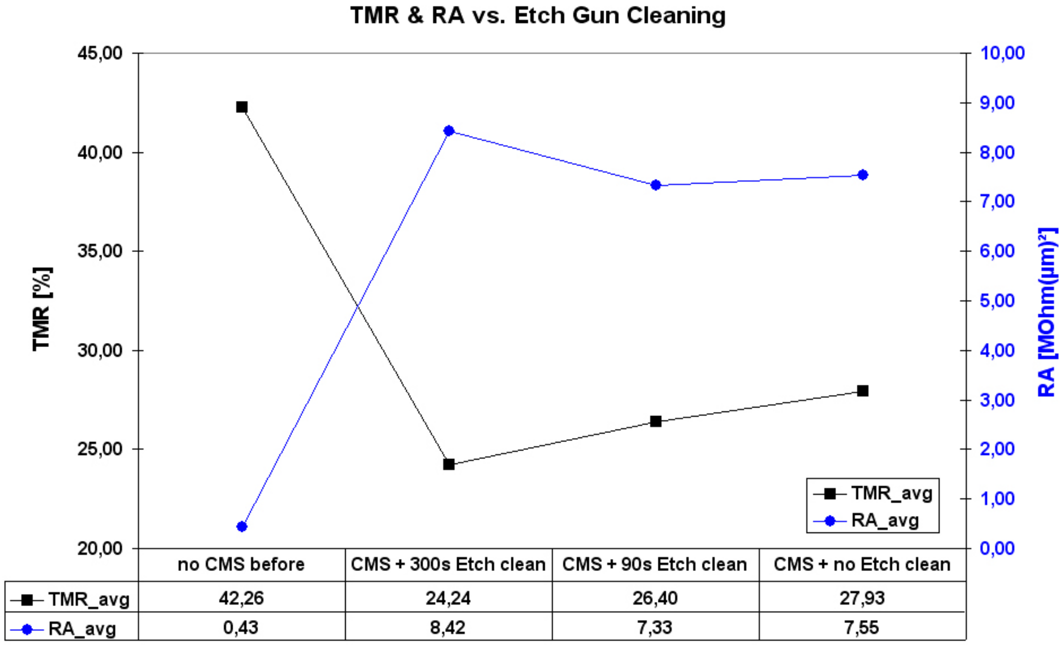

| | no CMS before | CMS + 300s Etch clean | CMS + 90s Etch clean | CMS + no Etch clean |
|---|---|---|---|---|
| TMR_avg | 42,26 | 24,24 | 26,40 | 27,93 |
| RA_avg | 0,43 | 8,42 | 7,33 | 7,55 |

Figure 6.10: TMR and resistance-area-product for CoFeB-MgO-CoFeB stacks with 200s MgO IBAD. Before the barrier deposition an etch gun cleaning step of 90s or 300s was performed for two of the four quadrants.

from then on. If the assumption of a target and/or chamber contamination was correct, even a preclean of 180 s would then not have been sufficient.

In an experiment matrix the preclean was varied between 30 s per step up to 135 s per step. As can be seen in figure 6.11 a prolonged target preclean has a positive effect: The longer the preclean time, the higher the measured TMR and the lower the measured resistance area product. However, even after a target preclean of 120 s, when about the same TMR is reached, the resistance is still considerably higher than the resistance without Heusler sputtering before. Even after six minutes of target preclean the resistance area product is still five times as high as the resistance of the reference wafer from the same sputtering run.

This result leads to the conclusion that the MgO target is not being contaminated during the $Co_2MnSi$ process but the chamber is negatively preconditioned. Although the target preclean is mainly meant to remove contamination from the target, the sputtered materials covers the chamber walls and the stage shutter afterwards. However, this oxide layer seems to be insufficient to reverse the ad-

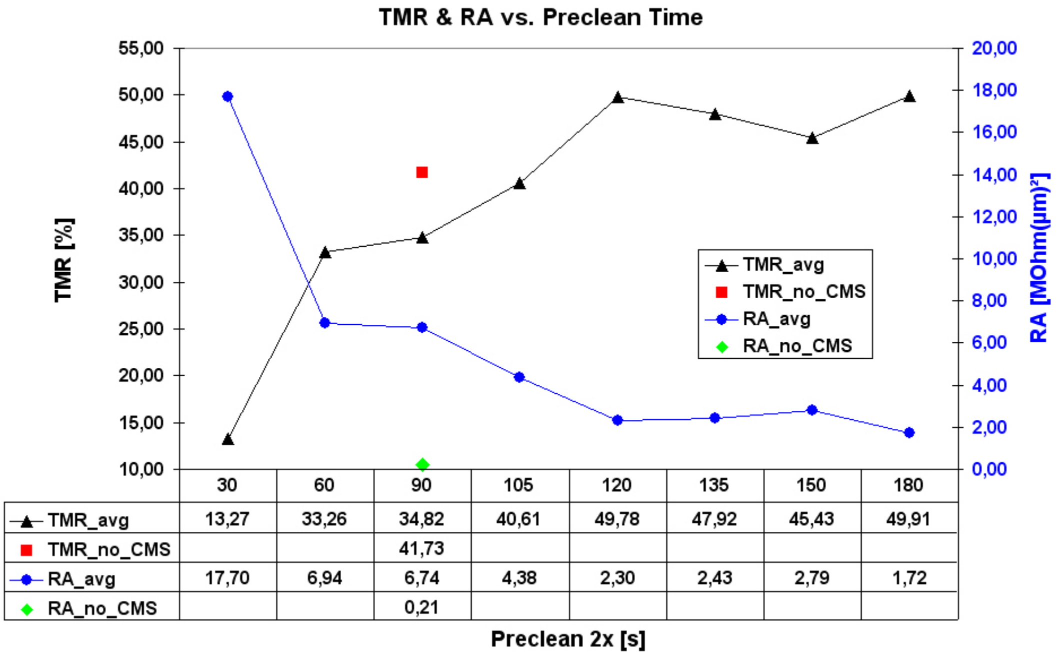

| | 30 | 60 | 90 | 105 | 120 | 135 | 150 | 180 |
|---|---|---|---|---|---|---|---|---|
| TMR_avg | 13,27 | 33,26 | 34,82 | 40,61 | 49,78 | 47,92 | 45,43 | 49,91 |
| TMR_no_CMS | | | 41,73 | | | | | |
| RA_avg | 17,70 | 6,94 | 6,74 | 4,38 | 2,30 | 2,43 | 2,79 | 1,72 |
| RA_no_CMS | | | 0,21 | | | | | |

Figure 6.11: TMR and resistance-area-product for CoFeB-MgO-CoFeB stacks with 200s MgO IBAD. The target preclean before the MgO deposition was varied as shown in the table. The result of a standard wafer of the same run without a CMS dummy before has been added as a reference.

verse effect of CMS sputtering. Therefore a deliberate oxidation of the chamber interior was tested.

### 6.3.4 Oxidation of the Sputtering Chamber Walls

An oxidation of the sputtering chamber always bears the risk of oxidizing the wafer as well. In the case of CMS it was shown by first-principles calculations that the oxidation of both electrodes significantly reduces the conductance especially in the parallel configuration, which then in turn reduces the TMR ratio [37]. For that reason the oxidation of the wafer surface has to be avoided. To realize an oxidation of the sputtering chamber without the risk of oxidizing the half-sputtered wafer a three-step barrier deposition was performed. Firstly a thin layer of MgO was deposited to protect the bottom electrode against oxidation. Secondly the target shutter as well as the stage shutter were closed and a small amount of argon/oxygen was let into the chamber for a well defined time. Afterwards the tunneling barrier deposition was finished. In this experiment the total deposition time was fixed to 180s. Different parameters can be varied to optimize the oxidation process: The deposition time ratio before and after the chamber oxidation and the oxidation process itself (duration and gas flow).

In the first experiment the ratio between the first and the second MgO deposition step was kept constant, but the Ar/$O_2$ gas flow and the flooding time were varied. A gas flow of either 0.5 sccm or 1.0 sccm was chosen, which corresponds to the gas flows used when depositing MgO in an Ar/$O_2$ atmosphere. The selected times were 30s, 60s and 120s. The resulting TMR and RA values are plotted in figure 6.12. The lighter graphs belong to samples where no $Co_2MnSi$ has been sputtered before, the darker ones to a samples where dummy-wafers with 50 nm of $Co_2MnSi$ have been sputtered directly before the barrier deposition.

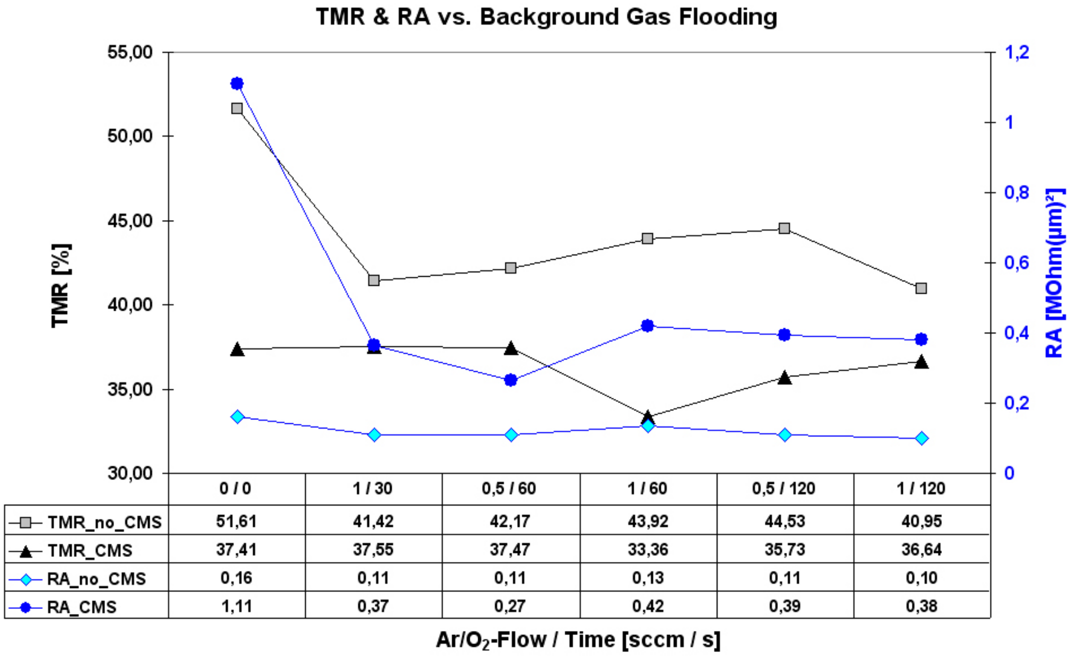

| | 0 / 0 | 1 / 30 | 0,5 / 60 | 1 / 60 | 0,5 / 120 | 1 / 120 |
|---|---|---|---|---|---|---|
| —□— TMR_no_CMS | 51,61 | 41,42 | 42,17 | 43,92 | 44,53 | 40,95 |
| —▲— TMR_CMS | 37,41 | 37,55 | 37,47 | 33,36 | 35,73 | 36,64 |
| —◇— RA_no_CMS | 0,16 | 0,11 | 0,11 | 0,13 | 0,11 | 0,10 |
| —●— RA_CMS | 1,11 | 0,37 | 0,27 | 0,42 | 0,39 | 0,38 |

Figure 6.12: TMR and resistance-area-product for CoFeB-MgO-CoFeB stacks with 40s + 140s MgO IBAD. In between the two MgO steps the chamber was flooded with Ar/$O_2$ of a set flow for a well-defined time.

The graph does not show a clear connection between the chamber flooding parameters and the wafer results; TMR and RA seem to be independent from gas flow and time. Surprisingly one can see that although there is still a difference

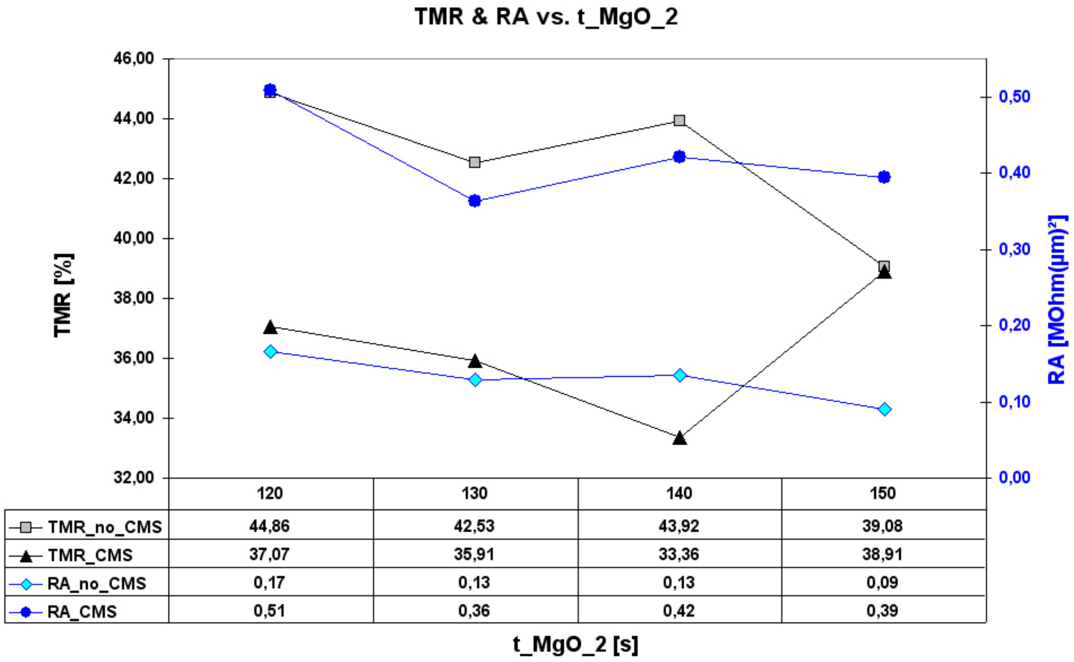

| | 120 | 130 | 140 | 150 |
|---|---|---|---|---|
| TMR_no_CMS | 44,86 | 42,53 | 43,92 | 39,08 |
| TMR_CMS | 37,07 | 35,91 | 33,36 | 38,91 |
| RA_no_CMS | 0,17 | 0,13 | 0,13 | 0,09 |
| RA_CMS | 0,51 | 0,36 | 0,42 | 0,39 |

Figure 6.13: TMR and RA for different deposition time ratios; here the second deposition time was chosen as scale. The total deposition time was fixed to 180s, the oxygen flooding to 1.0 sccm for 60s.

between samples with and without CMS-dummies before, the difference is smaller than in previous experiments. Especially the resistance-area product is only about twice as high for the samples with CMS than for the samples without it[1]. In general this process of oxygen flooding seems to work fine, at least with the standard stack the normal results could be reproduced.

A last experiment was done to find out the optimum ratio between the first MgO deposition before the oxygen flooding and the second deposition afterwards. The total deposition time was 180s again, a medium oxidation with 1.0 sccm Ar/$O_2$ for 60s was chosen. The resulting TMR ratios and resistance-area products are plotted in figure 6.13.

Again there is no clear trend of dependence on the second deposition time: Within the limits of process fluctuations TMR as well as the resistance area product are independent of the deposition time ratio.

---

[1] A reference sample "after CMS-dummy" with 180s of MgO was sputtered with the next matrix; it resulted in an average TMR of 37.41 % and a resistance-area-product of 1.11 $M\Omega\mu m^2$.

These results on barrier process stability suggest that the sputtering chamber needs to be oxidized before the MgO barrier is being deposited. Because of that a three step barrier process was chosen for future experiments with MTJs containing $Co_2MnSi$ electrodes: At first a thin MgO layer was deposited without additional oxygen, secondly the chamber was oxidized for 120s with 0.5 sccm $Ar/O_2$ and finally the second part of the MgO barrier was deposited non-reactively. A sequence like this had proven to produce constant TMR and RA values for MTJs with CoFeB electrodes independent of the ”sputtering history” of the chamber.

# Chapter 7

# $Co_2MnSi$ Thin Films

In the following chapter the work on $Co_2MnSi$ Heusler thin films will be presented. $Co_2MnSi$ has been successfully integrated into MTJs with both, $Al_2O_3$ and MgO barriers by various research groups worldwide [42, 71–73]. Apart from that $Co_2MnSi$ has a very high Curie temperature of 985 K, which is important for room temperature applications [22, 74]. Therefore this special Heusler alloy was chosen in order to test the industrial usage of Heusler electrodes.

There are different possibilities to deposit alloys with a special stoichiometry, like co-sputtering from different pure targets or sputtering from a stoichiometric target. Due to the sputtering system that was used ablating from a single target was the only option. Because of the experience in the "Thin films and physics of nanostructures" group at the University of Bielefeld an off-stoichiometric $Co_2MnSi$ target with 43.6 % Co, 28.0 % Mn and 28.4 % Si was used[1]. The composition of the target was verified by EDX analysis (see Appendix C); however the composition of the films deposited could not be checked because the software is not designed for the analysis of thin films. It was further decided to place the target in the IBD chamber for various reasons:

1. The IBD chamber has the best vacuum in the whole system, which guarantees uncontaminated films.

2. The MgO target is located in the same chamber, as well as a CoFe target, which can be used as a counter-electrode. This target configuration provides the possibility to deposit the whole MTJ stack in one chamber without having to transfer the wafer.

---

[1] An almost identical composition was used by Oogane *et al.* for the preparation of MTJs with CMS electrode and alumina barrier [75]

3. To my knowledge, IBD deposition of Heusler alloys has never been tested before. However, especially the IBAD process, which is used for the MgO deposition, could be advantageous for the crystalline growth of Heusler thin films. The additional energy that is brought into the film could help atom rearrangement and is expected to have a similar effect as deposition at elevated substrate temperatures.

At first, various thin film systems were sputtered on small glass or oxide-covered Si substrates to find an ideal seed layer. The samples were analyzed by X-Ray diffraction and room temperature VSM measurements. Afterwards the optimized Co$_2$MnSi films were integrated into magnetic tunneling junctions with an MgO barrier.

## 7.1 X-Ray Diffraction Analysis

All samples were analyzed using a *PANalytical X'Pert MRD* diffractometer with a PW3373/00 Cu LFF DK292712 X-Ray tube; the wavelength of the Cu K$_\alpha$ radiation is 1.54056 Å. The diffractometer is equipped with a four-circle goniometer, that allows in-plane scans as well. The set-up of the scans and data collection were done with the commercial software *X'Pert Data Collector*.

The optimum crystalline orientation for Heusler thin films is (100) orientation [25]; however, depending on the substrate and / or seed layer different orientations are possible. For a quick overview concerning orientation and ordering (220) and (200) reflexes were looked at first. If a sample was promising, the (111) reflex indicating perfect L2$_1$ ordering was analyzed. In a cubic crystal the angle between the different diffraction planes $(h_1k_1l_1)$ and $(h_2k_2l_2)$ is given by [76]:

$$\cos\psi = \frac{h_1h_2 + k_1k_2 + l_1l_2}{\sqrt{(h_1^2 + k_1^2 + l_1^2)(h_2^2 + k_2^2 + l_2^2)}} \tag{7.1}$$

In table 7.1 the angles between the first diffraction planes are listed.

### 7.1.1 Seed Layer Optimization

At first simple stacks of the type Seed/Co$_2$MnSi/Ta were deposited on glass substrates. The seed layer material as well as the CMS film thickness were varied. All typical seed materials that were present in the sputtering tool were tested. In

| $h_1k_1l_1$ | $h_2k_2l_2$ | $\psi$ [°] | $\psi$ [°] |
|---|---|---|---|
| 100 | 110 | 45.0 | |
| 100 | 111 | 54.74 | |
| 110 | 111 | 35.26 | 90.0 |

Table 7.1: Angles between the first diffraction planes in a cubic lattice (for $\psi \leq 90°$).

general $Co_2MnSi$ crystallizes in $L2_1$ ordering, in contrast to other Heusler materials, especially the ones containing Al like $Co_2MnAl$ or CCFA, that are preferably only B2-ordered [22, 77]. However, in order to achieve good crystallinity Heusler films have to be sputtered onto heated substrates [78], or have to be annealed after room temperature deposition [79]. As the PVD is not equipped with a heatable chuck, the samples were annealed *ex situ* at 300°C or 400°C and analyzed by X-Ray diffraction afterwards [2].

The following systems were deposited and analyzed (see table 7.2):

| **Sample** | **Seed 1** | **thckn. [nm]** | **Seed 2** | **thckn. [nm]** |
|---|---|---|---|---|
| A, B, C | Cr | 5 | | |
| D, E, F | NiFeCr | x | NiFe | y |
| G, H, I | MgO | 10 | | |
| J, K, L | MgO | 10 | Cr | 5 |
| M, N, O | Ta | 5 | | |
| P, Q, R | Ru | 5 | | |

Table 7.2: Seed layer matrix for $Co_2MnSi$ deposited on glass. The exact thicknesses of NiFeCr/NiFe are confidential.

For each seed layer samples with 10 nm, 20 nm and 50 nm $Co_2MnSi$ were deposited. Because of the amorphous glass substrate a dominant amorphous background was present in all samples. The signal to noise ratio is relatively low which complicates the data interpretation. However, only a qualitative analysis was needed in this case, for comparing the results for different seed layer the data

---

[2] The samples were also magnetically analyzed by room temperature VSM measurements, see 7.3. However, the results were not as obvious as the X-Ray results.

is significant enough. The (200) and (220) scans for various seed layers are shown in figure 7.1 and figure 7.2 respectively.

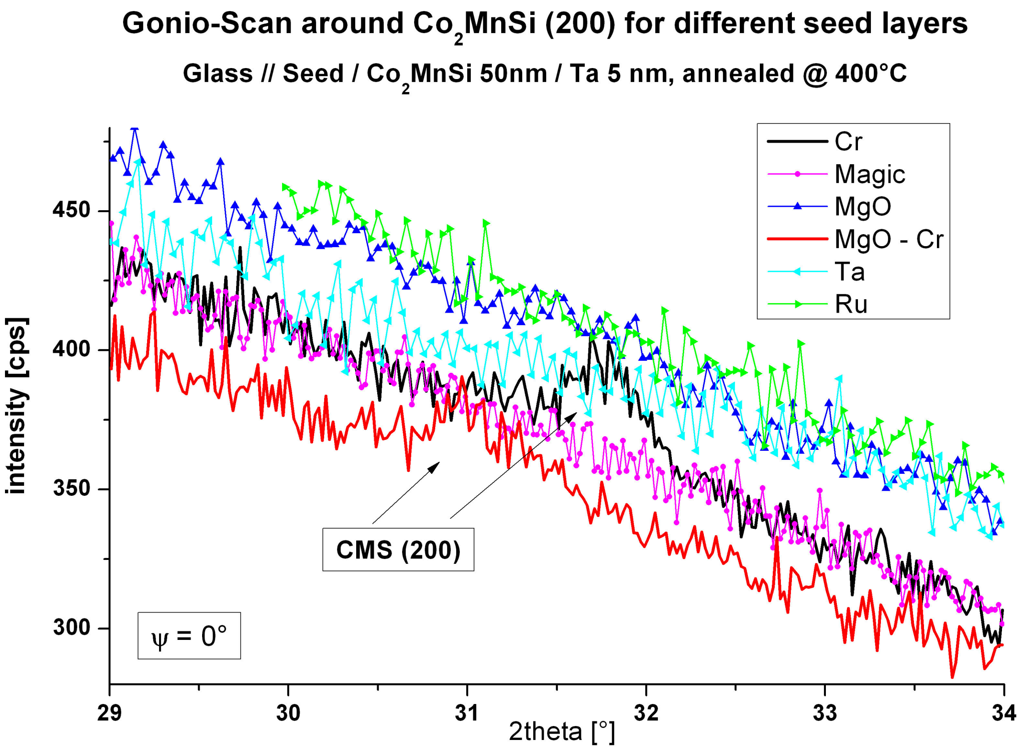

Figure 7.1: X-Ray diffraction pattern for the Gonio-Scan around the (200) reflex, $\psi = 0°$. Only for Cr and MgO/Cr seed a small peak is visible.

As expected from lattice constants the Cr seed layer is best suited for CMS. Only in the case of Cr, MgO/Cr and NiFeCr/NiFe seed layers characteristic reflexes were found. The samples annealed at 300 °C did not show any crystalline ordering, therefore only the 400°C annealed samples were further investigated. For all future experiments, unless stated otherwise, a 400°C annealing was used to crystallize the CMS layer.

In this first matrix the sample with 5nm of Cr showed a weak (200) peak under $\psi = 0°$; this indicates (100) orientation of the CMS film. Additionally, the (200) peak is characteristic for B2-ordering of the Heusler films and vanishes if the samples are completely disordered (A2). The existence of a small (200) reflex therefore indicates at least partly B2 order of the CMS film. An even weaker (200) reflex that was shifted by 0.8° to smaller angles was found for MgO/Cr seed.

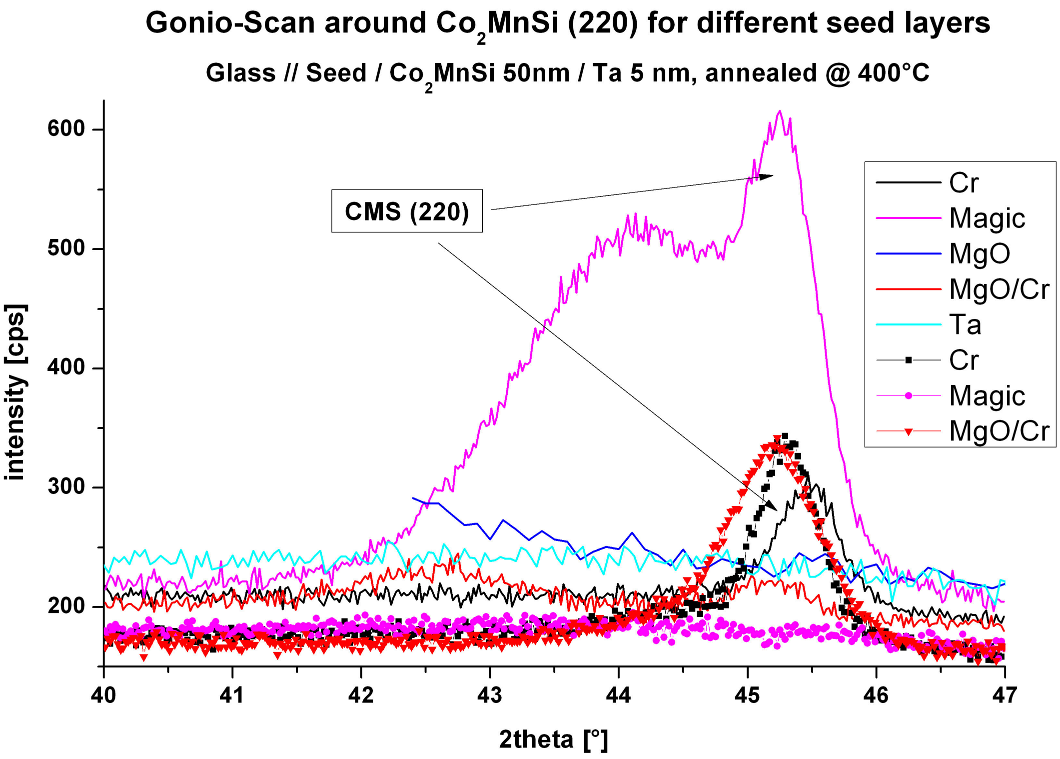

Figure 7.2: X-Ray diffraction pattern for the Gonio-Scan around the (220) reflex. Lines correspond to a tilt angle of $\psi = 0°$, Lines + symbols to $\psi = 45°$.

The peak shift signifies stress within the $Co_2MnSi$ film. The fundamental reflex (220) was found under both tilt angles $\psi$ that were tested, 0° and 45°. Therefore one can conclude that the CMS films are not perfectly (100) oriented but are polycrystalline with (110) components as well. In the case of NiFeCr/NiFe-seed the whole film was strongly (110) textured, the (220) reflex was found for $\psi = 0°$ only. However, no (200) reflex was present, the $Co_2MnSi$ grows completely disordered in the A2 state.

As mentioned above different thicknesses of $Co_2MnSi$ were tested in order to find a minimum value for crystallization. As an example the results for Cr-seed is presented in figure 7.3.

Here the (220) main reflex is visible only for the 20 nm and 50 nm CMS film; the (200) B2-ordering reflex however does only just appear for the 50nm film. 10 nm CMS was not enough to crystallize the film at all. The best results were obtained with the thickest 50 nm CMS film. Thicker layers were not tested for

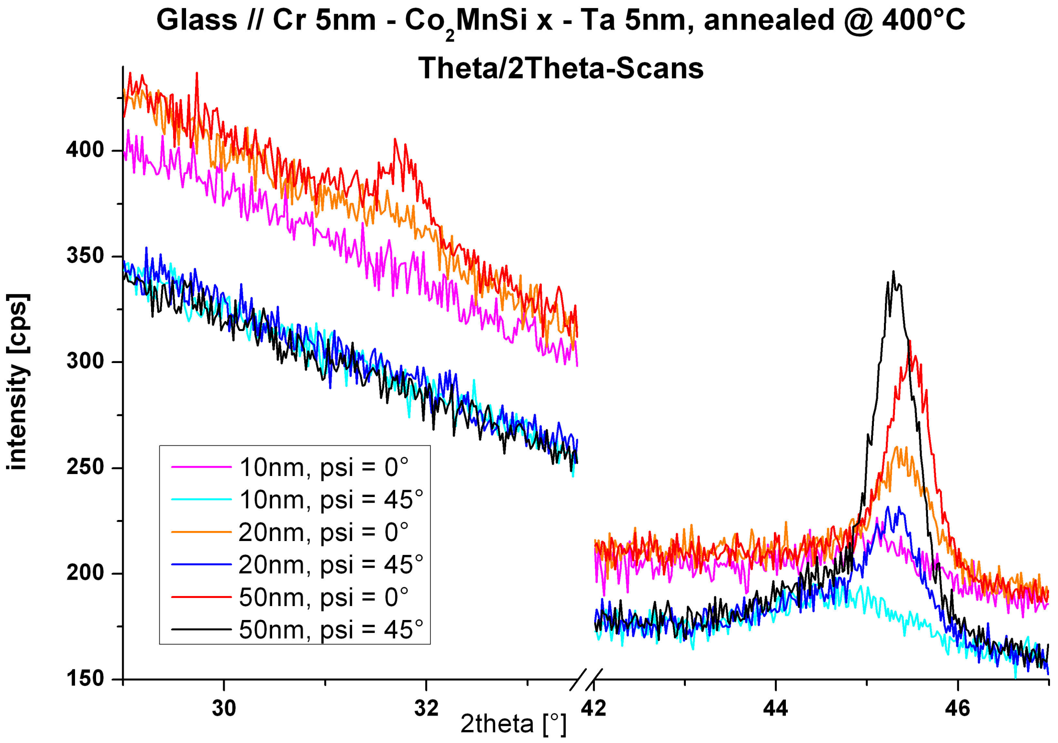

Figure 7.3: Gonio scans showing the (200) and (220) reflexes, for tilt angles $\psi = 0°$ and $\psi = 45°$ for various $Co_2MnSi$ thicknesses. All samples were deposited on glass with Cr seed and annealed at 400°C.

practical reasons, as the deposition of e.g. 100 nm $Co_2MnSi$ would have taken 20 minutes already. All further experiments were performed with 50 nm of $Co_2MnSi$ for that reason.

To verify the first results and to further optimize the seed layer a second matrix with only Cr seed layer was sputtered. This time the Cr thickness was varied (5, 10, 20 and 50 nm). In order to check the conditions in a future TMR stack an MgO barrier as well as a CoFe top electrode were deposited on top of the CMS layer in one set of samples. A different substrate was used this time, namely Si with a 400 nm $Al_2O_3$ layer. There are two main reasons for this change of substrate: Firstly, Si with a top oxide is a standard substrate used by Sensitec for various sensor products and will most likely be used for the TMR wafers with CMS electrodes as well. Secondly, the glass substrates produced a pronounced amorphous background in the XRD scans which made analyses more difficult.

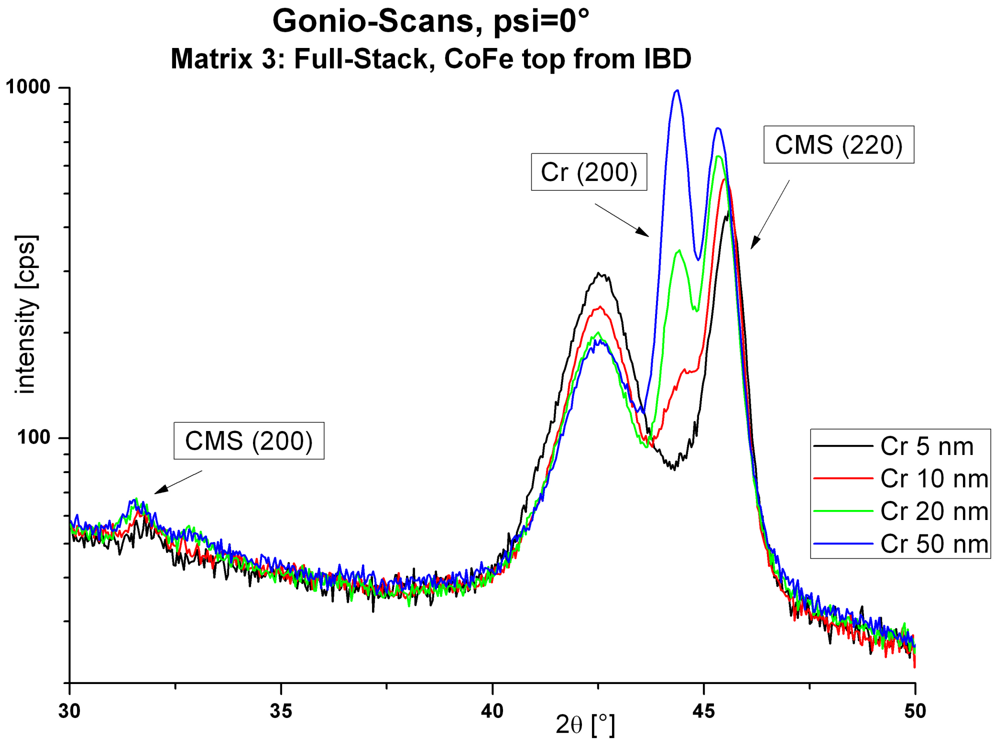

Figure 7.4: X-ray diffraction pattern for Gonio-Scans with $\psi = 0°$ for different Cr seed layer thicknesses. The y-scale was chosen as logarithmic scale for clarification.

Figure 7.4 shows the Gonio scans ($\theta - 2\theta$ -scans) for $\psi = 0°$ for full stacks Cr x / CMS 50 nm / MgO 2 nm / CoFe 3 nm / Ru 5 nm. Apart from the Ru cap layer all layers were deposited in the IBD chamber. As expected, the graph shows the increasing intensity of the Cr(200) reflex with increasing Cr thickness. Additionally the CMS(220) and CMS(200) reflexes are visible, their intensities also slightly increase with increasing Cr thickness. With a 50 nm Cr seed layer the Cr(200) reflex is already more intense than the CMS(220) reflex, which is the one that is to be analyzed. As the intensity of the desired CMS(220) increases only slightly with increasing Cr thickness, 20 nm of Cr seed seem to be ideal. Unfortunately none of these samples showed a clear (100) orientation, as (200) as well as (220) reflexes are found for the same $\psi$ angle. The same result was obtained for the samples with CoFe top electrode from PM4 and samples without CoFe top layer; no decisive difference between these samples could be found (see figure 7.5).

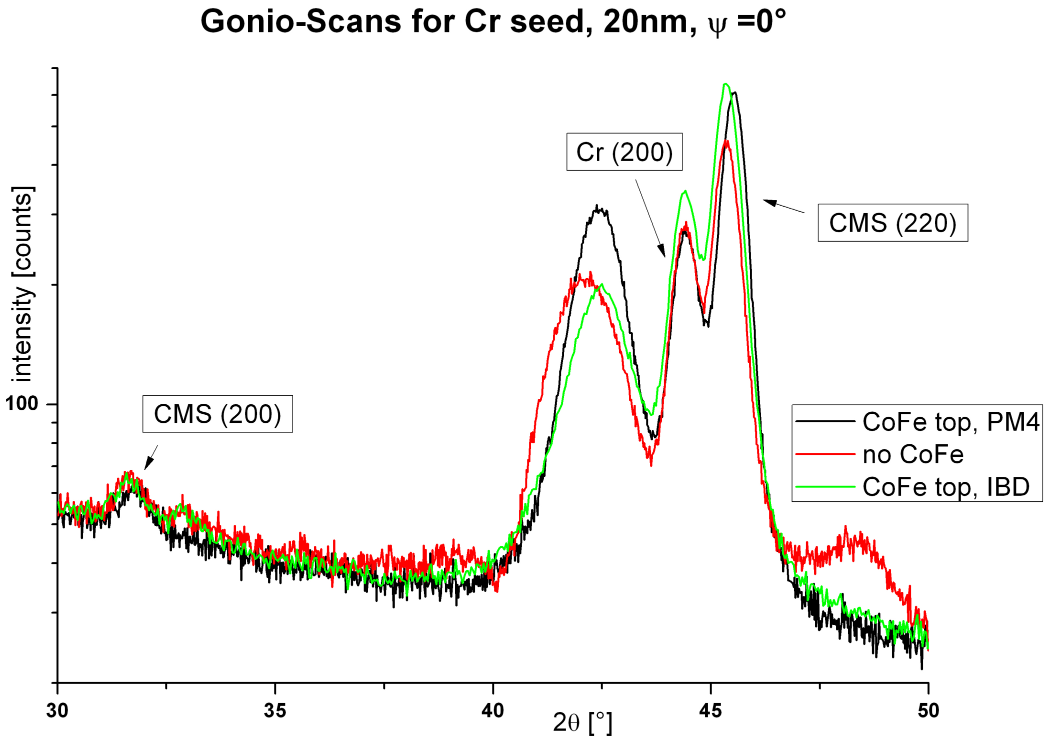

Figure 7.5: X-ray diffraction pattern for Gonio-Scans with $\psi = 0°$ for samples with and without MgO-CoFe top layers. The Cr thickness was fixed to 20nm. The y-scale was chosen as logarithmic scale for better visibility.

In general all diffraction patterns of this matrix showed less noise and clearer characteristic reflexes. These facts were attributed to the different substrate compared to the first samples. However, the unclear orientation of the CMS films is a drawback. As the influence of the different substrate on the CMS film orientation could not be excluded, different types of substrates were tested in another experiment.

Only substrates that are suitable for future wafer production were considered, namely Si / $Al_2O_3$ and Si / $SiO_2$; glass substrates were used for comparison. Because of the results of the Cr thickness matrix mentioned above the Cr thickness was fixed to 20 nm. Although MgO and MgO / Cr had not been successful in the first experiments, those two seed layers were retested. As the deposition of the barrier and top electrode did not show a significant influence on the CMS diffraction pattern, these layers were left out. Table 7.3 lists the samples that

| **Sample** | **Substrate** | **Seed material** | **thickness [nm]** |
|---|---|---|---|
| TM2111a | glass | Cr | 20 |
| TM2111aa | Si + $Al_2O_3$ | Cr | 20 |
| TM2111as | Si + $SiO_2$ | Cr | 20 |
| TM2111b | glass | MgO + Cr | 10 + 20 |
| TM2111ba | Si + $Al_2O_3$ | MgO + Cr | 10 + 20 |
| TM2111bs | Si + $SiO_2$ | MgO + Cr | 10 + 20 |
| TM2111c | glass | MgO | 10 |
| TM2111ca | Si + $Al_2O_3$ | MgO | 10 |
| TM2111cs | Si + $SiO_2$ | MgO | 10 |

Table 7.3: Matrix to check the substrate influence on $Co_2MnSi$ growth.

were deposited to analyze the substrate influence.

Surprisingly this time the MgO / Cr buffer layer turned out to be far better suited than Cr alone, independent of the substrate that was used. MgO seed without additional Cr seed did not work; the CMS seemed to be more or less amorphous, even after annealing. There was almost no difference between $Al_2O_3$ and $SiO_2$ on Si; as expected the samples deposited on glass showed less intensive reflexes and a dominant amorphous background. For practical reasons Si with an alumina passivation was chosen for future wafer experiments, as this type of substrate was best known from TMR stacks with conventional electrodes.

Figure 7.6 shows $\theta - 2\theta$-scans for $\psi$=0° and $\psi$=45° for the first two reflexes, (200) and (220). Although the characteristic peaks are quite broad and the spectra are a bit noisy, one can clearly see that the samples "bX" are (100) oriented and show B2 ordering. However, no (111) reflex was found under $\psi$=53.74° for any sample, which indicates that none of the samples showed perfect $L2_1$ ordering. The results above were reproduced several times with samples from different sputtering runs, on small substrates as well as on whole wafers.

The optimized layer stack that was found with these analyses was Si + oxide substrate // MgO 10 nm / Cr 20 nm / $Co_2MnSi$ 50 nm / CoFe 3 nm / Ru 5 nm. The X-ray diffraction pattern looked promising enough to test the system on a whole wafer and perform TMR measurements. Unfortunately only a tiny effect of 3% TMR could be measured, even with an optimized MgO barrier process. Apparently the Heusler film was only polycrystalline and not ordered enough to

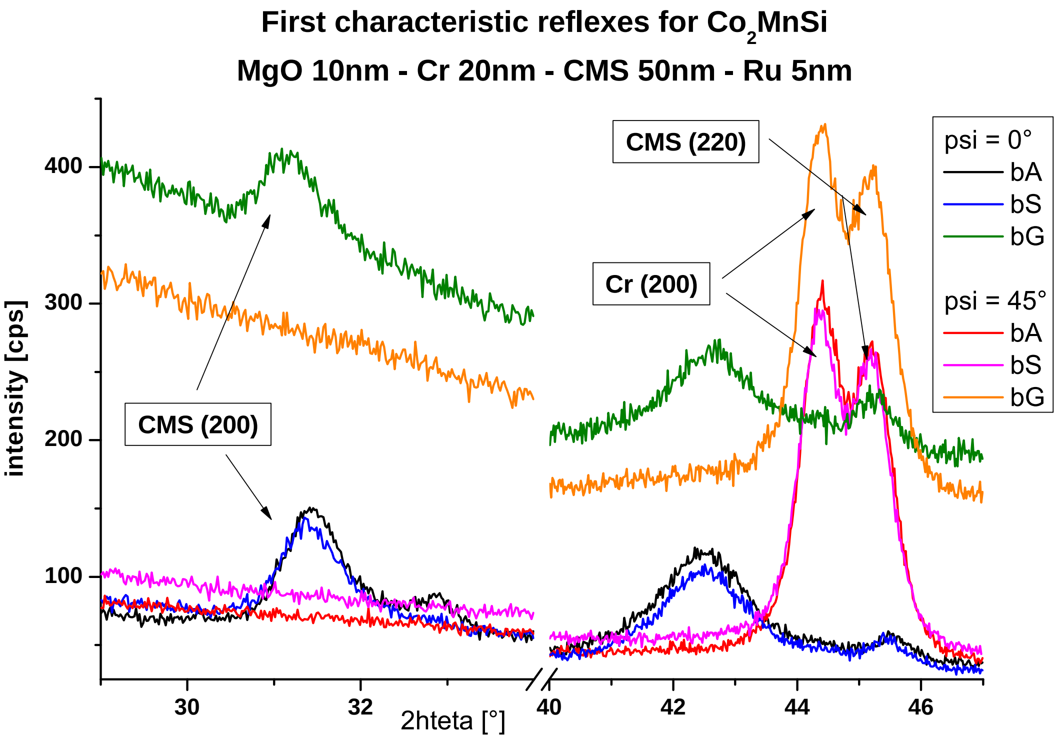

Figure 7.6: $\theta$-$2\theta$ scans for the first characteristic reflexes of Co$_2$MnSi. The scans were performed for different tilt angles $\psi$. The abbreviations stand for the different substrates: "A" = Si + AlOx, "S" = Si + SiOx, "G" = glass.

generate a high TMR.

### 7.1.2 Co$_2$MnSi deposited by IBAD

Having found the optimum seed layer, MgO-Cr, and knowing of the positive effect of the etch gun during the MgO growth, the IBAD process was tested for the deposition of Co$_2$MnSi as well. However, the etch parameters used during the MgO IBAD deposition process were too high; the resulting etch rate was higher than the CMS deposition rate. Increasing the deposition gun's power was impossible with the current hardware setup, therefore further reducing the etch gun's power remained the only option. By reducing the gas flow to 6 sccm (instead of 20 sccm as in case of the MgO) it was possible to operate at 200 V instead of 300 V. The beam current was kept constant at 30 mA. With these low power settings a net deposition rate of 0.49 Å/s was achieved. This lead to an increased deposition time of 17 minutes for a standard 50 nm CMS film, instead of 10 minutes without the assist gun. It turned out that the two guns were not operating reliably over the whole period during the deposition; the beam power was fluctuating. However, a set of samples on different substrates was deposited on the optimized MgO-Cr seed layer and annealed at 400°C.

The samples were characterized with the help of XRD, the results for the first characteristic reflexes were compared with those of the standard deposition process. Figure 7.7 clearly shows that the IBAD process is not an option: Neither the (200) B2-ordering reflex nor the (220) main reflex were found, suggesting an amorphous film growth. Because the standard deposition process yielded better results with a more stable process the experiments on the IBAD process were abandoned completely hereafter.

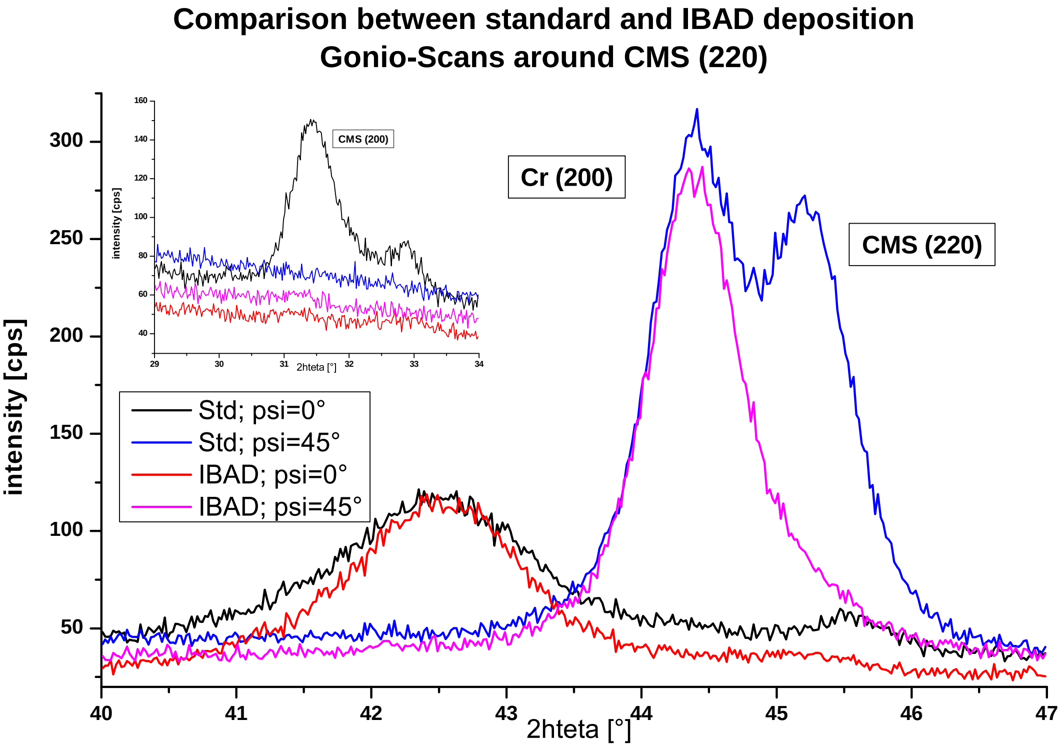

Figure 7.7: $\theta - 2\theta$ scans for the first characteristic reflexes of $Co_2MnSi$ (the inset shows the (200) reflex). The IBAD sample does neither show a (200) nor a (220) reflex.

### 7.1.3 Co$_2$MnSi Thin Films on MgO Substrates

All TMR results published by groups worldwide are based on MTJ systems that were deposited on MgO substrates, which is the ideal underground for growing CMS thin films, presumably even without the need of a seed layer [73]. The lattice parameters of MgO and Co$_2$MnSi match well if CMS grows at an angle of 45° with respect to MgO (see figure 7.8).

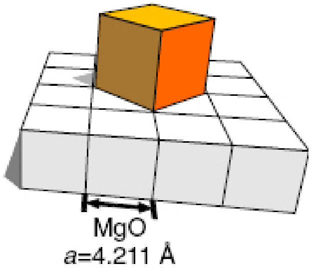

Figure 7.8: Co$_2$MnSi cube on MgO. CMS has a lattice constant of 5.654 Å, which fits well to a 45° rotation with respect to MgO (picture taken from [77]).

The 45° rotation leads to an edge length of 5.955 Åfor the MgO crystal; this results in a lattice mismatch of about 5% with respect to the CMS lattice parameter of 5.654 Å.

In this work MgO substrates had not been considered at the beginning because MgO is not available as five inch wafer and can therefore not be used for TMR stacks that need to be structured. In addition to that, MgO wafers would be far too expensive in a mass production, so using Si substrates for TMR sensors is a must. In order to imitate an MgO substrate a thin film of 10 nm MgO was sputtered onto an alumina covered Si substrate and annealed at 450°C. After the annealing, which had to be done *ex situ*, the remaining Heusler stack was sputtered and the sample was analyzed using X-Ray diffraction. This procedure however, yielded the same result as an MgO seed that had not been annealed before.

In order to prove that ion beam deposition of Co$_2$MnSi works in principle and results in well-ordered films, but does not work on Si substrates, the optimized layer sequence with an MgO-Cr-seed layer and a Co$_2$MnSi film of 50 nm was sputtered on an MgO substrate. An MgO barrier, CoFe top electrode and Ru cap layer were sputtered as well in order to be able to measure TMR if the X-Ray results were promising. The sample was annealed at 350°C for 30 minutes in an $N_2$ atmosphere using the *YES* oven.

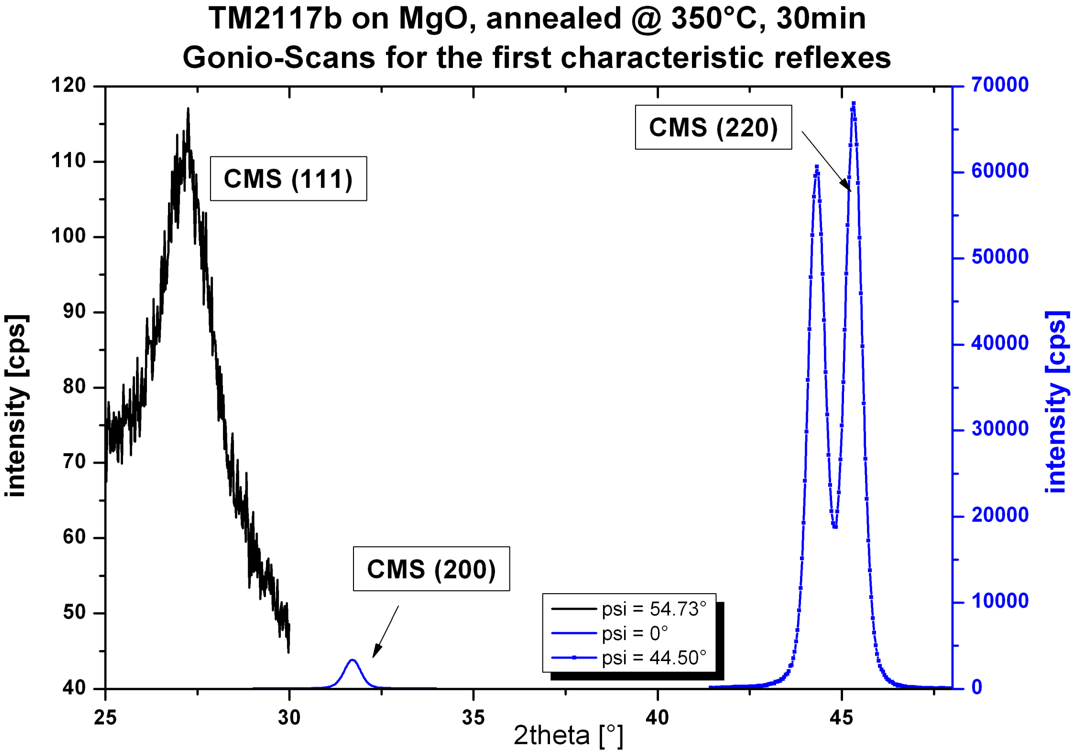

Figure 7.9: $\theta - 2\theta$ scans for the first characteristic reflexes of $Co_2MnSi$. $\psi$ and $\varphi$ have been optimized before. The $L2_1$ ordering reflex (111) can clearly be seen.

X-ray diffraction of this sample revealed a strong (100) out-of-plane texture and was also in-plane-ordered. This sample on an MgO substrate was also the first sample which was not only B2-, but $L2_1$ ordered, i.e. the (111) reflex was found as well. Figure 7.9 shows the $\theta - 2\theta$ scans for the first characteristic reflexes of $Co_2MnSi$. The $\psi$ as well as $\varphi$ angles were optimized separately before. The $L2_1$ ordering reflex (111) can also clearly be seen; however, the intensity is considerably lower than the intensity of the (200) reflexes. In an ideal $Co_2MnSi$ films these two reflexes would have approximately the same intensity, the reduction here indicates that only a small fraction of the film is actually $L2_1$ ordered, the rest shows B2 ordering. The sample was strongly in-plane ordered, which was confirmed by a $\varphi$-scan around the (220) reflex of CMS (not shown). The reason for this is the single-crystalline substrate with only a small lattice mismatch to the lattice constant of Cr and CMS.

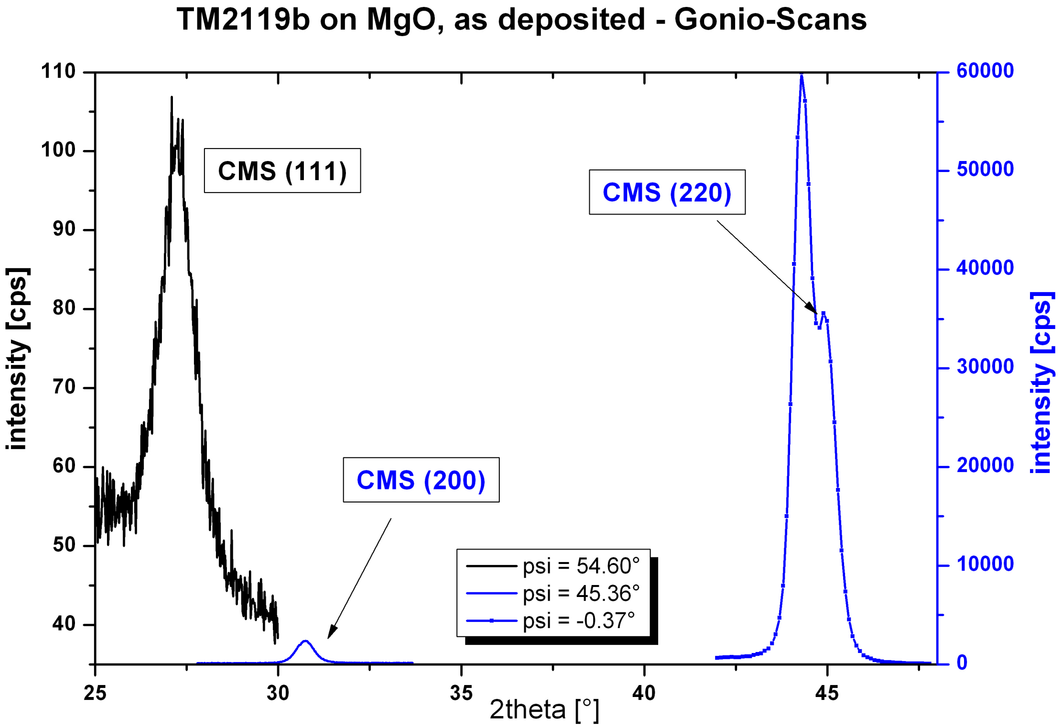

Figure 7.10: $\theta - 2\theta$ scans for the first characteristic reflexes of $Co_2MnSi$ on MgO//MgO/Cr, as deposited. $\psi$ and $\varphi$ have been optimized before. All reflexes are slightly shifted with respect to the theoretical peak positions.

The data shown here belongs to a sample (TM2117b) that was only annealed shortly at a moderate temperature of 350°C. This lead to the question, if $Co_2MnSi$ films on MgO single-crystalline substrates need to be annealed at all or whether a good crystalline quality can also be achieved without annealing. In general low annealing temperatures are favorable for TMR systems because the higher the annealing temperature (and / or time) the higher the risk of diffusion. Especially Mn, from the Heusler electrode or from an antiferromagnetic layer like IrMn, tends to diffuse at high temperatures. A new set of samples was deposited onto MgO single-crystalline substrates and first analyzed without any annealing. Three different seed layers were tested: MgO 10 nm / Cr 20 nm, MgO 10 nm alone and the third CMS film was sputtered without any seed. The stack without any seed layer and the sample with only 10nm of MgO showed no crystalline order at all;

no characteristic reflexes were found with X-ray diffraction. The third sample with the presumably best seed layer, MgO plus chromium, already showed $L2_1$ ordering directly after the deposition. $\theta - 2\theta$ scans for the first characteristic reflexes are shown in figure 7.10.

This result is remarkable, as Heusler thin films are usually not well ordered in an as-deposited state if they were deposited at ambient temperatures [80]. Especially the presence of the $L2_1$ ordering reflex (111) emphasizes the outstanding quality of the CMS thin films on MgO substrates.

After a short annealing of 30 minutes at 350°C all three samples were characterized again: The film which was deposited directly onto the MgO substrate without any seed layer showed only a very weak (220) reflex, the other two samples were both highly ordered (see figures 7.11 and 7.12 for the (220) and (200) reflexes respectively).

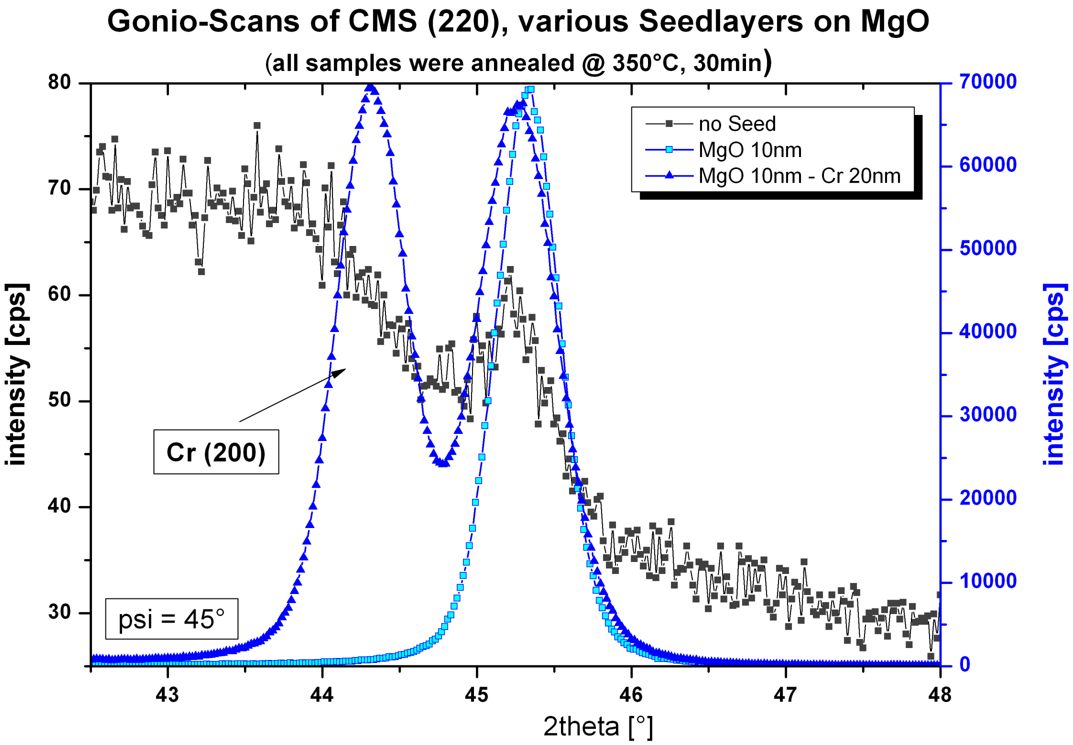

Figure 7.11: $\theta - 2\theta$ scans for the (220) reflex of $Co_2MnSi$ on different seed layers on an MgO substrate. All scans were performed under a tilt angle of 45°.

The sample 19b (with MgO/Cr seed) also showed strong in-plane ordering again; this was verified with $\varphi$-scans around the CMS(220) reflexes before and

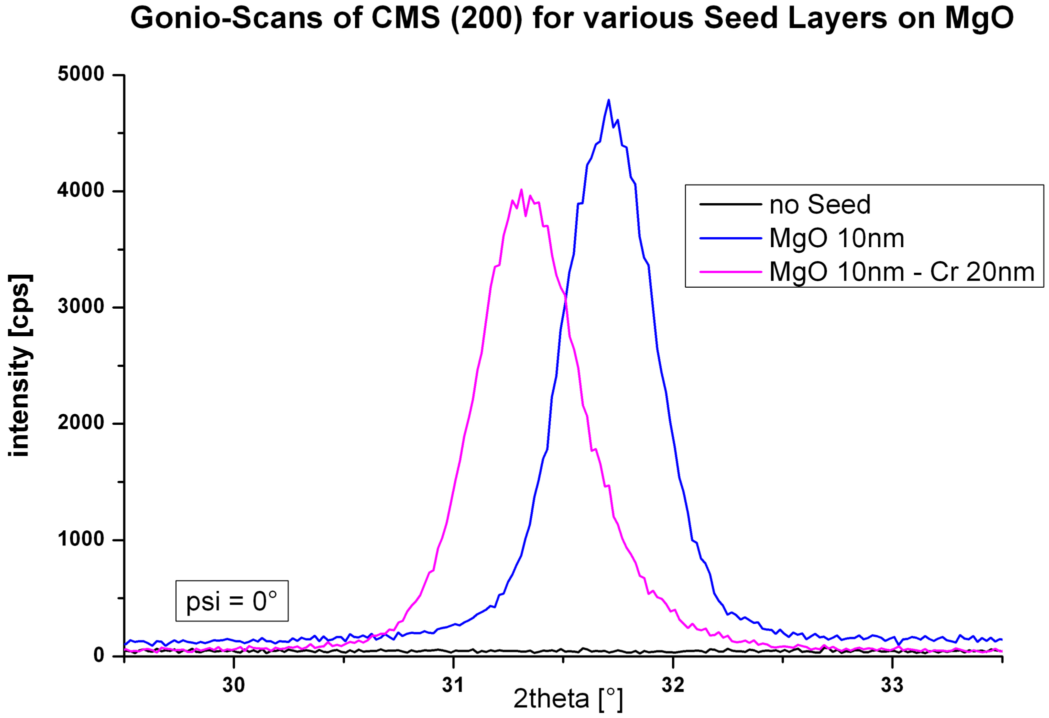

Figure 7.12: $\theta - 2\theta$ scans for the (200) reflex of $Co_2MnSi$ on different seed layers on an MgO substrate. All scans were performed under a tilt angle of 0°. For the sample without any seed the B2 ordering reflex is absent.

after annealing (see figure 7.13). The scans show narrow peaks at a distance of 90° which correspond to the cubic symmetry of $Co_2MnSi$.

The intensity of all reflexes that were analyzed had increased; especially the main reflex (220) and the (200) reflex had become more dominant. This shows the expected increased ordering upon annealing. A comparison between the as deposited and annealed x-ray patterns also shows a peak shift (see figure 7.14) which corresponds to a change of the lattice constant.

The lattice constant is calculated with the help of Bragg's law:

$$d = \frac{n\lambda}{2\sin\theta} \tag{7.2}$$

In this equation $\lambda$ is the wavelength of the radiation used, $d$ is the distance between neighbouring planes in the crystal and $\theta$ is the half value of the peak position. For a cubic crystal like $Co_2MnSi$ $a = b = c; \alpha = \beta = \gamma = 90°$ and

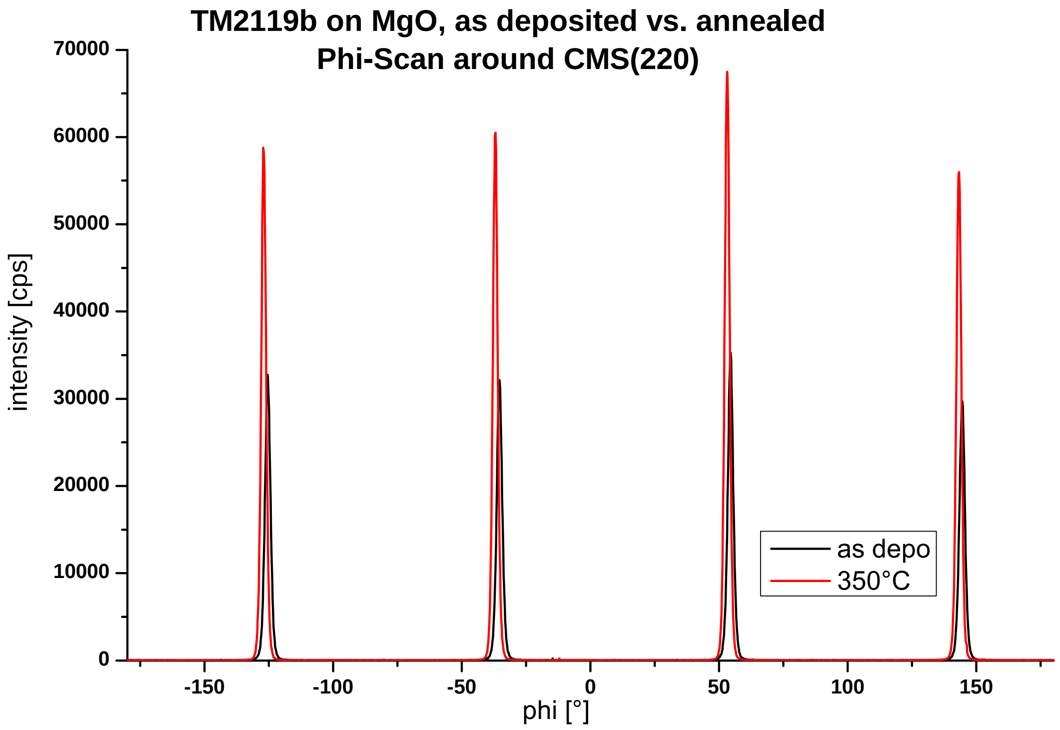

Figure 7.13: In-plane scan ($\varphi$-scan) around the position of the CMS (220) reflex for sample TM2119b on MgO, before and after annealing. The scan reveals a strong in-plane ordering. The peak shift (before vs. after annealing) is due to the manual positioning of the sample on the sample holder and is completely random.

therefore

$$\frac{1}{d^2} = \frac{h^2 + k^2 + l^2}{a^2} \tag{7.3}$$

where $h$,$k$ and $l$ are the Miller indices and $a$ the lattice parameter of the elementary cell. Combining these two equations results in the following relation between the lattice constant, the Miller indices and the corresponding peak position:

$$a = \frac{n\lambda}{2\sin\theta}\sqrt{h^2 + k^2 + l^2} \tag{7.4}$$

The calculated lattice constants are listed in table 7.4. The wavelength of the Cu $K_\alpha$ radiation which was used in the experiments is 1.54056 Å.

This change towards theoretical values means that the film stress is being reduced by annealing the $Co_2MnSi$ thin films. Longer annealing times might fur-

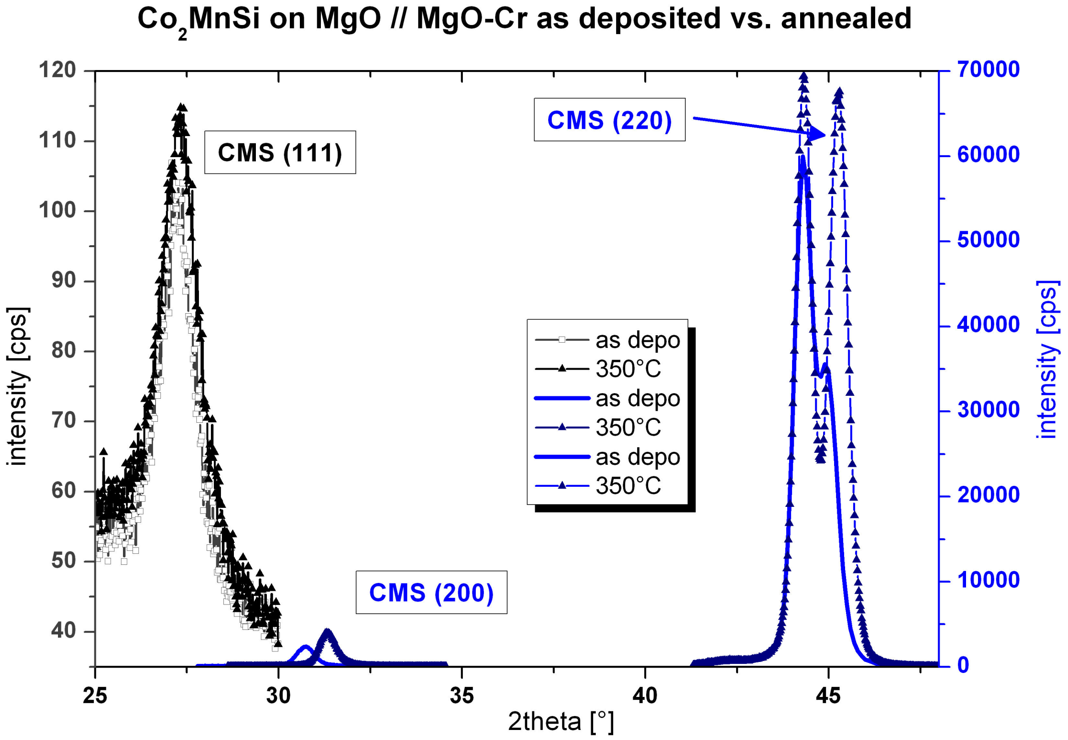

Figure 7.14: $\theta - 2\theta$ scans for the first characteristic reflexes of Co$_2$MnSi on MgO/Cr, as deposited and 350°C annealed sample. Especially (200) and (220) reflexes are shifted more to the theoretical peak positions upon annealing.

| **hkl** | **Annealing** | $2\theta$ [°] | **lattice constant** [Å] |
|---|---|---|---|
| 111 | as deposited | 27.191 | 5.676 |
| 200 | as deposited | 30.735 | 5.813 |
| 220 | as deposited | 44.966 | 5.697 |
| 111 | 350°C | 27.237 | 5.666 |
| 200 | 350°C | 31.344 | 5.703 |
| 220 | 350°C | 45.246 | 5.664 |
| 222 | 350°C | 56.398 | 5.647 |
| 400 | 350°C | 65.341 | 5.708 |

Table 7.4: Peak positions of the first characteristic reflexes and resulting lattice constants. The peak positions were determined with the help of *Philips X'Pert Data Viewer*. The theoretical lattice constant is 5.670 Å[72].

ther reduce the stress in the films. Additionally the intensity of the characteristic peaks increased significantly; this indicates the growth of the grains within in the $Co_2MnSi$ film.

Rocking curves, i.e. $\omega$-scans for a fixed $2\theta$-position, were also performed for some of the reflexes and their position and width were compared before and after annealing. As expected, the peaks became narrower upon annealing and were also slightly shifted. A narrower rocking curve, i.e. a smaller FWHM value, indicates a higher degree of ordering: the different planes that contribute to this reflex are not tilted to one another in $\omega$ as much as before, resulting in a more intense peak that is not as broadened as before. The rocking curves of the first characteristic reflexes are shown in figure 7.15.

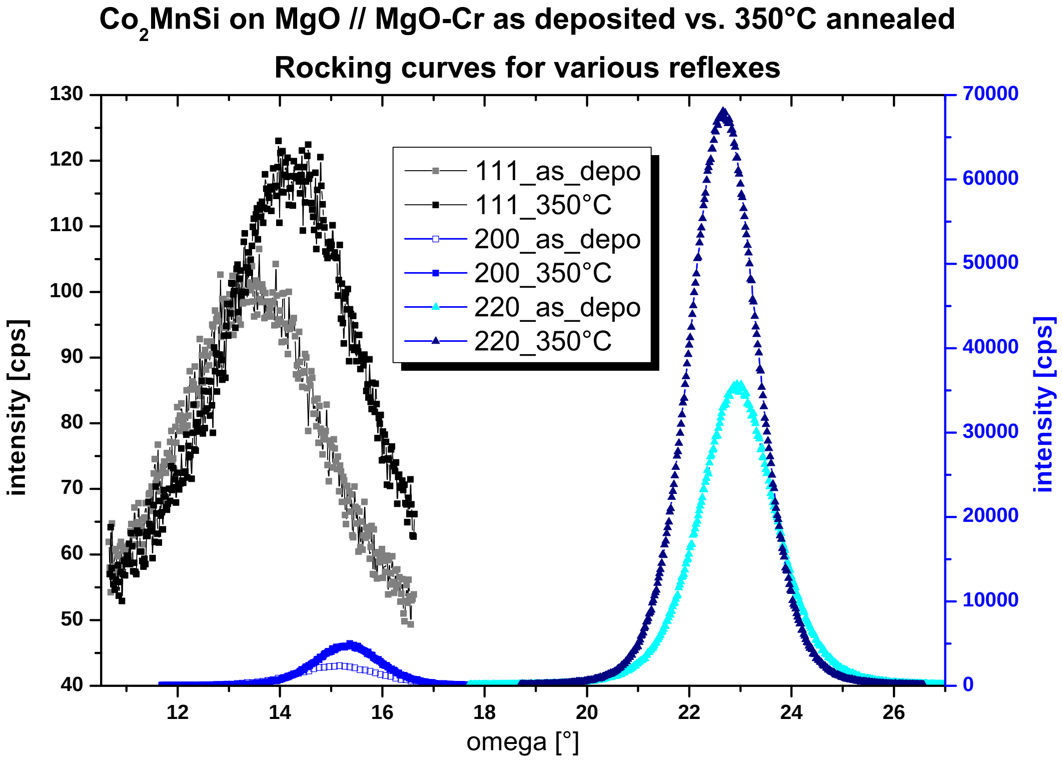

Figure 7.15: $\omega$ scans around the position of the first characteristic reflexes before and after annealing. The peaks are slightly shifted after annealing and become narrower and more intense.

The graphs were fitted using *Origin 8.1G*'s PseudoVoigt-Function; the resulting peak centers, widths and areas are summarized in table 7.5. One can see that "w", which denotes the peak width, has decreased for all reflexes; at the same

| **Parameter** | **as deposited** | | **350°C** | |
|---|---|---|---|---|
| | value | standard error | value | standard error |
| **CMS (111)** | | | | |
| x$_c$ [°] | 13.42687 | 0.0094 | 14.18956 | 0.00813 |
| A [°·cps] | 214.09377 | 50.08878 | 262.71691 | 34.82321 |
| w [°] | 3.32408 | 0.19172 | 3.12338 | 0.09576 |
| **CMS (200)** | | | | |
| x$_c$ [°] | 15.12984 | 0.00387 | 15.31896 | 0.00124 |
| A [°·cps] | 5359.03243 | 214.44316 | 8479.75511 | 63.79366 |
| w [°] | 1.89406 | 0.01481 | 1.50055 | 0.00375 |
| **CMS (220)** | | | | |
| x$_c$ [°] | 22.93752 | 0.0007 | 22.66955 | 0.0004 |
| A [°·cps] | 78636.81097 | 240.99211 | 129199.8842 | 311.58981 |
| w [°] | 1.75094 | 0.00215 | 1.57593 | 0.00118 |

Table 7.5: Peak centers, widths and areas of the rocking curves of the first characteristic reflexes of sample TM2119b on MgO. The data was analyzed with *Origin*.

time the peak area ”A” has increased. These two parameters combined stand for a higher degree of crystallization.

### 7.1.4 Co$_2$MnSi Thin Films in (110) Orientation

In general (100) orientation of the electrodes is favourable in combination with an MgO(100) tunneling barrier. In the case of half metallic electrode materials however, the MgO's special ”filtering effect” is not needed to achieve extremely high TMR values. Therefore also (110) orientated Heusler electrodes can be incorporated into MTJs under the condition that the spin polarization in the (110) is equally high than for the (100) direction. For example, Hattori *et al.* prepared junctions with a CMS(110) bottom electrode and an alumina barrier and were able to achieve 40 % TMR at room temperature; at lower temperatures the TMR increased up to 120 % at 2K [81].

NiFeCr/NiFe (magic seed) is known for its ability to induce a (110) fibre texture; this was also shown for the Heusler alloy Co$_2$Cr$_{0.6}$Fe$_{0.4}$Al [82]. First samples with CMS on glass also indicated (110) texture, however, crystalline quality was rather poor. The experiment was repeated on the standard wafer substrate Si with 400 nm $Al_2O_3$, the sample was annealed at 350°C for 30 minutes. In figure 7.16 the X-ray diffraction scans for the (220) and (200) reflexes are shown. As expected the most intense peak (220) is found only for $\psi = 0°$, which corresponds to a (110) orientation of the film. Under a tilt angle of 45° the B2 ordering reflex (200) is present. As the film is not in-plane ordered, which is always the case for a sputtered film on an amorphous underground, the intensity of the (200) reflex is reduced compared to the theoretical value: The intensity is equally distributed among all $\varphi$ angles. The $L2_1$ ordering reflex (111) was not present, indicating a B2 ordered film.

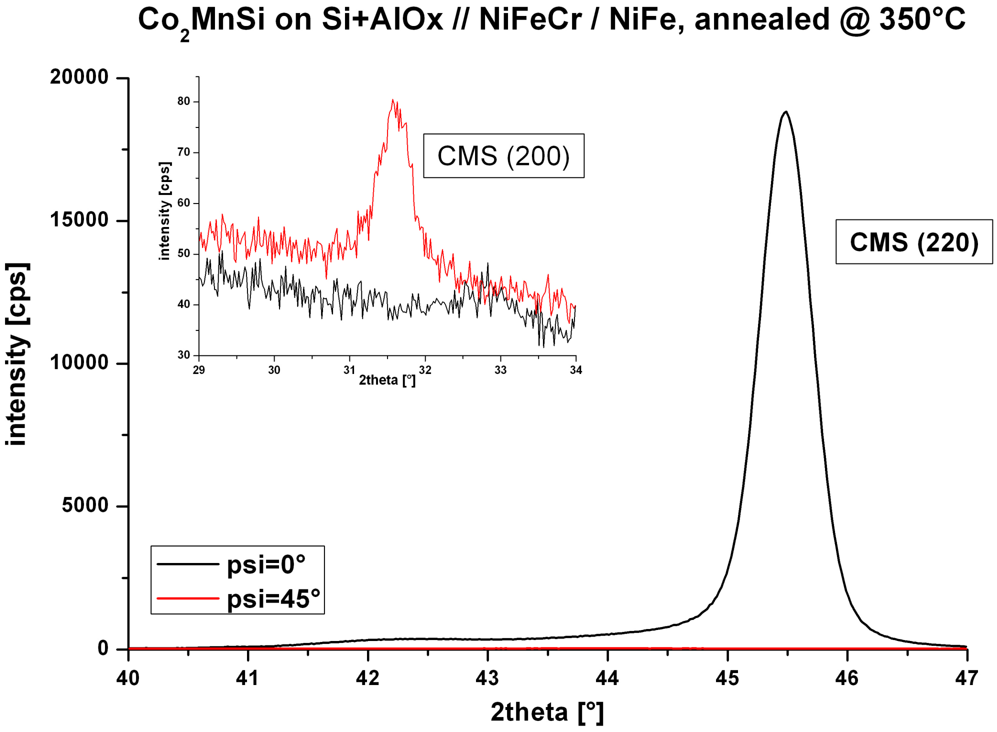

Figure 7.16: $\theta - 2\theta$ scans around the position of the $Co_2MnSi$ (220) reflex for a sample on magic seed. The (220) reflex is found only for $\psi = 0°$ which corresponds to a (110) orientation of the film. The inset shows the (200) reflex.

## 7.2 X-Ray Reflectometry

Apart from the crystalline quality of thin films their thickness and surface roughness are of major interest. Therefore X-Ray Reflectometry (XRR) was used to verify the film thickness perviously determined by profilometer measurements and to quantify the mean film roughness of all layers in a simple Heusler stack.

In XRR monochromatic X-rays of wavelength $\lambda$ at grazing incident angles $\omega$ are reflected from the surface and the interfaces of a multilayer stack. The reflected intensity is detected at the angle $2\theta$, where the incident angle $\omega = 2\theta/2 = \theta$ ($\theta$ is the outgoing angle). Reflections from different interfaces lead to interference fringes that can be used to calculate both, layer thicknesses and roughness. In general one can say that the period of the fringes is related to the layer thickness and the intensity loss at increasing angles theta corresponds to the surface or interface roughness.

A simple full stack with the following layer sequence and nominal thicknesses was used for the analysis: Si substrate // $Al_2O_3$ 400nm // MgO 10nm - Cr 20nm - $Co_2MnSi$ 50nm - MgO 2nm - CoFe 3nm - Ru 7nm. The sample had been annealed at 350°C for 30 minutes in $N_2$ atmosphere. At Sensitec a *Bede D1 Diffractometer* with Cu $K_\alpha$ radiation ($\lambda = 1.541$ Å) is used for the measurements. Data analysis is performed with the help of the commercial software *Bede REFS*. The reflection data as well as the fit for the sample mentioned above is shown in figure 7.17; the resulting thicknesses and roughnesses are summarized in table 7.6.

| **Material** | **nom. Thickness [Å]** | **real Thickness [Å]** | **Roughness [Å]** |
|---|---|---|---|
| MgO | 100 | 97.51 | 4.95 |
| Cr | 200 | 203.31 | 1.01 |
| $Co_2MnSi$ | 500 | 417.54 | 6.27 |
| MgO | 18 | 29.63 | 4.06 |
| CoFe | 30 | 25.98 | 7.56 |
| Ru 1 | 70 | 63.98 | 4.79 |
| Ru 2 | 0 | 14.42 | 10.52 |

Table 7.6: Fit of XRR data for a Heusler full stack. The goodness of the fit was 0.081. The upper Ru layer has a reduced density, corresponding to a top oxide layer.

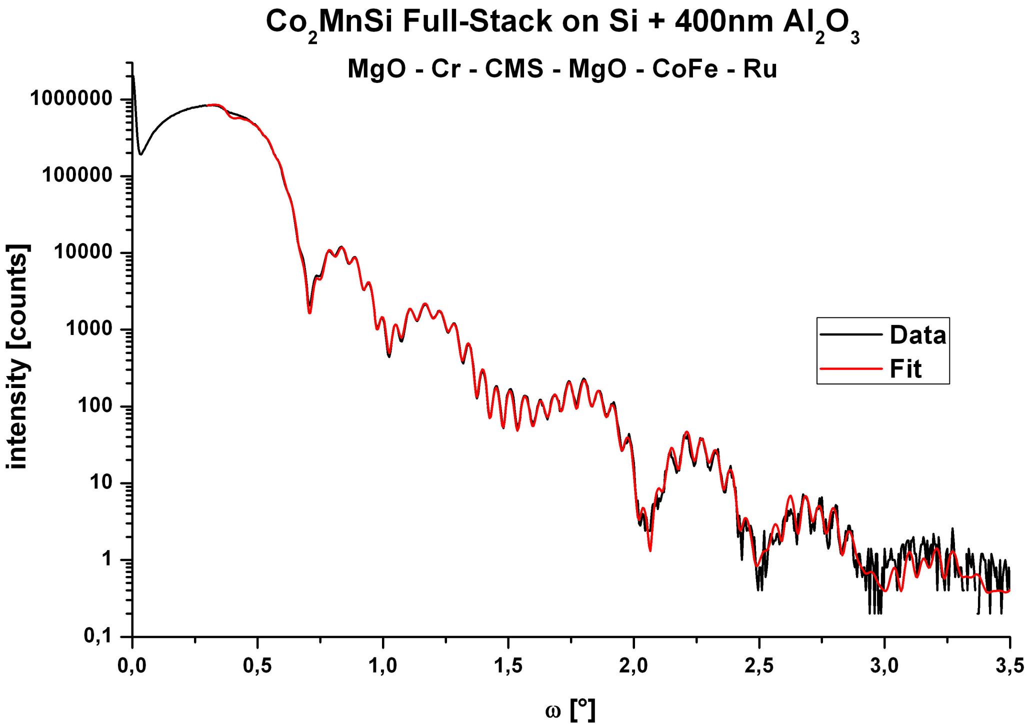

Figure 7.17: XRR data and fit for a simple Heusler stack "seed - $Co_2MnSi$ - top" deposited on Si//$Al_2O_3$.

One can see a rather large discrepancy between the nominal thicknesses and the real or fitted values for the Heusler film and the MgO barrier. There are two possible explanations for a thicker barrier than expected: Firstly the deposition rate was wrongly calculated or has changed over time or, secondly, the electrodes are oxidized at the interfaces with the MgO barrier. As a distinction between MgO and a "Heusler-oxide" is impossible to do with XRR, the actual cause for the additional oxide remains unclear. An interface oxide could also explain the high MTJ resistance, which was measured on all TMR wafers with CMS electrodes, as well as the tiny TMR ratios (see section 7.4). At the same time the interface and surface roughnesses are very good, the 42 nm Heusler thin film has a roughness of only 6 Å. A smooth film surface is a requirement for high quality TMR stacks, otherwise pinholes could occur which destroy the tunneling process. With this reflectometry analysis it has been proven that the ion beam process is capable of producing Heusler films of the required quality.

## 7.3 Magnetic Characterization

Hysteresis measurements were performed for 50 nm $Co_2MnSi$ films deposited on different seed layers (Cr; MgO-Cr; MgO) and different substrates (glass; Si + $Al_2O_3$; Si + SiOx). A substrate influence on the magnetic properties was visible, but as expected the general trend that could be seen by varying the seed was the same for all substrate types (see figure 7.18). A relatively low coercivity of 15 Oe was measured for MgO-Cr seed layer, the Cr seed alone led to a doubling to 31 Oe and the MgO seed layer resulted in a high coercivity of 105 Oe. These values indicate an improved film quality, like higher degree of ordering or larger grains in the polycrystalline film, of the CMS films deposited on MgO-Cr, which confirms the XRD results [83].

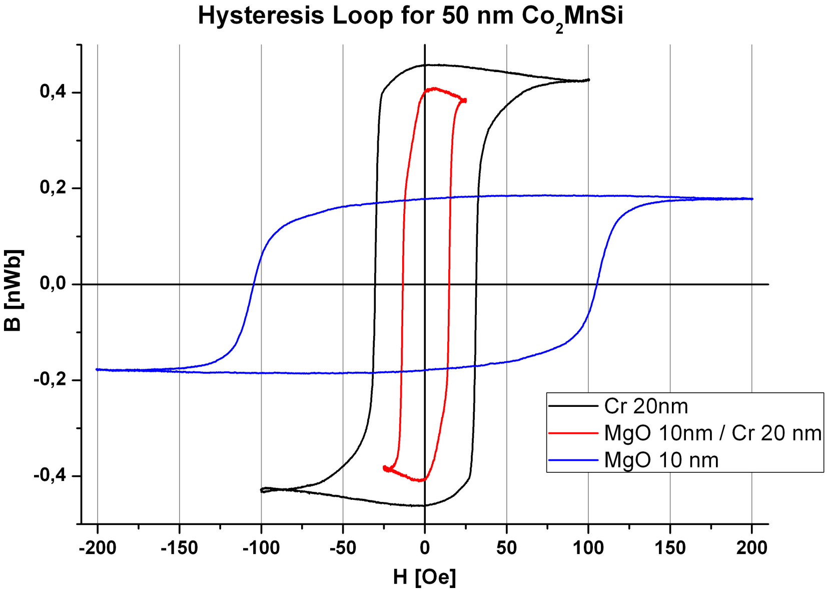

Figure 7.18: Hysteresis loop for 50nm $Co_2MnSi$ deposited on different seed layers. All films were deposited onto Si substrates with $Al_2O_3$ passivation.

To determine the magnetic moment of the CMS films room temperature VSM measurements were performed with small coupons of 10 mm x 10 mm size and glass coupons of 18 mm in diameter. For the calculation of the moment the sample volume had to be known, i.e. the exact thickness of the film as well as the sample area. The thicknesses had been evaluated by XRR measurements before with different samples, the determination of the sample area is more difficult. The substrates had a well defined size, however, they had to be fixed with adhesive tape or small screws to 5 inch wafers during sputtering. For that reason the effective sample area varied slightly from sample to sample; an average value was used for the calculation of the moment.

The calibration of the VSM had been done with a small Nickel standard which was considerably smaller than the samples measured here. Therefore the absolute value was 4 % too large in the case of the 10 mm x 10 mm samples and even 11 % in the case of the glass substrates for the VSM setup used [84]. This has been corrected in the presented data already. Additionally a y-offset has been corrected for all data shown, i.e. the graphs have been centered around the y-axis.

The measurements were done before and after annealing; different film thicknesses were also compared. It turned out that the magnetic moment per volume increased with increasing film thickness; at the same time the coercive field decreased (see figure 7.19 for films on glass substrates). In perfect samples, the moment, which is normalized to the sample volume, should be constant. An enhanced magnetic moment with increasing thickness suggests a higher degree of

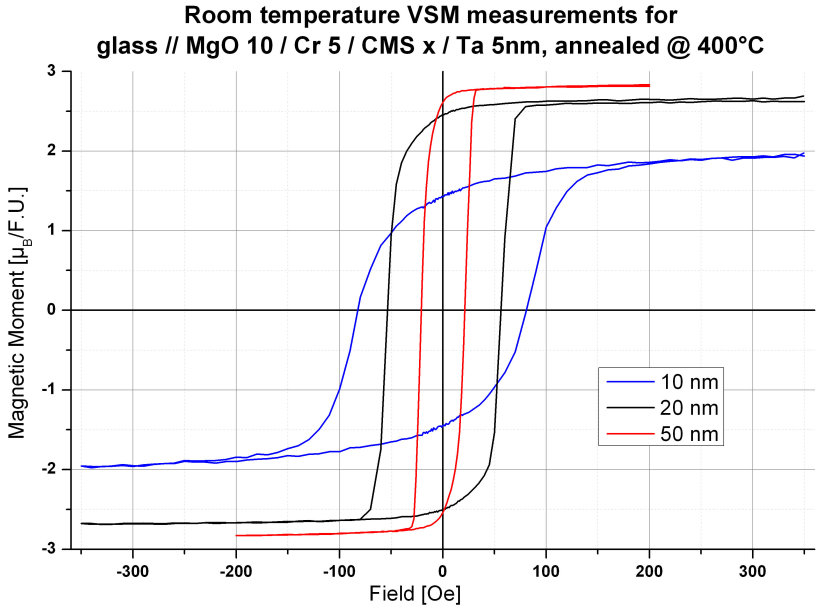

Figure 7.19: Room temperature VSM measurements for samples with 10, 20 and nm of $Co_2MnSi$ on MgO/Cr seed layer. All samples were deposited on circular 18 mm glass substrates and annealed at 400°C. The magnetic moment increases with increasing film thickness; at the same time the hysteresis decreases.

ordering in the films with increasing thickness. This result was expected as the X-ray diffraction analysis had revealed the same thickness dependence (see figure 7.3). The decreased coercivity confirms the higher quality of the thicker films: Crystalline imperfections in a sample make the return to the original, unmagnetized state more difficult, which in turn increases the coercivity.

Different seed layers were also compared; the highest magnetic moments were achieved with MgO/Cr seed, which also yielded the best results in X-ray diffraction as far as crystalline ordering is concerned. Surprisingly, the samples with magic seed also showed poor magnetic properties, but also the crystalline quality of the first set of samples with magic seed was only weakly polycrystalline. However, a newer set of samples with Ru cap, which also showed a strong (110) fibre texture in the XRD patterns, yielded far better magnetic ordering as well. The data from both, the old and new sample with magic seed, is included in figure 7.20. Apart from the second sample with magic seed only Cr-seed and MgO-Cr double seed layer showed a reasonable magnetic moment. The coercive field of the Cr-sample is the highest of all samples that were analyzed.

The magnetically softest film, i.e. film with the lowest coercivity, was achieved with a MgO/Cr seed layer. Here the coercive field was only about 20 Oe. Ru, Ta and MgO seed are unsuitable according to the magnetic data; the magnetic moment was about one order of magnitude lower than for Cr, MgO/Cr and magic seed. Qualitatively this also confirms the X-ray diffraction results.

CMS films of different thicknesses deposited on MgO/Cr-seed, this time on an MgO substrate, were also compared. The corresponding VSM measurements are shown in figure 7.21.

The coercive field of the 10 nm thick sample is about twice as large as for the 20 and 50 nm thick sample, which again suggests a lower quality of the 10 nm sample. In contrast to the samples deposited on glass substrate the magnetic moment is only slightly reduced compared to the thicker films.

The magnetic moments for different annealing temperatures of samples with identical stacks sputtered in the same run were also compared: After 300°C annealing only for MgO/Cr seed lead to a clear hysteresis curve; all other samples appeared to be almost unmagnetic. After 500°C annealing the moments decreased again; the corresponding VSM graphs for MgO/Cr seed are shown in figure 7.22.[3]

---

[3] It should be noted however, that some of the 500°C-samples showed visible signs of corrosion, which may have destroyed the Heusler film despite the Ta cap. Unfortunately the high temperature *Blue M* Oven had an oxygen leakage problem, so the 500°C tests could not be

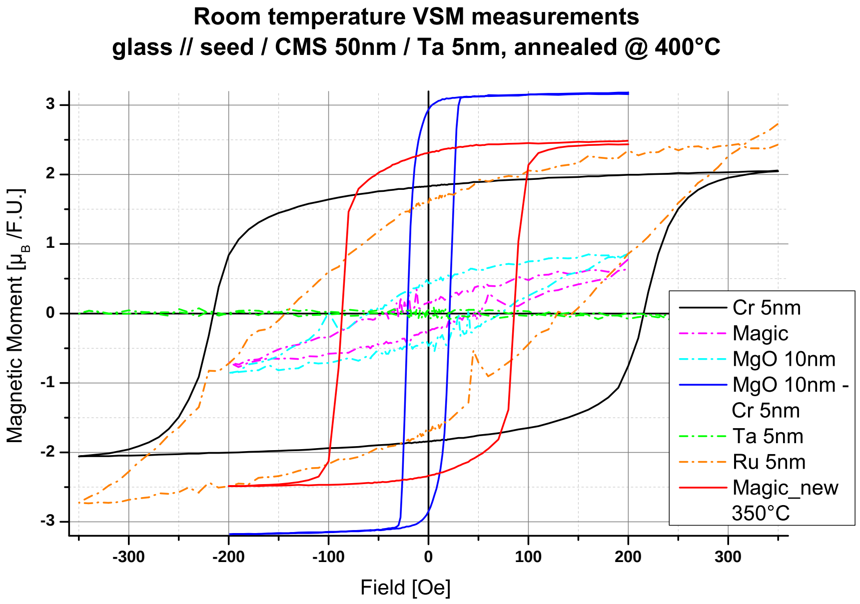

Figure 7.20: Room temperature VSM measurements for samples with 50 nm $Co_2MnSi$ on different seed layers. All samples were deposited on circular 18 mm glass substrates and annealed at 400°C; except for the last sample, "magic-new", which was annealed at 350°C. Please note, that for better visibility the dashed graphs were scaled by a factor of ten in the y-direction.

The best results were achieved after a 400°C annealing for 20 minutes in the *Blue M* oven or with a 350°C annealing for 30 minutes in the *YES* oven.

In order to judge the film quality the most important figure of merit is the magnetic moment per formula unit (F.U.), which has been used here as well. To compare the VSM results the data has to be converted from emu/cm$^3$ to $\mu_B$/F.U. via a conversion factor of 201.84 cm$^3$/emu. This factor can be derived as follows:

$$\frac{m[emu]}{V_{sample}[cm^3]} = \frac{m[emu]}{V_{sample}[cm^3]} \cdot \frac{V_{unitcell}[cm^3]}{\mu_B[emu]} = \frac{1}{K} \cdot \frac{m[emu]}{V_{sample}[cm^3]} \tag{7.5}$$

where

$$K = \frac{\mu_B[emu]}{V_{unitcell}[cm^3]} = \frac{\mu_B[emu]}{4 \cdot V_{F.U.}[cm^3]} = \frac{9.27410 \cdot 10^{-21}}{4 \cdot (5.68 \cdot 10^{-8} cm)^3} = 201.84 \frac{emu}{cm^3} \tag{7.6}$$

---

repeated.

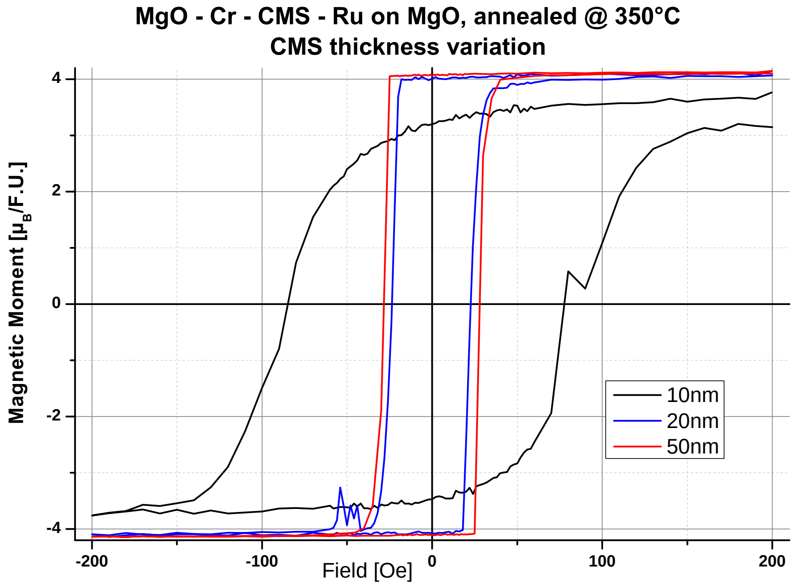

Figure 7.21: VSM measurements for different CMS thicknesses on MgO. 20 nm and 50 nm show nearly an identical magnetic moment, 10 nm seems to be less ordered.

The theoretical value for the magnetic moment is 5.0 $\mu_B$/F.U.; however, this theoretical value is normally achieved in bulk samples only, not in thin films [85]. This bulk value was also not reached with the samples prepared in this thesis; the maximum value achieved was about 3.7 $\mu_B$/F.U.. This deviation from the theoretical bulk value can either be attributed to disorder in the films (mainly B2 instead of perfect $L2_1$ ordering) and / or to an off-stoichiometry of $Co_2$MnSi [78].

## 7.4 Transport Measurements

Thin films of $Co_2$MnSi had been characterized and optimized to result in the best crystalline quality possible. However, on Si substrates good crystallinity could only be achieved with NiFeCr/NiFe seed, resulting in a ”wrong” (110) orientation of the Heusler film. Therefore the symmetry filtering effect of an MgO barrier could not be used, as this requires the electrodes and the barrier to be (100) oriented. (100) orientation could be achieved with MgO/Cr seed, but on Si substrates the films remained polycrystalline. Nevertheless simple, unpinned

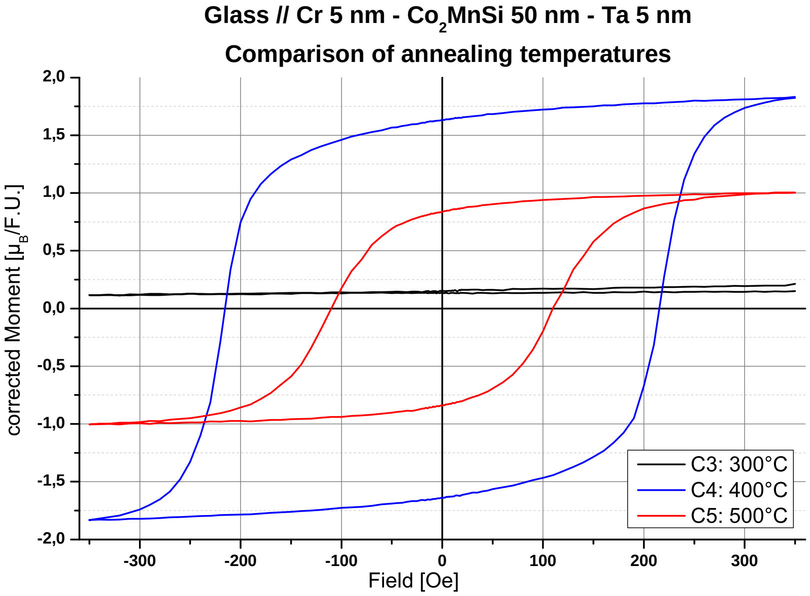

Figure 7.22: VSM measurements for different annealing temperatures of $Co_2MnSi$. All stacks had the sequence glass // Cr 5nm - CMS 50nm - Ta 5nm and were annealed for 20 minutes at different temperatures in the *Blue M* oven.

TMR stacks were deposited onto Si substrates with different seed layers, namely NiFeCr/NiFe and MgO/Cr. The layer sequence was as follows: Si + 400 nm $Al_2O_3$ // seed - $Co_2MnSi$ 50nm - MgO x nm - $Co_{90}Fe_{10}$ 3 nm - Ru 7nm. Different barrier thicknesses were tested, using the optimized recipe described in chapter 6.3.4. Quadrants wafers were deposited and annealed at 350°C for 30 min in a nitrogen atmosphere without magnetic field. The wafers were then structured using the normal process flow and tested at room temperature. Unfortunately only very small MR ratios of a few percent could be measured. The current-voltage dependence however revealed a clear non-linear tunneling characteristics. It turned out that the resistance of the barrier was still about one or two orders of magnitude too high, despite the previous optimizations of the MgO barrier process. Reducing the deposition time drastically reduced the resistance, but still the TMR ratios did not improve[4].

---

[4] Tsunegi *et al.* observed a similar effect in CMS-MgO-CoFe stacks with a sputter-deposited barrier [86]. The resistance was 1000 times higher in these stacks than in CoFeB-MgO-CoFeB stacks with a barrier of the same thickness. This was attributed to electron scattering at the electrode-barrier interface.

Tests with CMS TMR stacks on MgO substrates were also performed in order to test whether a better crystalline quality improved the achievable TMR ratio. The samples were sputtered at Sensitec; structuring and testing were done in Bielefeld using the standard equipment there. Unfortunately the barriers turned out to be too thick in all samples, only small TMR ratios of about 3 % were measured (see figure 7.23). The characteristic curve (IU) however clearly showed a nonlinear behaviour; the Brinkman-fit of the derivative verified a thick barrier of 2.4 nm (see 7.24)[87].

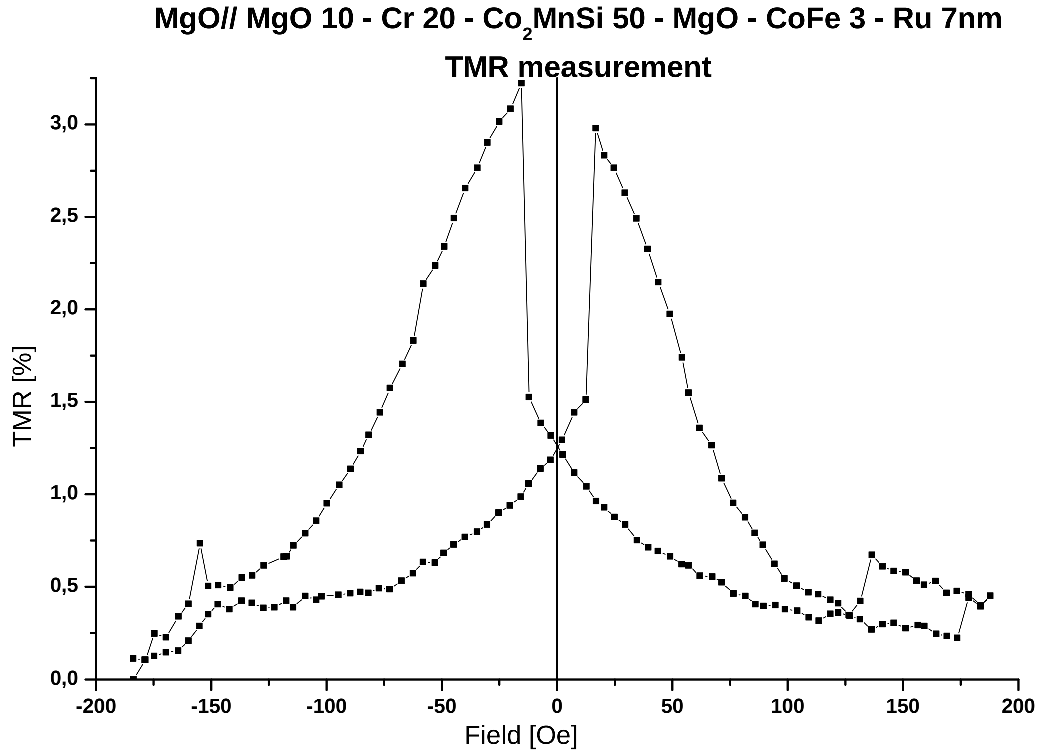

Figure 7.23: TMR measurement for a sample with MgO // MgO 10 - Cr 20 - MgO - CoFe 3 - Ru 7nm, annealed at 350°C for 30 min. The graph does not show a clear plateau because none of the electrodes was pinned and in the square junction form anisotropy cannot arise.

Because of reasons that are not completely understood at the moment it is not possible to deposit Co$_2$MnSi and MgO in the IBD chamber in the same process sequence. Despite comprehensive optimization work (see chapter 6.3) reasonably high TMR ratios could not be achieved with Co$_2$MnSi electrodes and an

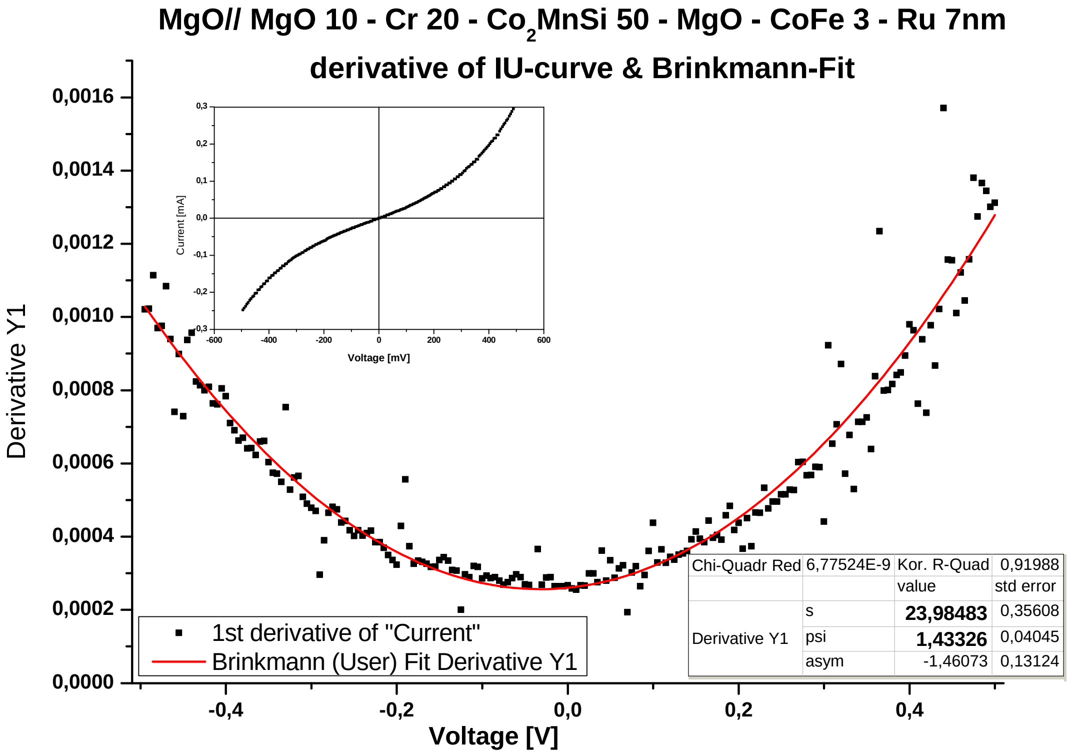

Figure 7.24: Derivative and Brinkman fit of the IU curve for a sample with MgO // MgO 10 - Cr 20 - MgO - CoFe 3 - Ru 7nm, annealed at 350°C for 30 min. The sample has been structured in Bielefeld using the standard procedure for UV lithography and Ar ion etching. The inset shows the original IU-curve.

IBD-deposited MgO barrier. A possible work-around could be separate the MgO-deposition from the CMS-deposition. Work on an MgO barrier could continue in a different chamber (e.g. the single-target chamber PM 5) or a $Co_2MnSi$ target could to be installed in the DC magnetron chamber PM 4 instead. The second option is very likely to work: First results achieved in the *MultiMag* project with $Co_2FeAl_{0.5}Si_{0.5}$ from the PM 4 and an MgO IBAD barrier are very promising [9]. Two of the reasons for the use of the IBD chamber for the Heusler deposition had been the very good vacuum and the ability to deposit almost the complete stack within the same chamber; both advantages would be lost in that case.

Another option to circumvent the problem of MgO deposition after CMS sputtering is to use an alumina barrier instead of an MgO barrier. Here again a different chamber (PM 5) would be used, so a conditioning problem of the barrier-deposition-chamber can be excluded. In general MgO barriers are favourable and the lattice mismatch between CMS and MgO is small, resulting in good crystallinity of both layers. However, in case of a perfectly ordered Heusler electrode with an optimum spin polarization the "filtering effect" of an MgO barrier would not be needed to enhance the MR ratio. High TMR ratios of 159 % at 2K and 70 % at room temperature have already been reported for MTJs with CMS bottom electrode, alumina barrier and top-pinned CoFe electrodes [75]. For sensor applications as targeted by Sensitec, these MR ratios would be sufficient. However, with the current tool configuration a stable plasma oxidation at low power as required for the formation of an alumina barrier is not possible. Therefore to test an MTJ with CMS electrode and alumina barrier the Heusler target would have to be moved to another sputtering machine with a more stable match box or the match box of PM 5 in PVD 2 would have to be modified.

# Chapter 8

# Summary and Outlook

In this work a TMR process based on an MgO tunnel barrier has been developed in an industrial environment. All development work was performed directly on industrial machinery suitable for mass production. TMR values around 70 % after moderate annealing at 265°C were achieved with a system containing an MgO barrier and conventional CoFeB electrodes. By annealing at higher temperatures up to 500°C the TMR ratios could be increased to about 140%. The TMR wafer distribution over a five inch wafer was reasonably good, however the resistance distribution will have to be improved in the next step of a product development phase.

Possible applications of TMR sensors are evaluated at the moment in the BMBF project *MultiMag* which is a collaboration between Sensitec and the universities of Bielefeld, Mainz and Kaiserslautern [9]. Work in this project concentrates on TMR sensors for high temperature applications and an array sensor, both making use of the ion beam MgO barrier process that was developed in this thesis. For sensor applications a linear response to an external magnetic field is required; the transfer curves presented in this thesis will therefore have to be linearized. To meet this requirement a sensor architecture with two orthogonally pinned electrodes has already been developed at Sensitec in the *Camel* project [7, 88]. A combination of the high TMR ratios achieved in this thesis with the idea of crossed anisotropies from the *Camel* project is very promising.

Because of the high sensitivity of TMR sensors, which was demonstrated in this thesis, they are especially suited for the detection of small magnetic fields [89]. Therefore a system to detect small amounts of magnetically marked bio-molecules is a likely application [90]. In the BMBF project *MRBead* an array sensor based on GMR was developed and a prototype successfully tested. Further improvement could be achieved by exchanging the GMR for a TMR sensor [91, 92]; this might be be part of the follow-up project "MRBead plus".

The work on Heusler electrodes, which was started with my diploma thesis [82], was continued with this PhD thesis. In contrast to the diploma thesis where $Co_2Cr_{0.6}Fe_{0.4}Al$ was examined, the promising alloy $Co_2MnSi$ was tested in this PhD thesis. Research groups worldwide deposit Heusler films by dc magnetron sputtering onto single crystalline MgO or sapphire substrates. Here, however, a novel film deposition method for Heusler thin films was used: ion beam deposition. It was demonstrated that this deposition process results in very high quality thin films of variable orientation depending on the substrate and seed layer that is being used. On MgO substrates with MgO/Cr seed (100) oriented, $L2_1$ordered $Co_2MnSi$ films were achieved with room temperature deposition, even without annealing. On the other hand, with NiFeCr/NiFe-seed $Co_2MnSi$ could be grown in (110) orientation after a 350°C annealing. These samples were not in-plane ordered because they were grown on an amorphous substrate (Si + $Al_2O_3$) and only grew B2-ordered. All samples prepared at Sensitec were deposited at room temperature and only annealed *ex situ*. Considering this limitation, especially the results of the CMS films deposited on MgO substrates are remarkable: It is very unusual to achieve well oriented, $L2_1$ ordered films with room temperature deposition; normally high temperature deposition or post deposition annealing are required. This proves the high quality of the films produced at Sensitec.

For applications the use of Si substrates instead of MgO is essential. With the help of an MgO/Cr buffer layer (100) oriented, B2-ordered $Co_2MnSi$ films could be prepared. However, for TMR stacks the film quality has to be further improved. One option is the use of an Ag seed instead of MgO/Cr as proposed by Yang *et al.* [93]. They were able to prepare in-plane ordered (100) oriented CMS thin films on clean Si substrates with 60 nm Ag by sputter deposition at room temperature and subsequent annealing.

Unfortunately it was impossible to combine the Heusler electrode with an MgO tunneling barrier due to unforeseeable chamber conditioning problems. To circumvent this problem different alternatives are possible. Firstly, a TMR stack containing an CMS electrodes and an alumina barrier is thinkable; a cross-talking between alumina and Heusler is excluded as they would be deposited in different sputtering chambers. Another option would be to convert the single target chamber PM 5 into an rf module for the deposition of the MgO barrier. Alternatively a new $Co_2MnSi$ target for dc magnetron sputtering could be installed in PM 4 to separate CMS from barrier deposition: Results with $Co_2Fe_{0.5}Al_{0.5}Si$ from PM 4 and the IBAD MgO barrier achieved in the *MultiMag* project are very promising.

# Bibliography

[1] P. Grünberg et al., Phys. Rev. Lett. **57**, 2442 (1986)

[2] A. Fert et al., Phys. Rev. Lett. **61**, 2472 (1988)

[3] W. H. Butler, X.-G. Zhang, T. C. Schulthess, J. M. MacLaren, Phys. Rev. B **63**, 054416 (2001)

[4] D. D. Djayaprawira et al., Appl. Phys. Lett. **86**, 092502 (2005)

[5] `http://www.sensitec.com`

[6] S. Yuasa, D. D. Djayaprawira, J. Phys. D: Appl. Phys. **40**, R337 - R354 (2007)

[7] `www.camel.0rg.fr`

`http://www.rmnt.org/com/J3N2008/posters/ANR%2005-NANO-041.pdf`

[8] `http://www.isb.rlp.de/index.html?lang=en`

[9] `http://www.physik.uni-bielefeld.de/experi/d2/research/multimag_gr.html`

[10] M. Jullière, Phys. Lett. A, **54**, 225 (1975)

[11] M. B. Stearns, J. Magn. Magn. Mater. **5**, 167 - 171 (1977)

[12] J. C. Slonczewski, Phys. Rev. B **39**, 6995 (1989)

[13] E. Y. Tsymbal et al., J. Phys.: Condens. Matter **15**, R109 - R142 (2003)

[14] J. S. Moodera, G. Mathon, J. Magn. Magn. Mater. **200**, 248 - 273 (1999)

[15] C. Felser et al., Angew. Chem. Int. Ed. **46**, 668 - 699 (2007)

[16] F. Heusler, Über magnetische Manganlegierungen, Archiv der Dt. Phys. Ges. (1901)
F. Heusler, Verh. Dtsch. Phys. Ges. **5**, 219 (1903)

[17] I. Galanakis et al., Appl. Phys. Lett. **89**, 042502 (2006)

[18] T. M. Nakatani et al., J. Magn. Magn. Mater. **322**, 357 - 361 (2010)

[19] T. Ishikawa et al., J. Appl. Phys. **105**, 07B110 (2009)

[20] T. Ishikawa et al., J. Appl. Phys. **103**, 07A919 (2008)

[21] O. Gaier et al., J. Appl. Phys. **103**, 103919 (2008)

[22] P. J. Webster, J. Phys. Chem. Solids **32**, 1221 - 1231 (1971)

[23] R. A. de Groot et al., Phys. Rev. Lett. **50**, 25, 2024 (1983)

[24] I. Galanakis et al., J. Phys. D: Appl. Phys. **39**, 765 - 775 (2006)

[25] S. Ishida et al., Physica B **245**, 1 - 8 (1998)

[26] S. Picozzi et al., Phys. Rev. B **66**, 094421 (2002)

[27] I. Galanakis, P. H. Dederichs, N. Papanikolaou, Phys. Rev. B **66**, 174429 (2002)

[28] B. Balke et al., Phys. Rev. B **74**, 104405 (2006)

[29] S. Picozzi et al., Phys. Rev. B **69**, 094423 (2004)

[30] S. J. Jenkins, D. A. King, Surf. Sci. **501**, L185 - L190 (2002)

[31] I. Galanakis, J. Phys.: Condens. Matter **14**, 6329 - 6340 (2002)

[32] S. Picozzi et al., J. Phys. Chem. Solids **64**, 1697 - 1701 (2003)

[33] S. Javad Hashemifar et al., Phys. Rev. Lett. **94**, 096402 (2005)

[34] A. Sakuma et al., J. Appl. Phys. **105**, 07C910 (2009)

[35] P. A. Dowben, R. Skomski, J. Appl. Phys. **95**, 7453 - 7458 (2004)

[36] H. Itoh et al., Phys. Rev. Lett. **84**, 2501 - 2504 (2000)

[37] Y. Miura et al., J. Phys.: Condens. Matter **21**, 064245 (2009)

[38] J. C. Slater, Phys. Rev. **49**, 931 - 937 (1936)

[39] L. Pauling, Phys. Rev. **54**, 899 - 904 (1938)

[40] G. Fecher et al., J. Appl. Phys. **99**, 08J106 (2006)

[41] K. Özdoğan et al., J. Appl. Phys. **103**, 023503 (2008)

[42] Y. Sakuraba et al., Appl. Phys. Lett. **88**, 192508 (2006)

[43] Y. Sakuraba et al., Jpn. J. Appl. Phys. **44**, L1100 - L1102 (2006)

[44] J. Schmalhorst et al., Appl. Phys. Lett. **86**, 052501 (2005)

[45] J. Mathon, A. Umersky, Phys. Rev. B **63**, 220403(R) (2001)

[46] C. Tiusan et al., J. Phys.: Condens. Matter **19**, 165201 (2007)

[47] D. J. Keavney et al., J. Appl. Phys. **81**, 795 - 798 (1997)

[48] S. S. P. Parkin et al, nature materials **3**, 864 (2004)

[49] K. Ando et al., nature materials **3**, 868 (2004)

[50] S. Ikeda et al., Appl. Phys. Lett. **93**, 082508 (2008)

[51] J. Nogués, I. K. Schuller, J. Magn. Magn. Mater. **192**, 203 - 232 (1999)

[52] G. Feng et al., J. Magn. Magn. Mater. **316**, e984 - e986 (2007)

[53] K. Tsunekawa et al., Digests of the IEEE Int. Magnetics Conf., HP-08 (2005)

[54] Ch. Park et al., IEEE T. Magn. **42**, 2639 - 2641 (2006)

[55] T. Ibusuki et al., Appl. Phys. Lett. **94**, 062509 (2009)

[56] D. J. Kim et al., J. Appl. Phys. **101**, 09B505 (2007)

[57] C. Y. You et al., J. Appl. Phys. **104**, 033517 (2008)

[58] J. Y. Bae et al., J. Appl. Phys. **99**, 08T316 (2006)

[59] J. P. Nozières et al., J. Appl. Phys. **87**, 3920 - 3925 (2000)

[60] S. Yoshimura et al., J. Magn. Magn. Mater. **312**, 176 - 180 (2007)

[61] S. Cardoso, J. Appl. Phys. **103**, 07A905 (2008)

[62] C. P. Wang et al., Appl. Phys. Lett. **71** (20), 2955 (1997)

[63] `http://www.microchemicals.com/photoresist/photoresist_az_eci_3027.htm`

[64] `http://www.microchemicals.com/developer/developers.html`

[65] `http://www.microchem.com/products/pdf/PMGI-Resists-data-sheetV-rhcedit-102206.pdf`

[66] J. Kanak et al., Vacuum **82**, 1057 - 1061 (2008)

[67] Y. M. Lee et al., Appl. Phys. Lett. **89**, 042506 (2006)

[68] J. Hayakawa et al., Appl. Phys. Lett. **89**, 232510 (2006)

[69] J. J. Cha et al., Appl. Phys. Lett. **95**, 032506 (2009)

[70] Y. M. Lee et al., Appl. Phys. Lett. **90**, 212507 (2007)

[71] S. Kämmerer et al., Appl. Phys. Lett. **85**, 79 - 81 (2004)

[72] S. Kämmerer, The Heusler alloy $Co_2MnSi$ in thin films, PhD thesis (2004)

`ttp://bieson.ub.uni-bielefeld.de/volltexte/2005/629/`

[73] S. Tsunegi et al., Appl. Phys. Lett. **93**, 112506 (2008)

[74] P. J. Brown et al., J. Phys.: Condens. Matter **12**, 1827 - 1835 (2000)

[75] M. Oogane et al., J. Phys. D: Appl. Phys. **39**, 834 - 841 (2006)

[76] B. D. Cullity, Elements of X-Ray Diffraction, Addison-Wesley Publishing Company, Inc. (1956)

[77] S. Trudel et al., J. Phys. D: Appl. Phys. **43**, 193001 (2010)

[78] U. Geiersbach et al., J. Magn. Magn. Mater. **240**, 546 - 549 (2002)

[79] H. Kijima et al., J. Magn. Magn. Mater. **310**, 2006 - 2008 (2007)

[80] H. Wulfmeier et al., MA 10.38, poster A, DPG spring meeting 2010, Regensburg

[81] M. Hattori et al., Appl. Phys. Express **1**, 021301 (2008)

[82] A. Gerken, $Co_2Cr_{0.6}Fe_{0.4}Al$-Schichten für magnetische Tunnelkontakte, Diplomarbeit (2006)

[83] K. B. Li et al., J. Magn. Magn. Mater. **303**, e196 - e200 (2006)

[84] J. Lindemuth, J. Krause, B. Dodrill, IEEE T. Magn. **37**, 4, 2752 - 2754 (2001)

[85] S. Kämmerer et al., J. Appl. Phys. **93**, 7945 - 7947 (2003)

[86] S. Tsunegi et al., J. Phys. D: Appl. Phys. **42**, 195004 (2009)

[87] W. F. Brinkman, R. C. Dynes and J. M. Rowell, Phys. Rev. Lett. **41**, 1915 - 1921 (1970)

[88] B. Negulescu et al., Appl. Phys. Lett. **95**, 112502 (2009)

[89] P. P. Freitas et al., J. Phys. Condens. Matter **19**, 165221 (2007)

[90] C. Albon et al., Appl. Phys. Lett. **95**, 023101 (2009)

[91] I. Ennen et al., *Physikalische Aspekte zur Manipulation und Detektion magnetischer Beads in Biosensoren und Lab-on-chip Strukturen*, Tagungsband des 9. Symposiums "Magnetoresistive Sensoren und Magnetische Systeme" in Wetzlar, 52 - 59 (2007)

[92] A. Hütten et al., *From the Nobel Prize in Physics in 2007 Towards Life Science Applications*, Proceedings of the 10th Symposium "Magnetoresistive Sensors and Magnetic Systems" in Wetzlar, 52 - 57 (2009)

[93] J. J. Yang, C. X. Ji, Y. Yang et al., J. Electron. Mater. **37**, 355 - 360 (2008)

# Appendix A

# Mask Drawing

During this PhD thesis the same mask that had been used during my diploma thesis was used. This simple design is only suitable for testing TMR, it is not a proper sensor design. The original design was done by Martin Jourdan from the university of Mainz. During my diploma thesis I modified the design first in AutoCAD and later transferred it to IC Graph by *Mentor Graphics*. There the drawing was finished and the alignment marks and overlay boxes were added.

The reticle contains 16 fields that belong to four different mask layers. The third layer however was abandoned because of a change in the process chain. Of the various designs only one was used throughout this PhD thesis, as the focus was on optimizing the layer stack not the chip layout. The testing and optimization of different layouts is currently done in the follow-up project *MultiMag* [9].

The drawing shows four stacked layers of one final chip. On the top and bottom eight rectangles can be seen (red); these are the contact pads, which are large enough to be contacted manually if needed.

In the middle of the chip a large conductor path reaches from the left to the right end of the chip (red). This is the bottom electrode, made of TMR sensor material.

From the pads to the bottom electrode wedge-shaped conductors (yellow) form the top electrode. Two conductors are connected to one junction, which is the small green dot at the overlap between the bottom and top electrode.

There are two rows of four circular junctions each; their diameters are 50 $\mu$m, 30 $\mu$m, 20 $\mu$m and 16 $\mu$m from left to right. On the reticle different sizes of circular (and square) junctions were added, reaching from 2 $\mu$m to 150 $\mu$m in diameter / edge length.

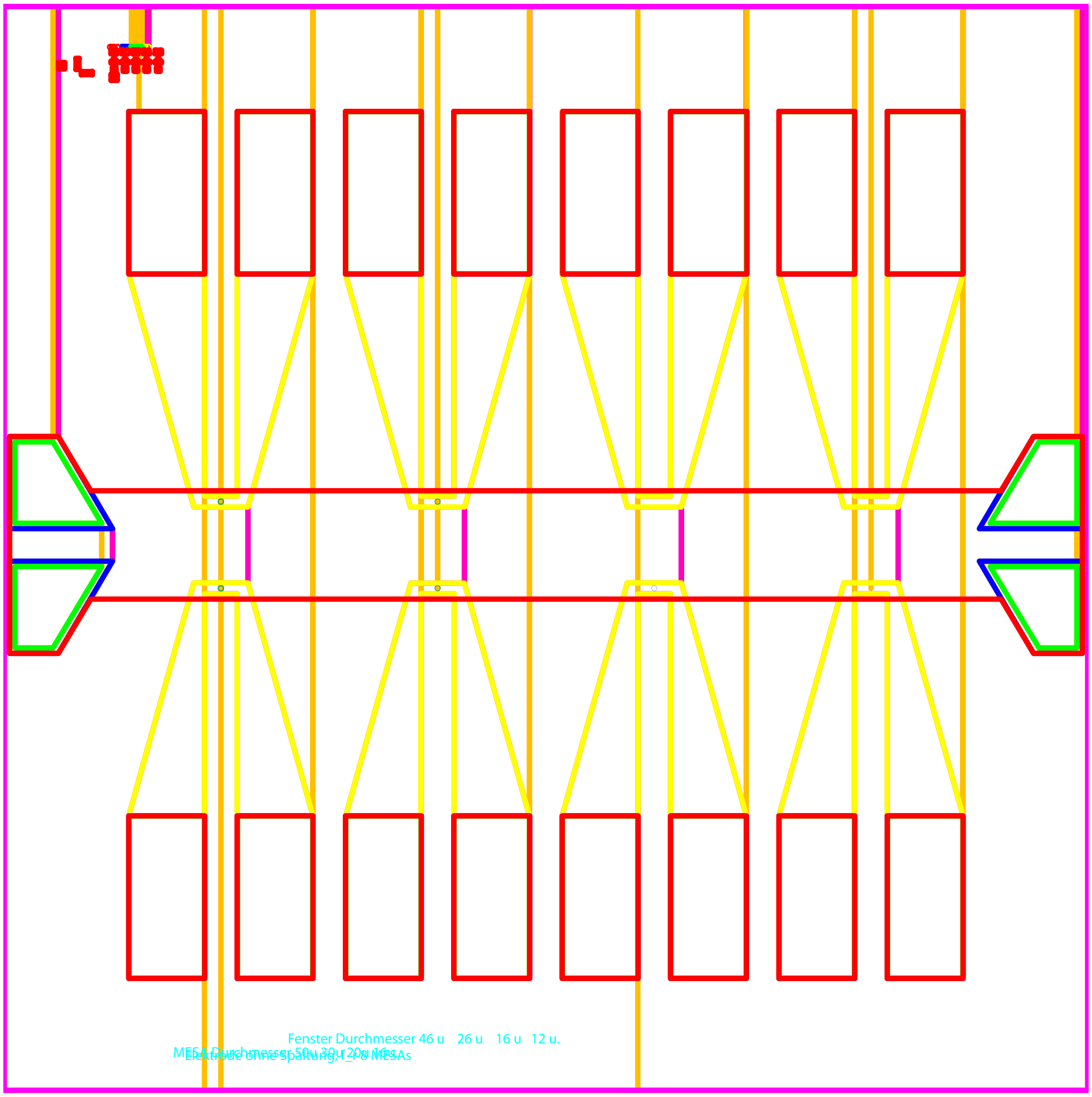

Figure A.1: "Bajor" Chip Layout. All four mask layers are shown in a stacked way here. One can see the pads and contact leads at the top and bottom, the bottom electrode in the middle from left to right and the two rows of junctions in the middle on the bottom electrode.

# Appendix B

# Generic Process Flow

| Layer | Task | Tool | Comment |
|---|---|---|---|
| **Bottom Insulation** | $Al_2O_3$ deposition | Corona | 400 nm |
| **TMR Stack** | Sensor Deposition | PVD 2 | TMR Stack |
| | Annealing | HFRO | 265°C, 5 kOe, 10 min hold |
| **Bottom Electrode** | Photo Apply | FSI 4 | AZ® ECI 3012 |
| | Photo Expose | Canon 2 | 1st |
| | Photo Develop | FSI 4 | AZ® 300 MIF |
| | Photo Inspect | Microscope | |
| | Ion Mill Sensor | Veeco 5 | Mill into $Al_2O_3$ |
| | Measure Overmill | Nanometrics | $Al_2O_3$ thckn. |
| | Remove resist | Matrix Asher | $O_2$-Plasma, 4 min |
| | Strip | Barrel Stripper | NMP |
| | Fence Remove | Snow Cleaner | $CO_2$ cleaning |
| | Inspect | Microscope | resist residues? |
| **MTJ** | Photo Apply | FSI 4 | LOR 1A + AZ® ECI 3012 |
| | Photo Expose MTJ | Canon 2 | TVPA, MTJ |
| | Photo Develop | FSI 4 | AZ® 300 MIF |
| | Photo Inspect | Microscope | Undercut ok? |
| | Ion Mill Sensor | Veeco 5 | stop after barrier |
| | Measure Overmill | Nanometrics | $Al_2O_3$ thckn. |
| **Gap Refill** | Gap2 Deposition | Corona | 60 nm $Al_2O_3$ |
| | Measure Gap | Nanometrics | $Al_2O_3$ thckn. |
| | Gap Liftoff | Equinox | Liftoff with NMP |

| **Layer** | **Task** | **Tool** | **Comment** |
|---|---|---|---|
| | Fence Remove | Snow Cleaner | $CO_2$ cleaning |
| | Mesa Inspect | Microscope | resist residues? |
| **Contact Pads** | Photo Apply | FSI 4 | LOR 5A + AZ® ECI 3012 |
| | Photo Expose | Canon 2 | TVPA, Contacts |
| | Photo Develop | FSI 4 | AZ® MIF 300 |
| | Photo Inspect | Microscope | Undercut ok? |
| | Ta/Au Depo | Z660 | 40 nm Ta + 200 nm Au |
| | Liftoff | Equinox | Liftoff with NMP |
| | *Fence Remove* | *Snow Cleaner* | *$CO_2$ cleaning* |
| | Final Inspection | Microscope | Final Inspection |
| **Test** | Test IU | Final 02 | Test IU, no field |
| | Test TMR | Final 02 | Test TMR 5inch |

Table B.1: Generic process flow for standard TMR structures.

# Appendix C

# EDX-Analysis of the $Co_2MnSi$ Target

The $Co_2MnSi$ target had been ordered off-stoichiometric to compensate for different sputtering yields of the components. A composition of 43.6 % Co, 28.0 % Mn and 28.4 % Si was chosen and a reference sample was analyzed by EDX. As only samples of limited height can be analyzed with the EDX at Sensitec the sample was diced before, resulting in contamination. Therefore all elements except for Co, Mn and Si were excluded from the report.

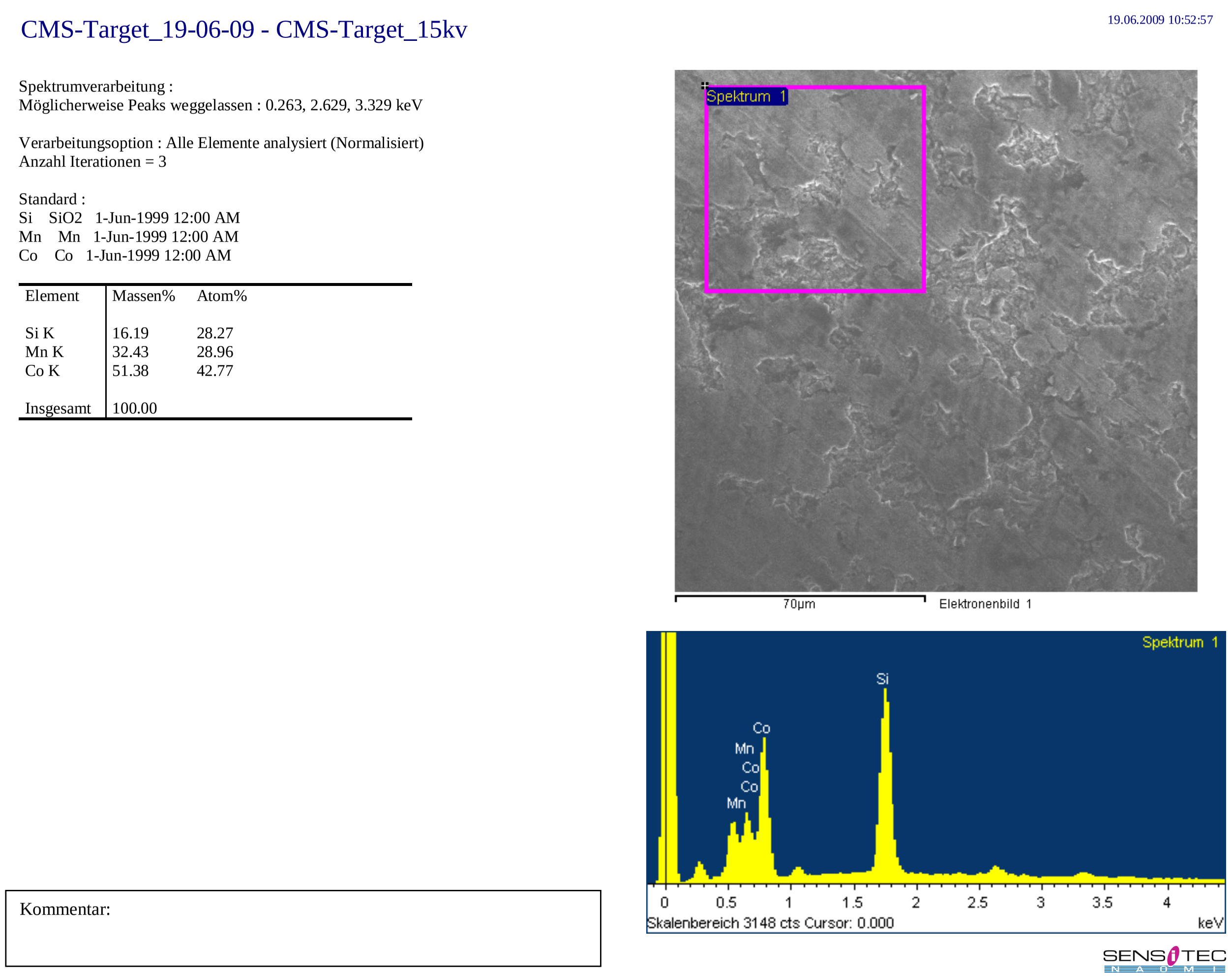

CMS-Target_19-06-09 - CMS-Target_15kv

19.06.2009 10:52:57

Spektrumverarbeitung :
Möglicherweise Peaks weggelassen : 0.263, 2.629, 3.329 keV

Verarbeitungsoption : Alle Elemente analysiert (Normalisiert)
Anzahl Iterationen = 3

Standard :
Si SiO2 1-Jun-1999 12:00 AM
Mn Mn 1-Jun-1999 12:00 AM
Co Co 1-Jun-1999 12:00 AM

| Element | Massen% | Atom% |
|---|---|---|
| Si K | 16.19 | 28.27 |
| Mn K | 32.43 | 28.96 |
| Co K | 51.38 | 42.77 |
| Insgesamt | 100.00 | |

Kommentar:

Figure C.1: EDX analysis of the Co$_2$MnSi target. All elements apart from Co, Mn and Si were excluded from the results as they were due to the sample preparation (dicing).

# Appendix D

# List of X-Ray Diffraction Peak Positions

| **hkl** | **2$\theta$** [°] | **d**$_{hkl}$ [Å] | **I**$_{rel}$ [%] |
|---|---|---|---|
| 111 | 27.269 | 3.268 | 4.74 |
| 200 | 31.589 | 2.830 | 5.05 |
| 220 | 45.279 | 2.001 | 100 |
| 311 | 53.664 | 1.707 | 1.91 |
| 222 | 56.257 | 1.634 | 1.22 |
| 400 | 65.965 | 1.415 | 14.8 |
| 331 | 72.772 | 1.299 | 0.61 |
| 420 | 74.982 | 1.266 | 1.34 |
| 422 | 83.630 | 1.155 | 28.92 |
| 511 | 90.010 | 1.089 | 0.31 |
| 333 | 90.010 | 1.089 | 0.10 |
| 440 | 100.685 | 1.006 | 10.21 |

Table D.1: X-Ray Diffraction peak positions for $Co_2MnSi$ for Cu $K_\alpha$ radiation.

| **hkl** | **2$\theta$ [°]** | **d$_{hkl}$ [Å]** | **I$_{rel}$ [%]** |
|---|---|---|---|
| 111 | 37.016 | 2.427 | 10.39 |
| 200 | 43.006 | 2.102 | 100 |
| 220 | 62.447 | 1.486 | 55.52 |
| 311 | 74.868 | 1.267 | 6.95 |
| 222 | 78.822 | 1.213 | 16.54 |
| 400 | 94.293 | 1.051 | 7.71 |
| 331 | 106.045 | 0.964 | 3.49 |

Table D.2: X-Ray Diffraction peak positions for MgO for Cu K$_\alpha$ radiation.

| **hkl** | **2$\theta$ [°]** | **d$_{hkl}$ [Å]** | **I$_{rel}$ [%]** |
|---|---|---|---|
| 110 | 30.931 | 2.889 | 100 |
| 200 | 44.309 | 2.043 | 17.22 |
| 211 | 55.014 | 1.668 | 33.70 |
| 220 | 64.459 | 1.444 | 9.78 |
| 310 | 73.205 | 1.292 | 12.79 |
| 222 | 81.562 | 1.179 | 3.08 |
| 321 | 89.741 | 1.092 | 14.59 |
| 400 | 97.914 | 1.021 | 1.57 |
| 411 | 106.254 | 0.963 | 5.85 |
| 330 | 106.254 | 0.963 | 2.93 |

Table D.3: X-Ray Diffraction peak positions for Cr for Cu K$_\alpha$ radiation.

| **hkl** | **2$\theta$ [°]** | **d$_{hkl}$ [Å]** | **I$_{rel}$ [%]** |
|---|---|---|---|
| 111 | 28.444 | 3.135 | 100 |
| 220 | 47.306 | 1.920 | 67.11 |
| 311 | 56.126 | 1.637 | 39.94 |
| 222 | 58.860 | 1.568 | 0 |
| 400 | 69.135 | 1.358 | 10.70 |
| 331 | 76.382 | 1.246 | 16.19 |
| 422 | 88.037 | 1.109 | 23.14 |
| 511 | 94.960 | 1.045 | 10.17 |
| 333 | 94.960 | 1.045 | 3.39 |
| 440 | 106.718 | 0.960 | 9.18 |

Table D.4: X-Ray Diffraction peak positions for Si for Cu K$_\alpha$ radiation.

| **hkl** | **2$\theta$ [°]** | **d$_{hkl}$ [Å]** | **I$_{rel}$ [%]** |
|---|---|---|---|
| 100 | 38.381 | 2.344 | 67.88 |
| 002 | 42.179 | 2.141 | 18.34 |
| 101 | 44.015 | 2.056 | 100 |
| 102 | 58.335 | 1.581 | 52.77 |
| 110 | 69.409 | 1.353 | 18.09 |
| 103 | 78.390 | 1.219 | 28.85 |
| 200 | 82.208 | 1.172 | 13.42 |
| 112 | 84.679 | 1.144 | 25.81 |
| 201 | 85.938 | 1.130 | 25.37 |

Table D.5: X-Ray Diffraction peak positions for Ru for Cu K$_\alpha$ radiation.

# Appendix E

# Publications & Talks

## E.1 Publications

J. Paul und Anna Gerken, *Tunnelmagnetoresistive Materialien: Möglichkeiten und Herausforderungen für Anwendungen in der Sensorik*, Tagungsband des 9. Symposiums "Magnetoresistive Sensoren und Magnetische Systeme" in Wetzlar, S. 11-17 (2007)

J. Paul, A. Gerken, *Tunnelmagnetoresistive Materialien für Anwendungen in der Sensorik*, Proceedings of Mikrosystemtechnik Kongress 2007, 287 - 290 (2007)

A. Gerken and J. Paul, *Use of the Tunnelmagnetoresistive Effect for Sensor Applications*, Microsystems Technology in Germany 2008, trias Consult, 50 - 51, (2008)

A. Gerken, J. Paul, B. Negulescu, C. Duret, *TMR-Schichtsysteme für Sensoranwendungen*, Proceedings of Mikrosystemtechnik Kongress 2009, (2009)

B. Negulescu, D. Lancour, F. Montaigne, A. Gerken, J. Paul, V. Spetter, J. Marien, C. Duret and M. Hehn, *Wide range and tunable magnetic tunnel junction sensor using two exchange pinned electrodes*, Appl. Phys. Lett. **95**, 112502 (2009)

J. Paul, A. Gerken, J. Marien, B. Negulescu, M. Hehn, C. Duret, *Neue TMR-Schichtsysteme für Sensoranwendungen*, Tagungsband:Technologien und Werkstoffe der Mikrosystem- und Nanotechnik (GMM-FB 65), (2010)

A. Gerken, J. Paul, B. Negulescu, C. Duret, *TMR Stacks for Sensor Applications*, Microsystems Technology in Germany 2010, trias Consult, 50 - 51, (2010)

## E.2 Talks

J. Paul, A. Gerken, *Tunnelmagnetoresistive Materialien: Möglichkeiten und Herausforderungen für Anwendungen in der Sensorik*, 9th Symposium "Magnetoresistive Sensoren und Magnetische Systeme", 13.03.2007, Wetzlar

J. Paul, A. Gerken, *Tunnelmagnetoresistive Materialien für Anwendungen in der Sensorik*, invited talk, MikroSystemTechnik Kongress 2007, 15. - 17.10.2007, Dresden

C. Schug, A. Gerken and J. Paul, *XRD-Untersuchungen an dünnen* $Co_2Cr_{0.6}Fe_{0.4}Al$ *(CCFA)-Schichten für TMR-Elemente*, 13th PANalytical-Symposium, 12. - 15.06.2008, Kassel

J. Paul, J. Marien, A. Gerken, B. Negulescu, M. Hehn, *Development of magnetic tunnel barriers in a manufacturing line for sensor production*, Biomagsens workshop "Magnetic tunnel junctions for highly sensitve sensors", Les Vaulx de Cernay, France, 21. - 23.10.2008

A. Gerken, J. Paul, *TMR-Schichtsysteme für Sensoranwendungen*, MikroSystemTechnik Kongress 2009, 12th - 14th October 2009, Berlin

J. Paul, A. Gerken, J. Marien, B. Negulescu, M. Hehn, C. Duret, *Neue TMR-Schichtsysteme für Sensoranwendungen*, 2nd GMM Workshop Technologien & Werkstoffe der Mikrosystem- und Nanotechnik, 10th - 11th May 2010, Darmstadt

# Danksagung

An dieser Stelle möchte ich mich bei allen Personen bedanken, die zum Gelingen dieser Arbeit beigetragen haben.

Mein Dank gilt vor allem Prof. Dr. Andreas Hütten für die Betreuung dieser externen Doktorarbeit und die finanzielle Unterstützung zu Beginn dieser Promotion. Durch seinen stetigen Optimismus hat Andreas mich immer wieder aufgebaut, wenn ich selbst kaum noch an den Erfolg dieser Arbeit geglaubt habe. Außerdem möchte ich mich bei der gesamten D2-Gruppe für die Unterstützung bei meinen ,,Besuchen” in Bielefeld und die tolle Atmosphäre bedanken; schade, daß ich nicht länger mit Euch gearbeitet habe. Besonderer Dank gilt Anna Regtmeier und Simone Herth, in deren Büros ich während meiner Zeit in Bielefeld untergekommen bin und Daniel Ebke für die durchgeführten TMR-Messungen und die Diskussionen zum Thema CMS. Außerdem möchte ich mich bei allen bedanken, die mich in die verschiedenen Geräte wie TMR-Tester, Lithographie-Ausrüstung und Ätzer eingewiesen haben.

Bei Sensitec danke ich insbesondere den Sputterern Viktor Spetter und Jürgen Wahrhusen; ohne ihre guten Ideen und vielen kleinen Tipps zu den Eigenheiten der PVD 2 bei der Prozessentwicklung für MgO wären diese guten Ergebnisse nicht möglich gewesen.
Der Aufbau des TMR-Testers lag vor allem in den Händen von Stefan Eilers; ihm und Johannes Paul danke ich für die vielen Stunden, Tage und Wochen der Programmierarbeit und Fehlersuche. Die Möglichkeit bei Sensitec intern zu testen war ein wichtiger Meilenstein im TMR-Projekt und hat die Arbeiten zur Barrierenoptimierung wesentlich beschleunigt.
Christoph Schug danke ich für die Unterstützung bei den Röntgenuntersuchungen und die Auswertungen der XRR-Messungen; mit seinem Enthusiasmus und seiner Erfahrung hat er mir stets hilfreich zur Seite gestanden.

Kurt Krämer und Andreas Meye habe ich für die Durchführung diverser EDX-Analysen zu danken.
Marco Doms, Bruno Hermann und Volker Seidemann danke ich für die Gewährung der nötigen Freiheiten bei Sensitec, so daß ich meine Doktorarbeit und die Ingenieurstätigkeit gut in Einklang bringen konnte. Marco danke ich außerdem für das kritische Lesen der ersten Version dieser Doktorarbeit und die vielen hilfreichen Verbesserungsvorschläge.
Dem Photo-Team danke ich dafür, daß es mich all die Jahre ertragen hat; Jungs (und Mädel), es hat immer Spaß gemacht mit Euch.
Allen Fachgruppen danke ich, daß sie mir bei diversen Fragen zur Prozesstechnik immer weitergeholfen haben und außerdem dafür gesorgt haben, daß meine Wafer immer zügig prozessiert wurden.
Mein Dank gilt außerdem den ,,MultiMags", die bei Sensitec das TMR- und Heusler-Fähnchen hoch halten. Besonders danke ich Tanja Graf für die wertvollen Diskussionen zu Heusler-Schichten und Ronald Lehndorff für die Gespräche zu MgO, die mich immer wieder auf neue Ideen brachten.
Ich danke Johannes Paul für die Leitung des TMR-Projekts bei Sensitec in dessen Rahmen diese Dissertation angefertigt wurde.

Mein besonderer Dank gilt dem Land Rheinland-Pfalz, daß im Rahmen der ,,Förderung von Forschungs- und Entwicklungsvorhaben in der mittelständischen Wirtschaft des Landes Rheinland-Pfalz" unter dem Aktenzeichen 3304.1429.17063 das Vorhaben ,,Tunnelmagnetoresistive Elemente für neue Applikationen in der Sensorik" finanziell gefördert hat und dadurch meine Dissertation bei der Sensitec GmbH erst ermöglicht hat.

Last but not least: Vielen Dank an Sloyde, $\varphi$B und Nikita für die moralische Unterstützung in den vergangenen Jahren.